Focused Ultrasound Thermal Therapy Monitoring using Ultrasound, Infrared Thermal, and Photoacoustic Imaging Techniques

By

Yi-Sing Hsiao

A dissertation submitted in partial fulfillment
of the requirements for the degree of
Doctor of Philosophy
(Biomedical Engineering)
in the University of Michigan
2013

Doctoral Committee:

Associate Professor Cheri X. Deng, Co-Chair
Professor Albert Shih, Co-Chair
Professor J. Brian Fowlkes
Associate Professor Xueding Wang
Assistant Professor Zhen Xu

To my parents, Ching-Kai and Shih-Ya, for their unconditional love and support, and to my grandfather, who gives me all his blessings.

Acknowledgements

I would like to first sincerely thank my advisor, Prof. Cheri Deng, for her patience and support in guiding me to completion of my PhD study. Our intellectual conversations have been full of interesting and unexplored ideas which motivate me to broaden my knowledge and logical thinking. I would like to thank all my committee members, whose guidance and feedback help make this dissertation possible. My co-advisor, Prof. Albert Shih, has been very supportive and always concerned with my progress. Prof. Xueding Wang has shared many valuable insights with me and helped me greatly in transforming thoughts into experiments. I would also like to thank Prof. Zhen Xu and Prof. J. Brian Fowlkes for their research suggestions and insightful thoughts. I have always enjoyed the conversations with these faculties and truly appreciated their help.

I am also very grateful to have lab members who are always beside me and have made my PhD life enriching. I would like to especially express my gratitude to Dr. Ronald Kumon, who has been a great mentor and friend. I would like to also thank my labmates Madhu, Ziqi, Di, Yu, Zhenzhen, Yun, and Juyoung for their company and help through the years. I am fortunate to have connections with them outside the laboratory and I truly appreciate the friendship we have. Many thanks go to people in Dr. Cain's, Dr. Xu's, and Dr. Wang's lab for their friendship and research support. I have always appreciated the encouraging and insightful discussions with them. I would like to thank Kuang-Wei in particular, for his help beginning the first day I came to Ann Arbor.

In addition to the people I encountered in the research field, I would like to thank all the staff members in Biomedical Engineering, especially Maria Steele and Kathy McCrumb. I would also like to express my deepest gratitude to my friends outside the lab, including those in Michigan and old friends back in Taiwan. They have showed me true friendship and constant support which enabled me to overcome many obstacles in life. Thank you all for sharing your love with me. I would like to thank my boyfriend, Nai-Chung, for his always love and support. We have shared so many joyful years together and he has always given me the courage and strength to overcome challenges in life.

Finally, my greatest thanks go to my parents and my brother, Gary. Thank you all for your unconditional love. Your words of comfort and support are always in my heart. I love you all so much.

Yi-Sing Tina Hsiao

June 28, 2013

Table of Contents

List of Figures

FIGURE

Chapter 2

Chapter 3

Chapter 4

Chapter 5

List of Tables

TABLE

Chapter 2

Chapter 5

Abstract

Focused ultrasound (FUS) is a promising thermal treatment modality which deposits heat noninvasively in a confined tissue volume to treat localized diseased tissue or malignancy through hyperthermia or high temperature ablation. FUS compatible guiding and monitoring systems to provide real-time information on tissue temperature and/or status (e.g., native or necrotized) are important to ensure safe and effective treatment outcome; however, current development of such systems are restricted to ultrasound and magnetic resonance imaging (MRI). The work described in this dissertation represents efforts not only to explore new tools to evaluate current monitoring techniques but also to develop new FUS monitoring modalities. In the first study, a new evaluation platform for ultrasound thermometry using infrared (IR) thermography was developed and demonstrated using phantoms subjected to FUS heating, providing a fast calibration and validation tool with spatiotemporal temperature information unavailable with traditional thermocouple measurements. In the second study, IR thermography was investigated as a new tool for high temperature FUS ablation monitoring. The spatiotemporal temperature characteristics in correspondence to lesion formation and bubble activities were identified using simultaneous IR and bright-field imaging. Tissue-specific thermal damage threshold, which is critical for accurate estimation of tissue status based on temperature time history, was also obtained using the same system. In the final study, we developed a novel dual-wavelength photoacoustic (PA) sensing technique for monitoring tissue status during thermal treatments, which is capable of separating the two effects from temperature rise and changes in optical

properties due to tissue alteration. Experimental validations of the theoretical derivation were carried out on *ex-vivo* cardiac tissue using water-bath heating on lesions generated by FUS. Future directions of research include *in-vivo* technique demonstration where effects such as blood perfusion on FUS heating need to be considered. When FUS operates in the non-ablative regime without causing irreversible changes in tissue, treatment monitoring techniques investigated in this study also have the potential to be translated into diagnostic tools.

CHAPTER 1

Introduction

1.1 Thermal therapy

Treatment modalities for treating localized diseased tissue or malignancy have evolved from invasive surgeries to minimally invasive and further to noninvasive techniques over the past few decades.[1,2] Open surgery imposes great risk on patients with its high morbidity and mortality rate and the recovery time is often lengthy. Less invasive laparoscopic surgery has become more adopted with lower complications and less pain and scarring compared to open surgery,[3,4] but with concerns including port site metastases due to surgical operation.[5] Many of the other minimally invasive techniques are based on thermal therapy, which has been proven to be effective in treating benign and malignant diseases.

Thermal therapy can be classified into two categories. Hyperthermia, in which tissue temperature is elevated from normal body temperature, 37 °C, to 41 – 45 °C, is often used for cancer treatment in conjunction with radiation therapy and chemotherapy.[6-9] The elevated temperature also allows for controlled drug release using thermosensitive agents loaded with drugs.[10] Another type of thermal therapy is high temperature ablation which can destruct diseased tissue through the induction of coagulative necrosis.[11] Common heat sources to induce hyperthermia and thermal ablation include radiofrequency, microwave, laser, and focused ultrasound (FUS). Among all types of heat source, FUS is the truly noninvasive

treatment modality which is capable of inducing localized heating in deep tissue from thermoviscous absorption of ultrasound energy.[1,12-13]

1.1.1 Hyperthermia

Whole-body hyperthermia, which heats up not only the target tissue but also the normal tissue, is often associated with systemic or local side-effects.[14] Therefore, recent developments in hyperthermia have been focused on localized or targeted hyperthermia where heating is restricted to a confined tissue volume (e.g., tumor site).

There are various aspects of hyperthermia in its interaction with tissue/cell to achieve therapeutic effects. For example, elevated temperature increases blood flow, resulting in a higher concentration of drugs in the region subjected to hyperthermia, and therefore yields a higher drug uptake at the target site.[14] It was also found that some gene regulations can be modulated by heat (e.g., heat-shock proteins).[15] Hyperthermia can also be applied to trigger the release of chemotherapeutic drugs loaded in thermosensitive liposomes, which further reduces the drug exposure to normal tissue.[16-18] Other bio-compatible materials on the micron or nanometer scale have also been developed to work with hyperthermia to improve treatment efficacy. These materials can be injected into the patient's circulatory system just like the liposomes to enhance the heating efficiency with site specificity. For example, metal nanoparticles capable of converting electromagnetic energy into heat have been developed with cancer-specific molecules to bind to cancer cells.[15,19]

FUS hyperthermia has been used in adjunct to radiotherapy and showed improved treatment outcome compared to using the radiotherapy alone.[20-22] An active research field using FUS hyperthermia is in enhanced targeted drug delivery to tumors using

thermosensitive liposomes.[10,16,23] Various strategies for optimizing FUS exposures for hyperthermia applications have also been investigated.[24,25]

1.1.2 High temperature ablation

Delivery of lethal energies to the diseased tissue can lead to irreversible damage. Except for cryoablation which induces cell death by freezing, other minimally invasive ablative modalities operate in the higher temperature range (> 50 °C) above the threshold for tissue necrosis/coagulation. Radiofrequency (RF) ablation is widely used, in which high-frequency AC current is delivered to the target site through a needle electric probe or catheter where the electrical energy is converted into heat.[1,26] Because the tip of the probe needs to be in contact with the tissue, RF ablation is delivered through open or laparoscopic surgery or percutaneously. Another type of ablation uses laser (photothermal) in which laser fiber is guided by needles to the target site to deliver light. It is often used with nanomaterials which have strong optical absorption in the near-infrared region.[27,28]

FUS, unlike these other methods, is the only truly noninvasive modality for heat deposition. The use of FUS at higher intensities to raise tissue temperatures sufficiently high to generate thermal damage is usually termed high-intensity focused ultrasound ablation, or simply as HIFU ablation. Its clinical application include cancer treatments (e.g., prostate,[29,30] liver,[31,32] kidney,[32-34] bone,[35] and brain[36]), uterine fibroid treatments,[37,38] and neurosurgeries.[39] For HIFU treatments of biological tissues, it is important to have monitoring techniques to measure tissue change (e.g., from native to coagulated) for providing real-time feedback to ensure safe and effective outcome.

1.2 Current FUS monitoring techniques

1.2.1 Tissue temperature and tissue status

For successful FUS thermal therapy, the heating process has to be closely monitored. Two aspects can be monitored: tissue temperature and tissue status. Temperature measurement is critical for both hyperthermia and HIFU ablation. In FUS-induced hyperthermia, the spatiotemporal temperature evolution needs to be monitored to ensure sufficient temperature increase to trigger desired events (e.g., drug release), while maintaining the temperature below a certain threshold so as not to cause irreversible damage to the cells.[40] In HIFU ablation, the temperature time history can be used to calculate the thermal dose, which is then used to predict tissue necrosis/coagulation. The temperature distribution has to be carefully controlled so that thermal damage to the tissue only occurs in the target treatment volume and not the surrounding normal tissue.

Tissue status is the other parameter to monitor and applies specifically for HIFU ablation where the tissue changes from its native state to necrotized or coagulated state during treatment. These changes are reflected in changes in tissue properties such as optical, acoustic, mechanical, and thermal properties. For both temperature measurement and tissue characterization, the two most widely investigated noninvasive imaging modalities for real-time FUS monitoring are magnetic resonance imaging (MRI) and ultrasound imaging.

1.2.2 Magnetic resonance imaging in FUS monitoring

MRI is capable of estimating temperature increases with sensitivity within a few degrees[41,42] based on temperature-sensitive MR parameters such as T_1 and T_2 relaxation time, proton resonance frequency (PRF), and proton diffusion coefficient (D).[41,43] MRI-guided focused ultrasound (MRIgFUS) has been used clinically to treat uterine fibroid and breast

tumors and noninvasively estimate tissue temperature[44-46] and are currently the only FDA-approved clinical HIFU systems. For tissue characterization, post-treatment MRI also provides good contrast in delineating tissue types and HIFU lesions with millimeter spatial resolution.[44,47]

However, there are several disadvantages of MRI. For MRIgFUS ablation in liver and kidney,[48-50] its unreliable temperature measurement in fat and susceptibility to artifacts induced by organ displacements still remains a challenge.[43] Furthermore, the acquisition duration required by MRI (few seconds/frame)[51] may limit its use in treatments using short FUS pulses with rapid tissue heating[41] or result in extended treatment time.[52] The average treatment time using MRIgFUS is between $1 - 4$ hours with the total hours in the scanner being longer.[45,53] The treatment devices are also required to be made MR-compatible. Moreover, the high cost of MRI scanners, the claustrophobia and discomfort for some patients in closed-bore systems, and the lack of portability of MRI systems may further restrict the widespread use of the technology for FUS therapy.[1]

1.2.3 Ultrasound imaging in FUS monitoring

In contrast, ultrasound is non-ionizing and the imaging systems have high portability and are at a lower cost. Ultrasound systems are also inherently compatible to various types of thermal treatment devices. Dual-mode transducers for both imaging and thermal therapy have also been designed with the main advantage being implicit registration of the targeted region.[54] Conventional diagnostic ultrasound imaging with gray-scale representation (B-mode imaging) is frequently applied to monitoring HIFU ablation. However, in the absence of the occurrence of bubbles at high ultrasound pressure level and/or boiling temperature, the low acoustic contrast between coagulated and native tissue itself is not

always sufficient. This urges researchers to derive various parameters to improve the visualization and detection of lesion formation,[55] including ultrasound attenuation and backscatter,[56,57] spectral parameters,[58,59] thermal strain[60,61] or stiffness (e.g., using acoustic radiation force imaging (ARFI)[62,63]). For temperature estimation, temperature-dependent changes in the ultrasound backscattered signals are used. A variety of techniques have been explored, including methods based on echo time shifts,[64-70] changes in backscatter energy,[71-73] and spectral parameters.[74] For accurate temperature estimation, all methods require calibrations in advance as the temperature dependency of these parameters are tissue type specific. These methods also need to account for artifacts from organ/tissue movement. Furthermore, as a result of problems associated with the rapid and large range of temperature variations in HIFU ablation and disruption by cavity formation,[75,76] ultrasound thermometry has been mostly used in the hyperthermia temperature range.

1.3 Organization of this dissertation

Motivated by the limited imaging techniques developed for FUS monitoring, in this dissertation, we aim to explore new tools to better evaluate current monitoring techniques and also develop new imaging methods.

Ultrasound imaging, although has shown good capability to estimate temperature in the hyperthermia regime, requires calibration for different tissue types undergoing FUS heating. To calibrate tissue-specific properties and also to verify the design of signal processing algorithm, independent temperature measurement is always required. Evaluation of ultrasound thermometry is usually done using thermocouples inserted at discrete locations. In Chapter 2, infrared (IR) thermography is introduced as a new tool to evaluate ultrasound

thermometry with high spatial and high temporal temperature measurements unavailable with other tools.

As we investigate into the higher temperature range reached in HIFU ablation, the limited temperature estimation range of ultrasound imaging and the high cost of MRI systems urge us to search for alternative imaging tools. At the same time, there is also a need to establish a better understanding of the correlation between temperature and HIFU-induced events (e.g., tissue necrosis/coagulation and bubble activities). In Chapter 3, IR thermography was further used to measure the spatiotemporal temperature on a tissue surface during HIFU ablation, and the occurrences of lesion and bubble formation were identified to have strong correlations with several temperature-derived parameters. A method to experimentally measure the thermal damage threshold for any tissue type is also presented.

To further explore new imaging methods for FUS monitoring, Chapter 4 describes a dual-wavelength photoacoustic (PA) sensing/imaging technique capable of monitoring tissue status independent of temperature changes. Compared to IR thermography, PA imaging allows a deeper imaging penetration depth. Typical PA imaging methods investigated for thermal treatment monitoring exhibit difficulties in identifying tissue coagulation because PA signal intensity is both temperature and tissue status dependent. Our technique, however, derives a parameter representative of the tissue status only, which enables more robust monitoring of thermal ablation. The technique was verified with *ex-vivo* tissue experiments.

Finally, Chapter 5 concludes this work and presents future directions, including applying the techniques to tissue volume more deeply beneath the tissue subsurface and to *in-vivo* conditions. New applications inspired by the current study will also be discussed.

1.4 References

1. J. E. Kennedy, "High-intensity focused ultrasound in the treatment of solid tumours," *Nat Rev Cancer* 5(4), 321-327 (2005)

2. T. A. Leslie and J. E. Kennedy, "High-intensity focused ultrasound principles, current uses, and potential for the future," *Ultrasound Quarterly* 22(4), 263-272 (2006)

3. K. T. Nguyen, T. C. Gamblin and D. A. Geller, "World review of laparoscopic liver resection-2,804 patients," *Ann Surg* 250(5), 831-841 (2009)

4. T. Makino, J. W. Milsom and S. W. Lee, "Feasibility and safety of single-incision laparoscopic colectomy: a systematic review," *Ann Surg* 255(4), 667-676 (2012)

5. H. Tomita, P. W. Marcello and J. W. Milsom, "Laparoscopic surgery of the colon and rectum," *World J Surg* 23(4), 397-405 (1999)

6. K. S. Ryu, J. H. Kim, H. S. Ko, J. W. Kim, W. S. Ahn, Y. G. Park, S. J. Kim and J. M. Lee, "Effects of intraperitoneal hyperthermic chemotherapy in ovarian cancer," *Gynecol Oncol* 94(2), 325-332 (2004)

7. M. Franckena, L. C. Lutgens, P. C. Koper, C. E. Kleynen, E. M. van der Steen-Banasik, J. J. Jobsen, J. W. Leer, C. L. Creutzberg, M. F. Dielwart, Y. van Norden, R. A. Canters, G. C. van Rhoon and J. van der Zee, "Radiotherapy and hyperthermia for treatment of primary locally advanced cervix cancer: results in 378 patients," *Int J Radiat Oncol Biol Phys* 73(1), 242-250 (2009)

8. M. W. Dewhirst, L. Prosnitz, D. Thrall, D. Prescott, S. Clegg, C. Charles, J. MacFall, G. Rosner, T. Samulski, E. Gillette and S. LaRue, "Hyperthermic treatment of malignant diseases: current status and a view toward the future," *Semin Oncol* 24(6), 616-625 (1997)

9. T. M. Zagar, J. R. Oleson, Z. Vujaskovic, M. W. Dewhirst, O. I. Craciunescu, K. L. Blackwell, L. R. Prosnitz and E. L. Jones, "Hyperthermia combined with radiation therapy for superficial breast cancer and chest wall recurrence: a review of the randomised data," *Int J Hyperthermia* 26(7), 612-617 (2010)

10. R. Staruch, R. Chopra and K. Hynynen, "Localised drug release using MRI-controlled focused ultrasound hyperthermia," *Int J Hyperthermia* 27(2), 156-171 (2011)

11. S. N. Goldberg, G. S. Gazelle and P. R. Mueller, "Thermal ablation therapy for focal malignancy: a unified approach to underlying principles, techniques, and diagnostic imaging guidance," *Am J Roentgenol* 174(2), 323-331 (2000)

12. S. Crouzet, F. J. Murat, G. Pasticier, P. Cassier, J. Y. Chapelon and A. Gelet, "High intensity focused ultrasound (HIFU) for prostate cancer: Current clinical status, outcomes and future perspectives," *Int J Hyperthermia* 26(8), 796-803 (2010)

13. G. ter Haar, "Harnessing the interaction of ultrasound with tissue for therapeutic benefit: High-intensity focused ultrasound," *Ultrasound Obst Gyn* 32(5), 601-604 (2008)

14. P. Wust, B. Hildebrandt, G. Sreenivasa, B. Rau, J. Gellermann, H. Riess, R. Felix and P. M. Schlag, "Hyperthermia in combined treatment of cancer," *Lancet Oncol* 3(8), 487-497 (2002)

15. P. Cherukuri, E. S. Glazer and S. A. Curleya, "Targeted hyperthermia using metal nanoparticles," *Adv Drug Deliver Rev* 62(3), 339-345 (2010)

16. H. Grüll and S. Langereis, "Hyperthermia-triggered drug delivery from temperature-sensitive liposomes using MRI-guided high intensity focused ultrasound," *J Control Release* 161(2), 317-327 (2012)

17. R. Staruch, R. Chopra and K. Hynynen, "Hyperthermia in bone generated with MR imaging-controlled focused ultrasound: control strategies and drug delivery," *Radiology* 263(1), 117-127 (2012)

18. G. A. Koning, A. M. M. Eggermont, L. H. Lindner and T. L. M. ten Hagen, "Hyperthermia and thermosensitive liposomes for improved delivery of chemotherapeutic drugs to solid tumors," *Pharm Res* 27(8), 1750-1754 (2010)

19. C. S. S. R. Kumar and F. Mohammad, "Magnetic nanomaterials for hyperthermia-based therapy and controlled drug delivery," *Adv Drug Deliver Rev* 63(9), 789-808 (2011)

20. C. C. Vernon, J. W. Hand, S. B. Field, D. Machin, J. B. Whaley, J. vanderZee, W. L. J. vanPutten, G. C. vanRhoon, J. D. P. vanDijk, D. G. Gonzalez, F. F. Liu, P. Goodman and M. Sherar, "Radiotherapy with or without hyperthermia in the treatment of superficial localized breast cancer: Results from five randomized controlled trials," *Int J Radiat Oncol* 35(4), 731-744 (1996)

21. P. K. Sneed, P. R. Stauffer, M. W. McDermott, C. J. Diedrich, K. R. Lamborn, M. D. Prados, S. Chang, K. A. Weaver, L. Spry, M. K. Malec, S. A. Lamb, B. Voss, R. L. Davis, W. M. Wara, D. A. Larson, T. L. Phillips and P. H. Gutin, "Survival benefit of hyperthermia in a prospective randomized trial of brachytherapy boost +/- hyperthermia for glioblastoma multiforme," *Int J Radiat Oncol* 40(2), 287-295 (1998)

22. T. M. Zagar, J. R. Oleson, Z. Vujaskovic, M. W. Dewhirst, O. I. Craciunescu, K. L. Blackwell, L. R. Prosnitz and E. L. Jones, "Hyperthermia combined with radiation therapy for superficial breast cancer and chest wall recurrence: A review of the randomised data," *Int J Hyperthermia* 26(7), 612-617 (2010)

23. S. Dromi, V. Frenkel, A. Luk, B. Traughber, M. Angstadt, M. Bur, J. Poff, J. W. Xie, S. K. Libutti, K. C. P. Li and B. J. Wood, "Pulsed-high intensity focused ultrasound and low temperature sensitive liposomes for enhanced targeted drug delivery and antitumor effect," *Clin Cancer Res* 13(9), 2722-2727 (2007)

24. S. T. Wang, V. Frenkel and V. Zderic, "Optimization of pulsed focused ultrasound exposures for hyperthermia applications," *J Acoust Soc Am* 130(1), 599-609 (2011)

25. J. Tu, J. H. Hwang, T. Chen, T. B. Fan, X. S. Guo, L. A. Crum and D. Zhang, "Controllable in vivo hyperthermia effect induced by pulsed high intensity focused ultrasound with low duty cycles," *Appl Phys Lett* 101(12), 124102 (2012)

26. Y. Ni, S. Mulier, Y. Miao, L. Michel and G. Marchal, "A review of the general aspects of radiofrequency ablation," *Abdom Imaging* 30(4), 381-400 (2005)

27. J. Z. Zhang, "Biomedical applications of shape-controlled plasmonic nanostructures: a case study of hollow gold nanospheres for photothermal ablation therapy of cancer," *J Phys Chem Lett* 1(4), 686-695 (2010)

28. X. W. Liu, H. Q. Tao, K. Yang, S. A. Zhang, S. T. Lee and Z. A. Liu, "Optimization of surface chemistry on single-walled carbon nanotubes for in vivo photothermal ablation of tumors," *Biomaterials* 32(1), 144-151 (2011)

29. H. Lukka, T. Waldron, J. Chin, L. Mayhew, P. Warde, E. Winquist, G. Rodrigues and B. Shayegan, "High-intensity focused ultrasound for prostate cancer: a systematic review," *Clin Oncol* 23(2), 117-127 (2011)

30. S. Crouzet, X. Rebillard, D. Chevallier, P. Rischmann, G. Pasticier, G. Garcia, O. Rouviere, J. Y. Chapelon and A. Gelet, "Multicentric oncologic outcomes of high-intensity focused ultrasound for localized prostate cancer in 803 patients," *Eur Urol* 58(4), 559-566 (2010)

31. L. Zhang, H. Zhu, C. B. Jin, K. Zhou, K. Q. Li, H. B. Su, W. Z. Chen, J. Bai and Z. B. Wang, "High-intensity focused ultrasound (HIFU): effective and safe therapy for hepatocellular carcinoma adjacent to major hepatic veins," *Eur Radiol* 19(2), 437-445 (2009)

32. R. O. Illing, J. E. Kennedy, F. Wu, G. R. ter Haar, A. S. Protheroe, P. J. Friend, F. V. Gleeson, D. W. Cranston, R. R. Phillips and M. R. Middleton, "The safety and feasibility of extracorporeal high-intensity focused ultrasound (HIFU) for the treatment of liver and kidney tumours in a Western population," *Brit J Cancer* 93(8), 890-895 (2005)

33. F. Wu, Z. B. Wang, W. Z. Chen, J. Bai, H. Zhu and T. Y. I. Qiao, "Preliminary experience using high intensity focused ultrasound for the treatment of patients with advanced stage renal malignancy," *J Urology* 170(6), 2237-2240 (2003)

34. M. Margreiter and M. Marberger, "Focal therapy and imaging in prostate and kidney cancer: high-intensity focused ultrasound ablation of small renal tumors," *J Endourol* 24(5), 745-748 (2010)

35. W. Z. Chen, H. Zhu, L. Zhang, K. Q. Li, H. B. Su, C. B. Jin, K. Zhou, J. Bai, F. Wu and Z. B. Wang, "Primary bone malignancy: effective treatment with high-intensity focused ultrasound ablation," *Radiology* 255(3), 967-978 (2010)

36. Z. Ram, Z. R. Cohen, S. Harnof, S. Tal, M. Faibel, D. Nass and S. E. Maier, "Magnetic resonance imaging-guided, high-intensity focused ultrasound for brain tumor therapy," *Neurosurgery* 59(5), 949-955 (2006)

37. J. Hindley, W. M. Gedroyc, L. Regan, E. Stewart, C. Tempany, K. Hynnen, N. Macdanold, Y. Inbar, Y. Itzchak, J. Rabinovici, K. Kim, J. F. Geschwind, G. Hesley, B. Gostout, T. Ehrenstein, S. Hengst, M. Sklair-Levy, A. Shushan and F. Jolesz, "MRI guidance of focused ultrasound therapy of uterine fibroids: Early results," *Am J Roentgenol* 183(6), 1713-1719 (2004)

38. L. Zhang, W. Z. Chen, Y. J. Liu, X. Hu, K. Zhou, L. Chen, S. Peng, H. Zhu, H. L. Zou, J. Bai and Z. B. Wang, "Feasibility of magnetic resonance imaging-guided high intensity focused ultrasound therapy for ablating uterine fibroids in patients with bowel lies anterior to uterus," *Eur J Radiol* 73(2), 396-403 (2010)

39. E. Martin, D. Jeanmonod, A. Morel, E. Zadicario and B. Werner, "High-intensity focused ultrasound for noninvasive functional neurosurgery," *Ann Neurol* 66(6), 858-861 (2009)

40. M. W. Dewhirst, B. L. Viglianti, M. Lora-Michiels, M. Hanson and P. J. Hoopes, "Basic principles of thermal dosimetry and thermal thresholds for tissue damage from hyperthermia," *Int J Hyperthermia* 19(3), 267-294 (2003)

41. I. Rivens, A. Shaw, J. Civale and H. Morris, "Treatment monitoring and thermometry for therapeutic focused ultrasound," *Int J Hyperthermia* 23(2), 121-139 (2007)

42. F. A. Jolesz, "MRI-guided focused ultrasound surgery," *Annu Rev Med* 60, 417-430 (2009)

43. V. Rieke and K. Butts Pauly, "MR thermometry," *J Magn Reson Imaging* 27(2), 376-390 (2008)

44. K. Hynynen, "MRI-guided focused ultrasound treatments," *Ultrasonics* 50, 221-229 (2010)

45. A. Chapman and G. ter Haar, "Thermal ablation of uterine fibroids using MR-guided focused ultrasound - a truly non-invasive treatment modality," *Eur Radiol* 17(10), 2505-2511 (2007)

46. F. M. Fennessy and C. M. Tempany, "A review of magnetic resonance imaging-guided focused ultrasound surgery of uterine fibroids," *Top Magn Reson Imaging* 17(3), 173-179 (2006)

47. K. Hynynen, O. Pomeroy, D. N. Smith, P. E. Huber, N. J. McDannold, J. Kettenbach, J. Baum, S. Singer and F. A. Jolesz, "MR imaging-guided focused ultrasound surgery of fibroadenomas in the breast: a feasibility study," *Radiology* 219(1), 176-185 (2001)

48. A. B. Holbrook, J. M. Santos, E. Kaye, V. Rieke and K. B. Pauly, "Real-time MR thermometry for monitoring HIFU ablations of the liver," *Magn Reson Med* 63(2), 365-373 (2010)

49. S. Roujol, M. Ries, B. Quesson, C. Moonen and B. Denis de Senneville, "Real-time MR-thermometry and dosimetry for interventional guidance on abdominal organs," *Magn Reson Med* 63(4), 1080-1087 (2010)

50. B. Quesson, C. Laurent, G. Maclair, B. D. de Senneville, C. Mougenot, M. Ries, T. Carteret, A. Rullier and C. T. Moonen, "Real-time volumetric MRI thermometry of focused ultrasound ablation in vivo: a feasibility study in pig liver and kidney," *NMR Biomed* 24(2), 145-153 (2011)

51. D. Kopelman, Y. Inbar, A. Hanannel, D. Freundlich, D. Castel, A. Perel, A. Greenfeld, T. Salamon, M. Sareli, A. Valeanu and M. Papa, "Magnetic resonance-guided focused ultrasound surgery (MRgFUS): Ablation of liver tissue in a porcine model," *Eur J Radiol* 59(2), 157-162 (2006)

52. F. Wu, "Extracorporeal high intensity focused ultrasound in the treatment of patients with solid malignancy," *Minim Invasiv Ther* 15(1), 26-35 (2006)

53. H. Furusawa, K. Namba, S. Thomsen, F. Akiyama, A. Bendet, C. Tanaka, Y. Yasuda and H. Nakahara, "Magnetic resonance-guided focused ultrasound surgery of breast cancer: Reliability and effectiveness," *J Am Coll Surgeons* 203(1), 54-63 (2006)

54. N. R. Owen, J. Y. Chapelon, G. Bouchoux, R. Berriet, G. Fleury and C. Lafon, "Dual-mode transducers for ultrasound imaging and thermal therapy," *Ultrasonics* 50(2), 216-220 (2010)

55. G. Fleury, G. Bouchoux, R. Berriet and C. Lafon, "Simultaneous imaging and therapeutic ultrasound," in *2006 IEEE Ultrasonics Symp Proc*, 1045-1051 (2006)

56. H. Zhong, M. X. Wan, Y. F. Jiang and S. P. Wang, "Monitoring imaging of lesions induced by high intensity focused ultrasound based on differential ultrasonic attenuation and integrated backscatter estimation," *Ultrasound Med Biol* 33(1), 82-94 (2007)

57. S. Y. Zhang, M. X. Wan, H. Zhong, C. Xu, Z. H. Liao, H. Q. Liu and S. P. Wang, "Dynamic changes of integrated backscatter, attenuation coefficient and bubble activities during high-intensity focused ultrasound (HIFU) treatment," *Ultrasound Med Biol* 35(11), 1828-1844 (2009)

58. R. H. Silverman, R. Muratore, J. A. Ketterling, J. Mamou, D. J. Coleman and E. J. Feleppa, "Improved visualization of high-intensity focused ultrasound lesions," *Ultrasound Med Biol* 32(11), 1743-1751 (2006)

59. R. E. Kumon, M. S. R. Gudur, Y. Zhou and C. X. Deng, "High-frequency ultrasound M-mode imaging for identifying lesion and bubble activity during high-intensity focused ultrasound ablation," *Ultrasound Med Biol* 38(4), 626-641 (2012)

60. R. Souchon, G. Bouchoux, E. Maciejko, C. Lafon, D. Cathignol, M. Bertrand and J. Y. Chapelon, "Monitoring the formation of thermal lesions with heat-induced echo-strain imaging: A feasibility study," *Ultrasound Med Biol* 31(2), 251-259 (2005)

61. J. Chenot, D. Melodelima, W. A. N'Djin, R. Souchon, M. Rivoire and J. Y. Chapelon, "Intra-operative ultrasound hand-held strain imaging for the visualization of ablations produced in the liver with a toroidal HIFU transducer: first in vivo results," *Phys Med Biol* 55(11), 3131-3144 (2010)

62. K. Nightingale, M. S. Soo, R. Nightingale and G. Trahey, "Acoustic radiation force impulse imaging: In vivo demonstration of clinical feasibility," *Ultrasound Med Biol* 28(2), 227-235 (2002)

63. F. L. Lizzi, R. Muratore, C. X. Deng, J. A. Ketterling, S. K. Alam, S. Mikaelian and A. Kalisz, "Radiation-force technique to monitor lesions during ultrasonic therapy," *Ultrasound Med Biol* 29(11), 1593-1605 (2003)

64. R. Maass-Moreno and C. A. Damianou, "Noninvasive temperature estimation in tissue via ultrasound echo-shifts. 1. Analytical model," *J Acoust Soc Am* 100(4), 2514-2521 (1996)

65. R. Maass-Moreno, C. A. Damianou and N. T. Sanghvi, "Noninvasive temperature estimation in tissue via ultrasound echo-shifts. 2. In vitro study," *J Acoust Soc Am* 100(4), 2522-2530 (1996)

66. C. Simon, P. Vanbaren and E. S. Ebbini, "Two-dimensional temperature estimation using diagnostic ultrasound," *IEEE Trans Ultrason Ferroelectr Freq Control* 45(4), 1088-1099 (1998)

67. D. Liu and E. S. Ebbini, "Real-time 2-D temperature imaging using ultrasound," *IEEE Trans Biomed Eng* 57(1), 12-16 (2010)

68. R. Seip, P. VanBaren, C. A. Cain and E. S. Ebbini, "Noninvasive real-time multipoint temperature control for ultrasound phased array treatments," *IEEE Trans Ultrason Ferroelectr Freq Control* 43(6), 1063-1073 (1996)

69. A. Anand, D. Savery and C. Hall, "Three-dimensional spatial and temporal temperature imaging in gel phantoms using backscattered ultrasound," *IEEE Trans Ultrason Ferroelectr Freq Control* 54(1), 23-31 (2007)

70. T. Varghese, J. A. Zagzebski, Q. Chen, U. Techavipoo, G. Frank, C. Johnson, A. Wright and F. T. Lee, "Ultrasound monitoring of temperature change during radiofrequency ablation: preliminary in-vivo results," *Ultrasound Med Biol* 28(3), 321-329 (2002)

71. W. L. Straube and R. M. Arthur, "Theoretical estimation of the temperature-dependence of backscattered ultrasonic power for noninvasive thermometry," *Ultrasound Med Biol* 20(9), 915-922 (1994)

72. R. M. Arthur, D. Basu, Y. Z. Guo, J. W. Trobaugh and E. G. Moros, "3-D in vitro estimation of temperature using the change in backscattered ultrasonic energy," *IEEE Trans Ultrason Ferroelectr Freq Control* 57(8), 1724-1733 (2010)

73. P. H. Tsui, Y. T. Chien, H. L. Liu, Y. C. Shu and W. S. Chen, "Using ultrasound CBE imaging without echo shift compensation for temperature estimation," *Ultrasonics* 52(7), 925-935 (2012)

74. A. N. Amini, E. S. Ebbini and T. T. Georgiou, "Noninvasive estimation of tissue temperature via high-resolution spectral analysis techniques," *IEEE Trans Biomed Eng* 52(2), 221-228 (2005)

75. N. R. Miller, J. C. Bamber and P. M. Meaney, "Fundamental limitations of noninvasive temperature imaging by means of ultrasound echo strain estimation," *Ultrasound Med Biol* 28(10), 1319-1333 (2002)

76. X. Zheng and S. Vaezy, "An acoustic backscatter-based method for localization of lesions induced by high-intensity focused ultrasound," *Ultrasound Med Biol* 36(4), 610-622 (2010)

CHAPTER 2

Evaluation of ultrasound thermometry during focused ultrasound heating using infrared thermography

Successful ultrasound temperature estimation relies on 1) accurate calibration between changes in ultrasound backscattered signal and temperature increase and 2) validation of signal processing methods. However, traditional temperature measurements using thermocouples lack spatial information and calibration done using water-bath heating is time-consuming. In this chapter, we proposed to use non-contact infrared (IR) thermography with high spatial and temporal resolution to facilitate fast calibration and validation of ultrasound thermometry methods. To demonstrate the new evaluation platform, experiments were performed with simultaneous acquisition of two dimensional (2D) ultrasound backscattered signal (B-mode imaging) and IR temperature measurement on the surface plane of a phantom subjected to focused ultrasound (FUS) heating, with an investigated temperature ranged from 20 °C to 35 °C. Although in this study FUS was applied as the heat source and ultrasound processing methods using echo time shifts was used, the developed platform using IR thermography can also be applied to developing ultrasound thermometry for other types of thermal therapies and data processing methods.

2.1 Introduction

For accurate temperature estimation using ultrasound imaging, all methods require calibrations in advance as the temperature dependency of the parameters used (e.g., backscatter energy, speed of sound) are all tissue type specific. The calibrations are typically performed either with uniform heating in water-bath[1-4] or with thermocouples inserted at multiple discrete locations in the specimen within the field of view of ultrasound imaging.[5] Water-bath heating requires a longer time for the specimen to reach a uniform temperature distribution (e.g., for a 20 °C temperature range, measurements can take several hours[1]). This method is inefficient if a large calibration database for all different tissue types is needed. Thermocouples, besides being invasive, disrupt energy propagation during thermal heating and the viscous heating and thermal conduction by thermocouples themselves may introduce error in measurements, which are most significant in FUS applications.[6-9]

In ultrasound thermometry, signal processing methods are also critical as their design and implementation greatly affect the accuracy of temperature estimation. Spatial resolution is particularly important for thermal therapies targeted at a small treatment volume where the induced temperature gradient is steep. However, validation done using thermocouples can only evaluate temperature estimations at sparse locations[1,2] and is insufficient for optimal design of algorithms. Therefore to develop robust ultrasound thermometry methods and to investigate their individual performances and limitations, a new evaluation platform for rapid calibration and validation with high spatial and temporal temperature measurement is necessary.

Infrared (IR) thermography, although limited to surface measurements, can obtain accurate measurements of temperature changes as a function of space and time directly without contact. The advantages also include easy implementation, high temporal (> 100 Hz) and spatial resolution (< 100 μm). It typically uses the mid-IR ($3 – 5\,\mu$m) and long-IR ($8 – 12\,\mu$m) spectrum which have sufficient sensitivity for thermal imaging.[10] IR thermography has been used for diagnosis and treatment monitoring, as demonstrated by medical applications such as oncology (breast cancer, skin diseases), skin burns, vascular disorders, surgery, tissue viability, sports medicine, and mass screening.[10-14]

For FUS-related studies, IR thermography has been used to visualize the locations and extent of heat deposition with various target geometries and/or using different designs of FUS transducers.[15-17] It has also been proposed as a new technique to calibrate transducers faster than traditional hydrophone field scans.[18,19] It has also been applied to record temperature profiles during FUS exposures to evaluate and optimize ultrasound parameters.[20,21] However, IR thermography has not been applied to the development of ultrasound thermometry.

Our goal for this study is to investigate the feasibility of IR thermography in calibrating and evaluating ultrasound thermometry during FUS heating with spatiotemporal temperature information unavailable with traditional thermocouple measurements. We conducted experiments using two types of phantom, tissue-mimicking and fat-mimicking, to investigate their differences in changes in the speed of sound as a function of temperature. Simultaneous IR thermography and B-mode ultrasound imaging were used to measure the spatiotemporal temperature and ultrasound backscattered signal on the same surface plane of the phantoms before, during, and after FUS exposures. A simple echo time shifts method

using cross-correlation speckle tracking was chosen for ultrasound thermometry due to its wide use. The ultrasound echo time shifts and IR measured temperature were first used for material-dependent calibration for each phantom type. Then the calibration results were used for ultrasound temperature estimation and the spatiotemporal error was determined by comparing with the IR measurement.

2.2 Materials and methods

2.2.1 Theory: ultrasound echo time shifts

When neglecting the thermal expansion effect in the specimen, the time of arrival τ of the ultrasound backscattered signal from axial depth y is expressed as $\tau(y) = 2\int_0^y \frac{1}{c(\theta(\xi))} d\xi$, where $c(\theta(\xi))$ is the speed of sound at depth ξ with temperature $\theta(\xi)$.

In the case of FUS heating, if isotropic free thermal expansion in the specimen is considered, the specimen will expand in both directions outward from the center of the heating zone. To derive τ from an ultrasound scatterer subjected to FUS heating, the ultrasound beam path can be divided into two segments as shown in Fig. 2.1: the first segment is the temperature constant zone from the transducer surface ($y = 0$) to y_0 where no temperature changes occur, and the second segment is the heating zone from $y \geq y_0$ with temperature changes $\delta\theta(\xi)$ at each depth ξ. For an ultrasound scatterer at depth y before heating, the baseline time of arrival $\tau_0(y)$ is

$$\tau_0(y) = \frac{2y_0}{c_0} + 2\int_{y_0}^{y} \frac{1}{c_0} d\xi, \tag{2.1}$$

where c_0 is the speed of sound at baseline temperature θ_0, and y_0 can be further expressed using the focus or center of the focal zone y_c: $y_0 = y_c - \int_{y_0}^{y_c} d\xi$. After heating, the scatterer shifts to depth y' with a time of arrival $\tau(y')$ now being

$$\tau\left(y'\right) = \frac{2y_0'}{c_0} + 2\int_{y_0}^{y} \frac{\left(1+\alpha_t\left(\theta\left(\xi\right)\right)\cdot\delta\theta\left(\xi\right)\right)}{c\left(\theta\left(\xi\right)\right)} d\xi\,, \tag{2.2}$$

where y_0' is the location y_0 expands to, expressed as $y_0' = y_c - \int_{y_0}^{y_c}\left(1+\alpha_t\left(\theta\left(\xi\right)\right)\cdot\delta\theta\left(\xi\right)\right)\cdot d\xi$. $\alpha_t(\theta(\xi))$ is the linear coefficient of thermal expansion at depth ξ with temperature $\theta(\xi)$. The echo time shift $\delta\tau(y)$ can then be computed by subtracting Eq. (2.2) from Eq. (2.1):

$$\begin{aligned}\delta\tau\left(y\right) &= \tau\left(y'\right) - \tau_0\left(y\right) \\ &= -\frac{2}{c_0}\int_{y_0}^{y_c}\left[\alpha_t\left(\theta\left(\xi\right)\right)\cdot\delta\theta\left(\xi\right)\right]d\xi + 2\int_{y_0}^{y}\left[\frac{\left(1+\alpha_t\left(\theta\left(\xi\right)\right)\cdot\delta\theta\left(\xi\right)\right)}{c\left(\theta\left(\xi\right)\right)} - \frac{1}{c_0}\right]d\xi\end{aligned}. \tag{2.3}$$

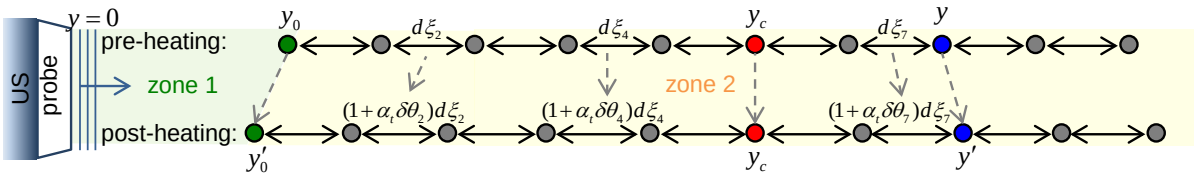

Figure 2.1 Diagram of ultrasound echo time shifts after FUS heating. zone 1 is the temperature constant zone from the transducer surface ($y = 0$) to y_0; zone 2 is the heating zone. $d\xi$ denotes the distance between two scatters, α_t the linear coefficient of thermal expansion, $\delta\theta$ the temperature change, and y_c the location of the spatial peak temperature rise.

Ultrasound thermometry. Differentiating Eq. (2.3) by the depth variable *y*, we get the time shift gradient $\partial(\delta\tau(y))/\partial y$:

$$\frac{\partial\left(\delta\tau\left(y\right)\right)}{\partial y}=2\left[\frac{\left(1+\alpha_t\left(\theta\left(y\right)\right)\cdot\delta\theta\left(y\right)\right)}{c\left(\theta\left(y\right)\right)}-\frac{1}{c_0}\right], \tag{2.4}$$

where the first term in Eq. (2.3) disappears since it is independent of *y*. For most biological materials at a lower temperature range (20 °C – 40 °C), a linear relation between speed of sound and temperature can usually be assumed:[22,23]

$$c\left(\theta\left(y\right)\right)=c_0\cdot\left(1+\beta\cdot\delta\theta\left(y\right)\right), \tag{2.5}$$

where $\beta=\frac{1}{c_0}\frac{\partial c\left(y,\theta\right)}{\partial\theta}\bigg|_{\theta=\theta_0}$. Although the linear coefficient of thermal expansion α_t is itself a function of temperature,[22] for simplicity we assumed it a constant over the temperature range under investigation. Using the fact that $\left|\beta\cdot\delta\theta\left(y\right)\right|\ll 1$ and the assumption of constant α_t, Eq. (2.4) can be rewritten to

$$\frac{\partial\left(\delta\tau\left(y\right)\right)}{\partial y}\approx\frac{2}{c_0}\cdot\left(\alpha_t-\beta\right)\cdot\delta\theta\left(y\right). \tag{2.6}$$

Eq. (2.6) is the same as derived by Simon et al.,[1] and hence $\partial(\delta\tau(y))/\partial y$ is used to estimate the temperature changes by

$$\delta\theta\left(y\right)=\frac{c_0}{2}\cdot k\cdot\frac{\partial\left(\delta\tau\left(y\right)\right)}{\partial y}, \tag{2.7}$$

where $k = 1/(\alpha_t - \beta)$ is material dependent and needs to be pre-calibrated.

Calibration. To empirically determine *k*, Eq. (2.7) is integrated from y_0 to depth *y*:

$$\int_{y_0}^{y}\delta\theta\left(\xi\right)\cdot d\xi=\frac{c_0}{2}\cdot k\cdot\int_{y_0}^{y}\frac{\partial\left(\delta\tau\left(\xi\right)\right)}{\partial\xi}\cdot d\xi=\frac{c_0}{2}\cdot k\cdot\left[\delta\tau\left(y\right)-\delta\tau\left(y_0\right)\right]=a\cdot\delta\tau\left(y\right)+b, \tag{2.8}$$

where $a = c_0 \cdot k/2$ and $b = -\delta\tau(y_0) \cdot c_0 \cdot k/2$. a and b can be determined by fitting a linear curve to $\delta\tau(y)$ and $\int_{y_0}^{y} \delta\theta(\xi) \cdot d\xi$ given available ultrasound backscatter data and spatial temperature distribution measured with IR thermography. The reason that Eq. (2.7) is not used directly for calibration is to prevent large noise and errors when taking the derivative of $\delta\tau(y)$ directly. $\delta\theta(\xi)$ measured by IR thermography usually has a smooth distribution which allows the integration in Eq. (2.8).

2.2.2 Phantom fabrication

The surface of the phantom had to be exposed to air to enable IR imaging, therefore to perform ultrasound imaging simultaneously with its probe out of the water (the probe used cannot be completely immersed in water), agar-based molds were first fabricated to allow for acoustic coupling between the phantom and the probe. The agar-based molds were made with 1% g/ml agar powder and deionized water. After the molds completely solidified, phantoms with desired acoustic and thermal properties were made inside the molds. Two different types of phantoms were fabricated: one was a water-based graphite-in-gelatin phantom to mimic typical biological tissue, and the other was an oil-based fat-mimicking phantom. These two phantoms were chosen due to their differences in speed of sound and thermal expansion as a function of temperature.

Tissue-mimicking phantom. The graphite-in-gelatin phantom[24] was constructed using 0.1 g/ml gelatin powder, 0.07 g/ml graphite powder, 0.0024 g/ml p-toluic acid, and 7% 2-propanol mixed in deionized water. The mixture was heated slowly on a hot plate with magnetic stirrer until the solution was clear. The solution was placed in a vacuum chamber for several minutes to remove gas bodies before it was poured into the agar mold.

Fat-mimicking phantom. To construct the fat-mimicking phantom,[25] a gelatin solution and an oil solution were heated separately before mixing them together. The gelatin solution consisted of 0.1 g/ml gelatin powder and 1.67% 2-propanol in deionized water, and the oil solution consisted of 25% olive oil and 16.67% castor oil (all concentrations were calculated based on the final mixture volume). After the gelatin solution became clear, the oil solution was slowly mixed into the gelatin solution, during which 1.67% detergent was also added. The mixture was stirred thoroughly. Again the mixture was placed in the vacuum chamber for several minutes to remove gas bodies before it was poured into the agar mold.

Emissivity measurement. Emissivity determines the efficiency of a body to radiate and absorb energy, and is defined as the ratio of the radiation emitted by the object to the radiation emitted by a blackbody at the same temperature.[26] It is a dimensionless parameter with a value between 0 and 1 with 1 being a perfect blackbody. For accurate conversion from IR radiance to temperature, knowledge of the emissivity of the imaged object is required. Therefore we first measured the emissivity of the two phantom types using the black tape method[27] with an IR camera (Silver 5600, FLIR Systems, Boston, MA, USA) perpendicular to the phantom surface. The Scotch Super 33+ Vinyl Electrical Tape (3M Company, St. Paul, MN) with a known emissivity of 0.95 was used. The importance of accurate measurement of emissivity and the ambient temperature to determining object temperature is further discussed in the Appendix.

2.2.3 Ultrasound system, IR imaging, and FUS heating

The experimental setup (Fig. 2.2A) consisted of the same IR camera used for emissivity measurement, an ultrasound imaging system, and a FUS system. The IR camera is sensitive to the mid-IR wavelength (3 – 5 μm), with a temperature measurement accuracy of ± 1 °C and a resolution of 0.01 °C. IR imaging was performed using one integration (exposure) times for measurements ranging from 10 °C to 60 °C, and conversion from IR radiance to temperature was performed using the manufacturer's calibration and non-uniformity corrections. The ultrasound imaging system (Vevo 770; Visualsonics, Toronto, ON, Canada) used had a high-frequency scanhead (RMV 707B, 30 MHz center frequency, 12.7 mm focal distance, 2.2 mm depth of focus [−6 dB], 55 μm axial resolution, 115 μm lateral resolution). The raw radiofrequency (RF) backscattered signals from the RF output port of the Vevo system were acquired by a digitizing oscilloscope (54830B, Agilent, Santa Clara, CA) at 500 Msample/s. The FUS system consisted of a FUS transducer (3.98 MHz center frequency, F = 1, Blatek, Inc., State College, PA), a function generator (33220A, Agilent), and a power amplifier (75A250, Amplifier Research, Souderton, PA). The FUS transducer was calibrated using a hydrophone (HNR-0500, Onda, Sunnyvale, CA) and its −6 dB focal width and focal length were measured as 0.7 mm and 5 mm, respectively.

Experiments were performed with the FUS transducer submerged in water facing up towards the phantom. The top surface of the phantom was above the water level to allow temperature measurement with the IR camera positioned above the phantom facing downward. The ultrasound imaging probe was placed horizontal and close to the phantom surface (Fig. 2.2B) to image the same plane as the IR measurement. To align the IR and ultrasound images, a thin metal wire visible under both imaging modalities was bent to

90 degrees with one edge inserted into the phantom and the other edge placed on the phantom surface. For synchronization, the "line trigger" and "frame trigger" output signals from the Vevo system were used to trigger the oscilloscope, FUS system, and IR camera through a delay-pulse generator (Model 565, Berkeley Nucleonics Corp., San Rafael, CA).

The B-mode images consisted of 32 A-lines with a separation of 27.5 μm between each pair of A-lines and were acquired at 34.4 Hz frame rate. The FUS exposures (34.4 Hz pulse repetition frequency, 51.7 % duty cycle, 0.84 s total duration, focus intensity 180 – 700 W/cm^2) were initiated 12 ms after the B-mode "frame trigger" to interleave with the imaging pulses to prevent interference. B-mode images were acquired for 6 frames before, 30 frames during, and 27 frames after FUS exposures. IR images of the phantom surface were acquired continuously for the entire time course at 50 Hz frame rate. 4 sets of experiments were performed on the tissue phantom, and 5 were on the fat phantom. All experiments were conducted at room temperature (20 °C).

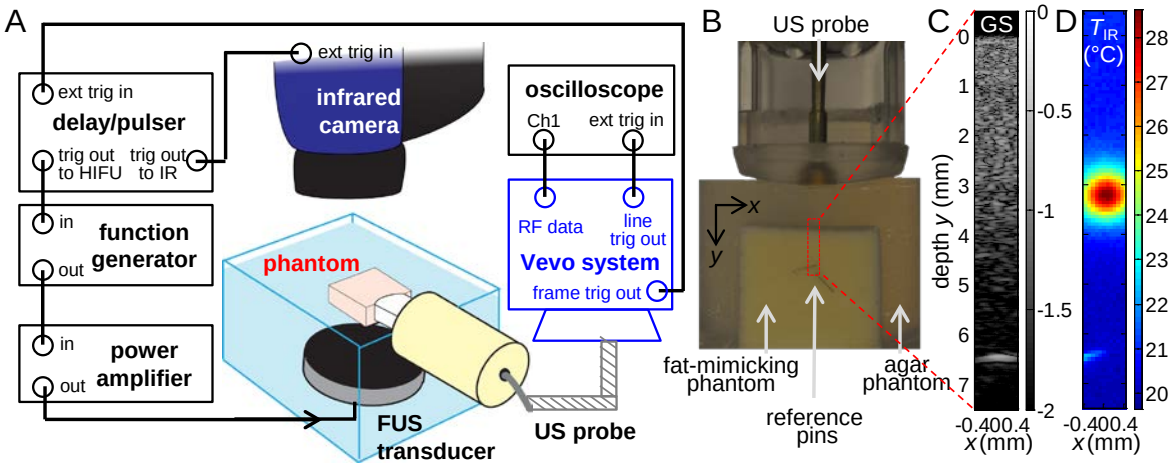

Figure 2.2 (A) Schematic illustration of experimental setup. (B) Photo of the ultrasound (US) probe and fat-mimicking phantom embedded in an agar mold. The region of interest is indicated by the red box. (C) and (D) show the corresponding ultrasound gray scale (GS) image and IR-measured temperature T_{IR}. The alignment reference pin can be seen on both images at around 6.3 mm depth.

2.2.4 Image and data analysis

All image analysis and computations were performed using MATLAB (R2012a, Mathworks, Natick, MA) offline. The time information for both the IR and ultrasound images was shifted so that time $t = 0$ corresponded to the start of FUS exposures. The orientation of the x- and y-axis are shown in Fig. 2.2B, with $x = 0$ corresponding to the center A-line of the B-mode image and $y = 0$ corresponding to the phantom-agar mold interface. We applied the 1D model presented in Sec. 2.2.1 to each A-line in the B-mode image, therefore in the following equations, the notation of location 'x' is only included when 2D spatial interpolation or filtering is involved.

Temperature increase. The temperature increase ΔT_{IR} at location (x, y) at time t was calculated from the IR measured temperature T_{IR} by

$$\Delta T_{\mathrm{IR}}(x, y, t) = T_{\mathrm{IR}}(x, y, t) - T_0(x, y, t \le 0), \tag{2.9}$$

where $T_0(x, y, t \le 0)$ is the baseline temperature averaged from –0.62 s to 0 s before FUS was turned on. The cumulative temperature rise up to depth y in Eq. (2.8) was denoted as $\mathrm{cum}[\Delta T_{\mathrm{IR}}(y)]$, and computed using

$$\int_{y_0}^{y} \delta\theta(\xi) \cdot d\xi \approx \sum_{y_0}^{y} \Delta T_{\mathrm{IR}}(y) \cdot \Delta y_{\mathrm{IR}} = \mathrm{cum}\left[\Delta T_{\mathrm{IR}}(y)\right], \tag{2.10}$$

where Δy_{IR} is the pixel size on the IR images, and y_0 was chosen at a depth with $\Delta T_{\mathrm{IR}}(y \le y_0) = 0$.

To compare with the ultrasound data, $\Delta T_{\mathrm{IR}}(x, y)$ and $\mathrm{cum}[\Delta T_{\mathrm{IR}}(x, y)]$ at each t was linearly interpolated to have the same resolution as the B-mode image (interp2.m function in MATLAB). After interpolation, the center peak temperature rise, $\max[\Delta T_{\mathrm{IR}}(y)]$, along each

A-line was determined. The spatial location of 'focus' (x_f, y_f) was also determined by $\left(x_f, y_f\right) = \arg\max_{x,y}\left[\Delta T_{\mathrm{IR}}\left(x, y, t = \mathrm{FUS\ end}\right)\right]$.

Speed of sound. The location of the tip of the reference metal wire y_{ref} was first determined from the IR image, then the time of arrival of the RF signal from the corresponding A-line was used to compute the baseline speed of sound c_0 in the phantom using

$$c_0 = \frac{2 \cdot y_{\mathrm{ref}}}{\tau(y_{\mathrm{ref}}) - \tau(y = 0)}, \tag{2.11}$$

where $\tau(y_{\mathrm{ref}})$ and $\tau(y = 0)$ is the time of arrival of the RF signal from the reference wire and the phantom-agar mold interface, respectively.

Echo time shifts. For each dataset, a reference frame was first computed using the mean of the 6 pre-FUS frames. To calculate $\delta\tau(y)$, the A-lines in each B-mode image were compared to the corresponding A-lines in the reference frame using the cross-correlation function. A tracking window $n = 80$ points was used (~2.4 λ, where λ is the wavelength of the imaging transducer). A fourth-order polynomial was fitted to the 11 points around the point with the maximum cross-correlation value, and the location of the final maximal with a finer spatial resolution was determined as the displacement. $\delta\tau(y)$ was then calculated by dividing the displacement with the sampling rate. Data points with RF signal amplitude smaller than 5 mV were removed to reduce noise.

Thermometry calibration. Eq. (2.8) can now be rewritten as $\mathrm{cum}[\Delta T_{IR}(y)] = a \cdot \delta\tau(y) + b$. a and b was determined by fitting a linear curve for each A-line in each frame. To minimize error from locations with small temperature rise, only the region with temperatures greater than $0.2 \times \max[\Delta T_{IR}(y)]$ was used for the fitting. This region is denoted as "focal width" in this chapter. The R-squared value ($R^2_{a,b}$), which is indicative of how well the data points fit the line, was recorded so that only cases with a good fit were used for statistical analysis.

Evaluation of temperature estimation. For temperature estimation, a 10^{th} order polynomial was fitted to $\delta\tau(y)$ computed using the cross-correlation method. The chosen order of polynomial fit was within the range used in Seip et al.'s work (polynomial of order between 8 and 14).[28] The fitted polynomial was then differentiated along y to obtain the gradient of echo time shifts $\partial(\delta\tau(y))/\partial y$. Since all experiments were performed at the same room temperature, the speed of sound c_0 at the baseline temperature was the same. Therefore, the estimated temperature was computed by multiplying $\partial(\delta\tau(y))/\partial y$ with a as in Eq. (2.7), where a was calibrated using Eq. (2.8). To evaluate the estimation error, leave-one-out cross validation (LOOCV) was employed in which each time one set of experiment was used as the validation set, and temperature was estimated by using the mean a calculated from the rest of the datasets.

2.3 Results

2.3.1 Emissivity of phantoms

The emissivity was measured to be 0.985 ± 0.017 (mean ± standard deviation (S.D.), n = 4) for the tissue-mimicking phantom and 0.823 ± 0.031 (n = 4) for the fat-mimicking phantom. Therefore for IR imaging in this study, emissivity was set to 0.99 and 0.82 for the tissue-mimicking and fat-mimicking phantom, respectively.

2.3.2 Speed of sound

Figures 2.2C and 2.2D show an example of the corresponding ultrasound gray scale (GS) and IR temperature image. The reference metal pin for image registration is visible on both images at depth ~6.3 mm. The baseline speed of sound c_0 (at 20.23 ± 0.28 °C) in tissue-mimicking and fat-mimicking phantom were 1581.3 ± 11.3 m/s (n = 4) and 1444.7 ± 9.7 m/s (n = 5), respectively. The mean value was used for subsequent data analysis.

2.3.3 Thermometry calibration

Figure 2.3 shows 1D examples of the calibration process using the IR and ultrasound data along depth y of the center line (x = 0) at t = 1 s (0.16 s after FUS was turned off) from one dataset for each phantom type. cum[$\Delta T_{IR}(y)$] (Figs. 2.3B and 2.3F), which was computed using the IR-measured $\Delta T_{IR}(y)$ (Figs. 2.3A and 2.3E), is compared against $\delta\tau(y)$ computed from the ultrasound RF data (Figs. 2.3C and 2.3F). The region with temperature rise greater than 0.2 × max[$\Delta T_{IR}(y)$] is indicated by the grey dashed lines, and the data within the region was used to fit for a and b as in Eq. (2.8) (Figs. 2.3D and 2.3H). As cum[$\Delta T_{IR}(y)$] increases along y, $\delta\tau(y)$ in the tissue-mimicking phantom becomes more negative (Fig. 2.3C), whereas $\delta\tau(y)$ in the fat-mimicking phantom becomes more positive (Fig. 2.3F). We also observed

that for a similar cum[ΔT_{IR}], the absolute echo time shifts $|\delta\tau|$ is 2 – 3 times higher in the tissue-mimicking phantom than in the fat-mimicking phantom.

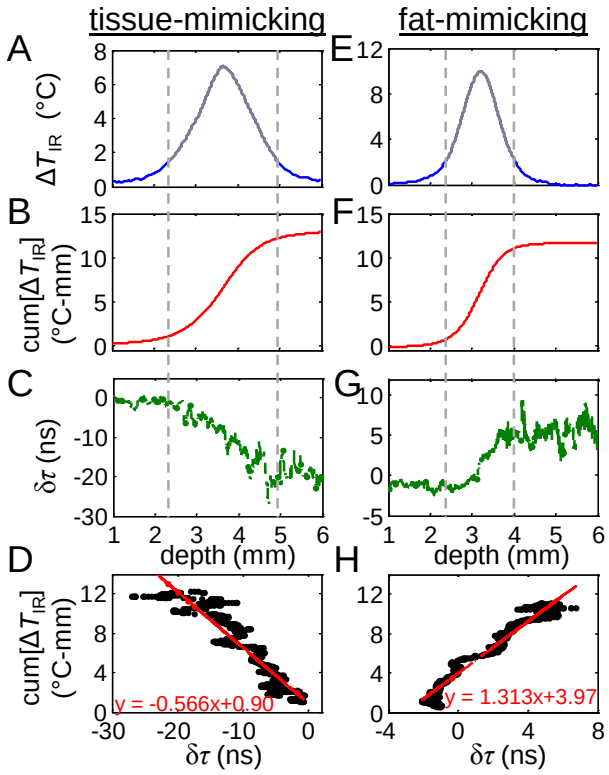

Figure 2.3 Examples of the calibration process: (A–D) are data from tissue-mimicking phantom and (E–H) from fat-mimicking phantom. (A, E) Temperature rise ΔT_{IR} measured by IR imaging. The dashed grey line indicates the region with temperature rise greater than 0.2 × max[ΔT_{IR}]. (B, F) Cumulative ΔT_{IR} along depth y, cum[ΔT_{IR}]. (C, G) Ultrasound echo time shifts $\delta\tau$. (D, H) Linear fit of cum[ΔT_{IR}] and $\delta\tau$.

Figure 2.4 shows a 2D spatiotemporal example of the calibration results for the tissue-mimicking phantom. During FUS exposures, the size of the heated region grows larger and the temperature rise becomes higher, as shown by the spatiotemporal evolution of ΔT_{IR} (Fig. 2.4A). The corresponding spatiotemporal evolution of cum[ΔT_{IR}] is shown in Fig. 2.4B. For better visualization, Fig. 2.4C shows a normalized echo time shifts $\delta\tau'(y)$ defined as

$$\delta\tau'(y) = \delta\tau(y) - \delta\tau(y_0), \tag{2.12}$$

where $\delta\tau(y_0)$ was computed by averaging $\delta\tau(0.5\text{ mm} \le y \le 1\text{ mm})$. Eq. (2.8) now becomes a simple scalar relation: cum[ΔT_{IR}] = $a \cdot \delta\tau'(y)$. Figure 2.4D shows ΔT_{IR} as a function of time at the focus (x_f, y_f), and 0.2 mm and 0.4 mm to the left of the focus (indicated by the white crosses in Fig. 2.4A). The corresponding a, and $R^2_{a,b}$ calculated for the corresponding A-lines containing these three locations are shown in Figs. 2.4E and 2.4F. The calibrated a reaches a more stable range of values around −0.60 °C-mm/ns after t = 0.5 s, corresponding to a higher $R^2_{a,b}$. An example for the fat-mimicking phantom is also shown in Fig. 2.5. Similarly, the calibrated a becomes more stable around 1.52 °C-mm/ns after t = 0.5 s, also corresponding to a higher $R^2_{a,b}$. The initial small cum[ΔT_{IR}] at the beginning of FUS exposure induced a small $\delta\tau$, which resulted in a low contrast-to-noise ratio (CNR) that was insufficient for good fitting. By considering fitting results with $R^2_{a,b} \ge 0.75$ from all A-lines in all frames, a = −0.59 ± 0.08 (°C-mm/ns) for the tissue-mimicking phantom (n = 4 sets of experiments, total of 5186 data points). Using the same criterion, a = 1.49 ± 0.27 (°C-mm/ns) for the fat-mimicking phantom (n = 5 sets of experiments, total of 5164 data points). Table 2.1 summarizes the calibrated a for the LOOCV, which was computed by excluding one dataset at a time.

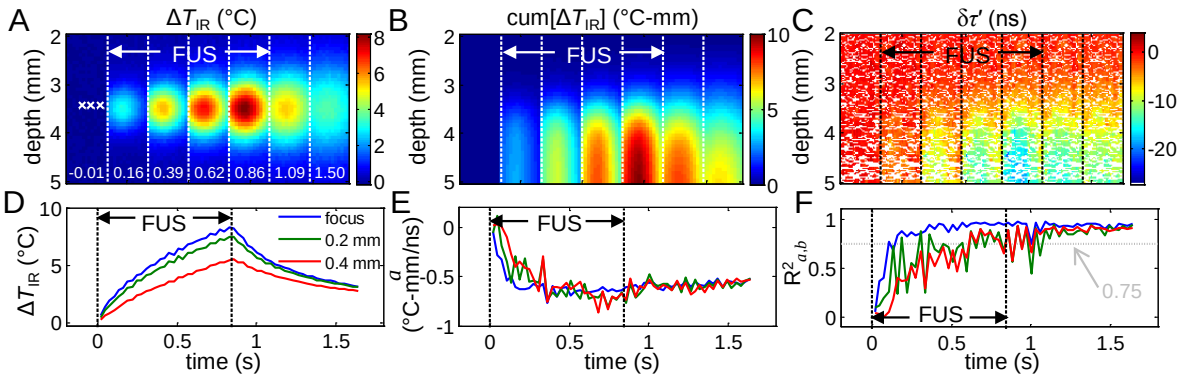

Figure 2.4 Example of calibration for tissue-mimicking phantom: (A) 2D temperature rise ΔT_{IR} before, during, and after FUS heating. The time is indicated in white numbers at the bottom of each frame in sec. (B) and (C) show the corresponding cum[ΔT_{IR}] and $\delta\tau'(y) = \delta\tau(y) - \delta\tau(y_0)$. (D) ΔT_{IR} over time at the focus, 0.2 mm and 0.4 mm to the left of focus. The three locations are indicated by the white crosses in the first frame in (A). (E) and (F) show the corresponding fitted a and $R^2_{a,b}$ along the A-lines containing these three locations.

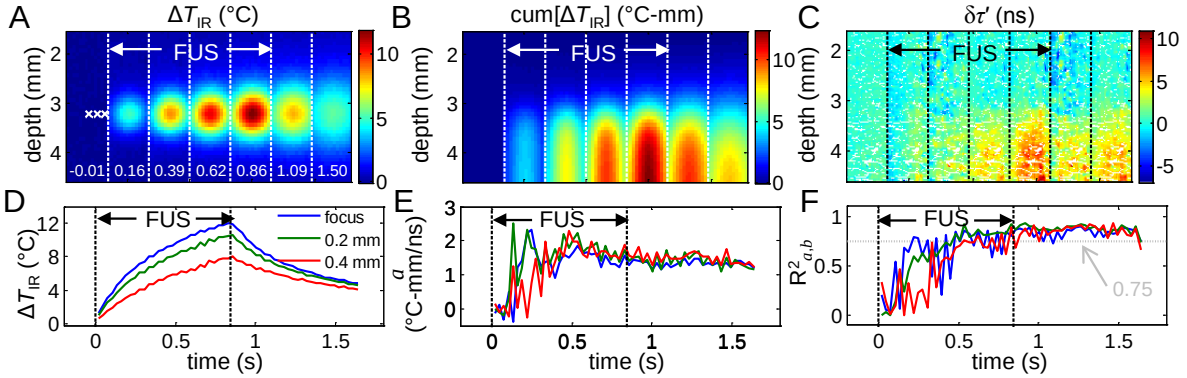

Figure 2.5 Example of calibration for fat-mimicking phantom: (A) 2D temperature rise ΔT_{IR} before, during, and after FUS heating. The time is indicated in white numbers at the bottom of each frame in sec. (B) and (C) show the corresponding cum[ΔT_{IR}] and $\delta\tau'(y) = \delta\tau(y) - \delta\tau(y_0)$. (D) ΔT_{IR} over time at the focus, 0.2 mm and 0.4 mm to the left of focus. The three locations are indicated by the white crosses in the first frame in (A). (E) and (F) show the corresponding fitted a and $R^2_{a,b}$ along the A-lines containing these three locations.

Table 2.1 Calibration coefficient for ultrasound temperature estimation

A. Tissue mimicking phantom

validate set	calibrate set	n points	*a* (°C-mm/ns)
1	2,3,4	3871	-0.6003 ± 0.0825
2	1,3,4	3630	-0.5927 ± 0.0832
3	1,2,4	3832	-0.5902 ± 0.0819
4	1,2,3	4225	-0.5862 ± 0.0710
-	-	-	-
	all	5186	-0.5922 ± 0.0797

B. Fat mimicking phantom

validate set	calibrate set	n points	*a* (°C-mm/ns)
1	2,3,4,5	4216	1.4812 ± 0.2662
2	1,3,4,5	3895	1.5059 ± 0.2775
3	1,2,4,5	4415	1.4656 ± 0.2623
4	1,2,3,5	4169	1.4832 ± 0.2705
5	1,2,3,4	3961	1.5206 ± 0.2678
	all	5164	1.4905 ± 0.2694

2.3.4 Evaluation of temperature estimation

Figure 2.6 shows 1D examples of ultrasound temperature estimation for the two phantom types at time points during and after FUS exposures. All figures are plotted using the center A-line ($x = 0$) from one dataset. Figs. 2.6A–D show $\delta\tau(y)$ and the 10th order polynomial fit. To compare with the polynomial fit, the fitted curve based on known temperature distribution measured by IR imaging is also plotted by rearranging Eq. (2.8):

$$\delta\tau_{\mathrm{IR}}(y) = \frac{\mathrm{cum}[\Delta T_{\mathrm{IR}}(y)] - b}{a}. \tag{2.13}$$

Again we see a decrease in $\delta\tau(y)$ with respect to y for the tissue-mimicking phantom and an increase for the fat-mimicking phantom. The estimated temperature increase ΔT_{US} calculated from differentiating the polynomial fit along y and multiplying the calibrated a in Table 2.1 was compared with the measured ΔT_{IR} (Figs. 2.6E–H). A better match between ΔT_{US} and ΔT_{IR} is seen on post-FUS results (Figs. 2.6F and 2.6H) compared to the during FUS results (Figs. 2.6E and 2.6G). A larger deviation between $\delta\tau_{\mathrm{IR}}(y)$ and the polynomial fit is observed for the fat-mimicking phantom, especially during FUS (Fig. 2.6C).

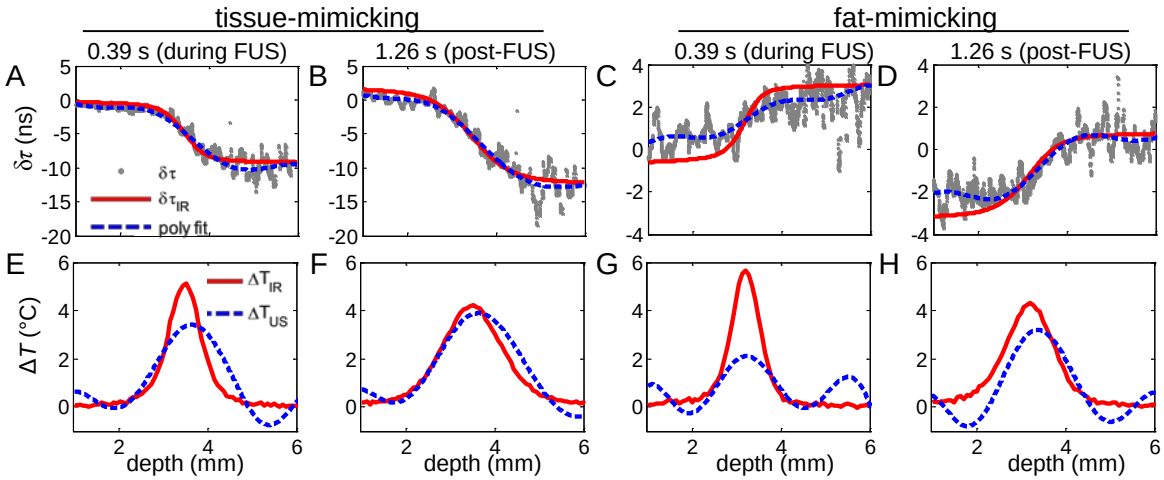

Figure 2.6 Examples of temperature estimation using echo time shifts with 10th order polynomial fitting. (A–D) Echo time shifts $\delta\tau$ determined directly from the ultrasound RF data, the 10th order polynomial fit, and the fit $\delta\tau_{IR}$ using IR measured temperature. (E–H) Corresponding IR measured temperature rise ΔT_{IR} and ultrasound estimated temperature rise ΔT_{US}.

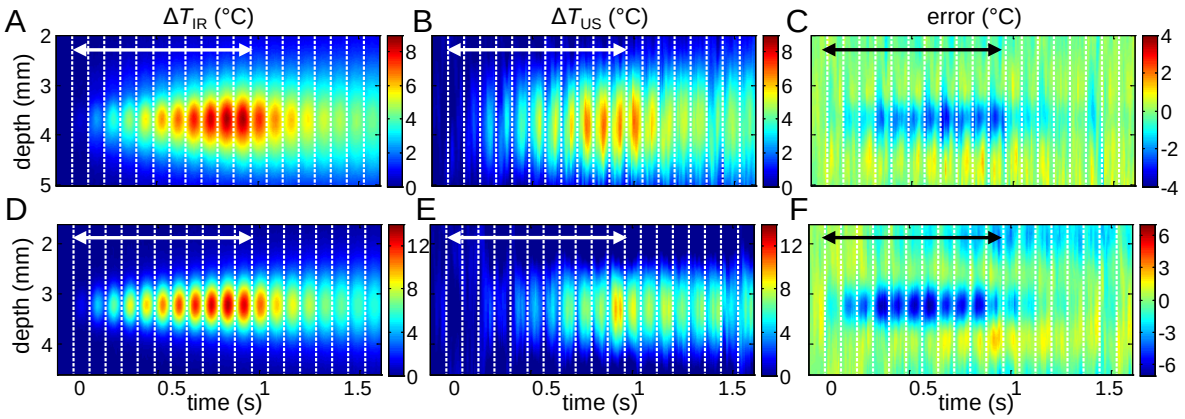

Figure 2.7 Evaluation of ultrasound temperature estimation: (A–C) one dataset from tissue-mimicking phantom and (D–F) one dataset from fat-mimicking phantom. (A, D) show the spatiotemporal evolution of temperature rise ΔT_{IR} measured by IR imaging. (B, E) The ultrasound estimated temperature rise ΔT_{US}. (C, F) Error = $\Delta T_{US} - \Delta T_{IR}$. The double-sided arrows indicate the time when FUS is on.

Figure 2.7 shows the 2D spatiotemporal ΔT_{IR} and ΔT_{US} from one dataset for each phantom type and the corresponding error: $\Delta T_{US} - \Delta T_{IR}$ (Figs. 2.7A–C: tissue-mimicking phantom; Figs. 2.7D–F: fat-mimicking phantom). In both phantom types, the error is largest during FUS exposure and at the center region of the focal zone (Figs. 2.7C and 2.7F). To evaluate the performance of temperature estimation from all datasets ($n = 4$ for tissue-mimicking phantom and $n = 5$ for fat-mimicking phantom), Fig. 2.8 shows the mean ± S.D. error at discrete locations: the focus, 0.25 mm and 0.5 mm away from the focus along the same A-line. The '+' and '-' signs in Fig. 2.8 indicate if the locations are towards or away from the imaging probe. The range of error in the tissue-mimicking phantom is smaller compared to that of fat-mimicking phantom. For both phantom types, the absolute error at the focus is the largest and increases during FUS exposures. However, when the FUS is off, the error quickly drops to close to zero.

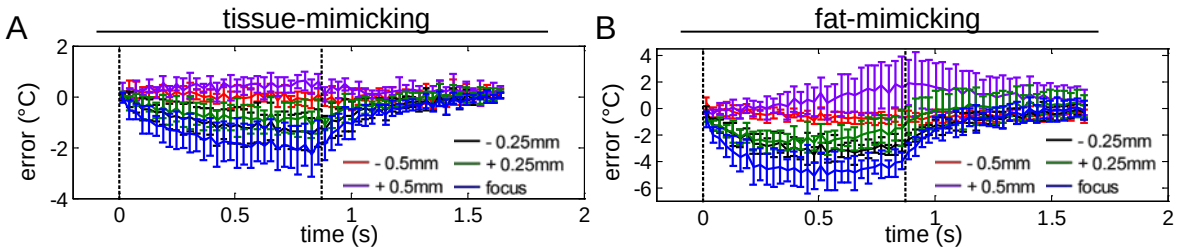

Figure 2.8 Statistical analysis of the ultrasound thermometry error: Mean ± S.D. of error at the focus, and ± 0.25 mm, ± 0.5 mm along the same A-line from the focus in (A) tissue-mimicking ($n = 4$) phantom and (B) fat-mimicking ($n = 5$) phantom. '+': further away from the imaging transducer; '–': towards the imaging transducer.

The main difference between the during FUS and post-FUS temperature distribution is the size of the focal width (defined as region with $\Delta T_{IR} \geq 0.2 \times \max[\Delta T_{IR}]$ along each A-line.). For example, Fig. 2.9A shows the temperature profiles along the axial depth with the same $\max[\Delta T_{IR}] = 5$ °C but different focal widths from one tissue-mimicking dataset. During FUS exposure, the focal width is smaller compared to that of post-FUS. To further investigate the effect of size of focal width on the temperature estimation accuracy, we computed the percentage error using

$$\text{error } \% = \frac{\Delta T_{US} - \Delta T_{IR}}{\Delta T_{IR}} \times 100\%, \tag{2.14}$$

and combined all A-lines with the same peak temperature at 5 ± 0.5 °C and plot their percentage error versus focal width as shown in Fig. 2.9B. A smaller absolute percentage error is observed for the post-FUS data with a bigger focal width.

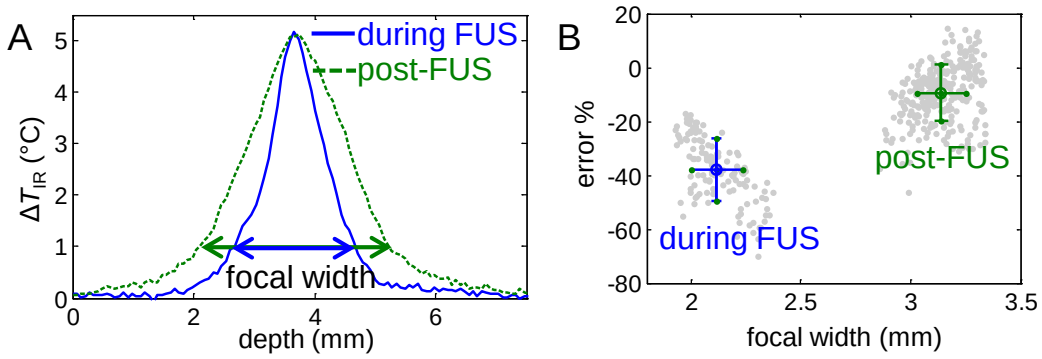

Figure 2.9 Effect of focal width on temperature estimation accuracy: example from one tissue-mimicking phantom dataset. (A) IR-measured temperature increase ΔT_{IR} along the axial depth for two A-lines during and post FUS exposure. The peak temperature is 5 °C for both A-lines. (B) Percentage error versus focal width for all A-lines with the same peak temperature = 5 ± 0.5 °C.

When combining all A-lines with varying peak temperature and from all n = 4, the relation between focal width and error % (Fig. 2.10) still shows that the temperature estimation becomes much accurate when the focal width is larger. Similar result is observed for the fat-mimicking phantom.

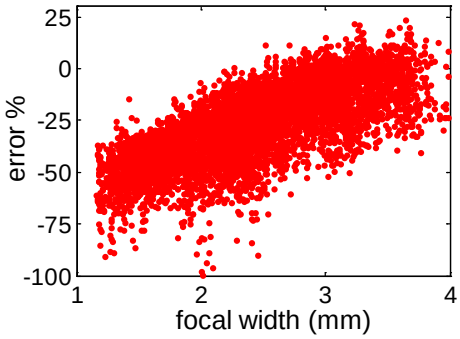

Figure 2.10 Percentage error as a function of focal width for the tissue-mimicking phantom.

2.4 Discussion

In this study, we investigated the applicability of IR thermography in developing ultrasound thermometry where FUS was used as an example thermal heating modality. Echo time shifts determined using 1D cross-correlation speckle tracking method were compared against the cumulative temperature rise along the same A-line to obtain the material-dependent coefficient for temperature estimation. The calibrated coefficient was then used for ultrasound thermometry through cross-validation, and the ultrasound estimation error was computed by comparing against the IR measured temperature.

2.4.1 Calibration of ultrasound thermometry

All methods for ultrasound thermometry require accurate calibration for the specimen being heated.[29] For example, in the echo time shifts method used in this study, the knowledge of the material dependent k is required. In methods using change of backscattered energy (CBE), it is also necessary to know how backscattered energy changes as a function of temperature for a specific type of specimen.[3] Although calibration done using water-bath heating can provide a smaller S.D. and/or error because of the larger heated volume, the time required for the water and sample to reach temperature equilibrium is long. In contrast, the fast calibration method we proposed using IR thermography only used FUS exposures with durations less than 1 s. However, given the small focal zone of the FUS transducer used in this study, $\text{cum}[\Delta T_{IR}] = \sum \Delta T_{IR} \cdot \Delta y$ only resulted in a small $\delta\tau$, particularly for the fat-mimicking phantom (Fig. 2.3F: on the order of several ns), which is very susceptive to noise. $\delta\tau$ becomes even noisier as depth increases due to the attenuated ultrasound signal strength. Therefore for calibration, we have chosen only data points within the center heating zone ($0.2 \times \max[\Delta T_{IR}]$) to minimize errors. This is also demonstrated by the more accurate calibration based on IR-measured temperature as the region of temperature rise ('focal width') increases, especially at time points during the cooling period when FUS is off. To further improve accuracy and minimize error, a FUS transducer with a larger focal zone can be used to heat up a bigger volume which will result in a larger $\delta\tau$.

To integrate ΔT_{IR} along the axial depth, we made an assumption that the speed of sound changes linearly as a function of temperature for these two phantom types (Eq. (2.5)). Indeed we observed that the calibrated a value was consistent with temperature distributions either at a higher ΔT_{IR} (e.g., Figs. 2.5D and 2.5E, $t = 1$ s) or a lower ΔT_{IR} ($t = 1.5$ s).

Phantoms which can sustain a higher temperature can be used in the future to further expand the method to calibrate quadratic relations between speed of sound and temperature rise in a wider temperature range.

The speed of sound and thermal expansion in most soft tissue (water-based) increase as temperature increases, whereas in fat (lipid-based) they both decrease as temperature increases.[22,23] These properties are comparable to the echo time shifts observed in the two phantom types used (Figs. 2.3C, 2.3F, 2.4C, 2.5C, 2.6A–D). One of the biggest challenges to apply ultrasound thermometry in clinical settings is the uncertainty of the content of the imaged tissue, and *in-vivo* calibration is generally unachievable. MRI also shares the same problem where its unreliable temperature measurement in fat still remains a challenge.[30] For tissue types that can be classified prior to thermal therapy, a database containing the corresponding calibration coefficients for each tissue type can greatly improve the accuracy of ultrasound temperature estimation. Using the fast calibration process with IR thermography, calibrations can be done on various different tissue types in a fast and systematic manner.

2.4.2 Validation of ultrasound thermometry

As shown in Fig. 2.9, at the same max[ΔT_{IR}], the temperature estimation has a much smaller error when the size of the focal width is wider, which appears after FUS was off. The observation is expected as even with known temperature profiles, the calibration fit becomes better with a higher $R^2_{a,b}$ after FUS was off. The use of a 10^{th} order polynomial to fit $\delta\tau$ and then taking the gradient of the polynomial can be considered equivalent to applying a narrowband differentiator directly to $\delta\tau$. In Simon et al.'s work,[1] a better spatial resolution of temperature estimation from $\delta\tau$ was observed when a broadband differentiator was applied at

the trade-off of increased amount of ripples. However, due to the small focal zone and small CNR in this work, we did not use broadband differentiators which preserve more noise. As a result, the temperature increase was underestimated within the focal zone during FUS exposure for both phantoms. To minimize noise and further improve performance, more advanced signal processing methods such as those using special filter designs can be employed.[31]

In previous ultrasound thermometry studies based on echo time shifts, a good agreement of temperature estimation and thermocouple measurement (~0.5 °C) was achieved. However, in these studies either water-bath experiments with uniform temperature distribution were performed or the HIFU transducers and ultrasound imaging probes were aligned with the same direction of ultrasound propagation. Therefore the focal width of the temperature increase along the imaging axial direction was on the order of several millimeter to centimeter scale.[1,29,32,33] No study has been able to investigate the limitation on the size of focal width for acceptable temperature estimation error due to the lack of spatial temperature information. In this study, we were able to investigate a sub-millimeter focal width by placing the HIFU transducer and imaging probe in a perpendicular configuration. As shown in Fig. 2.6A, when the focal width is small and CNR of $\delta\tau$ is small, a slight difference between the slope of the fitted polynomial and that of the fitted $\delta\tau_{\mathrm{IR}}$ in the focal zone results in a big difference in ΔT. Even after applying signal processing methods to minimize noise, there will still be a limitation on the size of the heating zone where temperature can be precisely estimated using ultrasound imaging. IR thermography has a high spatial resolution and can be easily applied to evaluate the performance of ultrasound thermometry as the size of heating zone varies. IR images acquired in this study had a pixel size of ~70 μm. In

contrast, thermocouples will not be sufficient to provide temperature information with a sub-millimeter spatial resolution. Our results also suggest that for ultrasound thermometry, the axial direction of the imaging plane should be selected to be along the direction which has the biggest focal width.

2.4.3 Temperature measurement errors

The accuracy of IR thermography in temperature measurement highly depends on the accuracy of the emissivity of the specimen, which is used to convert received radiation to temperature. The background temperature, which also adds to the total received radiation by the IR camera, also needs to be precisely measured to subtract its contribution.[34] Table 2.2 lists examples of the maximum temperature rise converted from the same IR radiation to temperature when different emissivity values (mean, mean + S.D., and mean − S.D.) were used. The maximum error in IR temperature measurement due to emissivity error is small (around ± 0.5°C) in this study. However, when the specimen of interest has a much lower emissivity (e.g., < 0.5), care must be taken because temperature conversion from IR radiation is more sensitive to emissivity error for low emissivity specimens (see Appendix).

Table 2.2 Emissivity on IR temperature measurement

	emissivity		max. ΔT_{IR}(°C)
tissue-mimicking	mean−S.D.	0.97	9.15
	mean	0.99	8.95
	mean+S.D.	1.00	8.85
fat-mimicking	mean−S.D.	0.79	8.48
	mean	0.82	8.17
	mean+S.D.	0.85	7.88

2.4.4 Limitations and future study

Although the developed evaluation platform for ultrasound thermometry using IR thermography provides high spatial and temporal temperature measurements unavailable with other tools and is easy to implement, there are still limitations to this technique. One of the main limitation is that the specimen has to have an accessible surface due to the limited penetration depth of IR light at thermal sensitive wavelengths. Therefore the technique is not applicable for deeply seated tissue parts inside our body. However, it can still be applied *in-vivo* to organs with accessible surface such as the skin. This is more advantageous compared to the current water-bath calibration and thermocouple validation methods, which are strictly restricted to *ex-vivo* specimens.

For future studies, the platform will be applied on real tissue to calibrate tissue specific properties and to investigate the threshold of CNR in tissue for accurate temperature estimation. We would also like to further investigate the effect of sizes of heating zone, which affects the CNR, on the temperature estimation.

2.5 Conclusions

The methods described herein suggest that fast calibration and validation of algorithms for ultrasound thermometry are possible with the use of IR thermography. Accuracy of thermometry calibration can be improved by applying a heat source capable of heating up a larger volume. The use of IR thermography also facilitates evaluation of spatial resolution of ultrasound thermometry. Although in this study FUS was chosen as the heat source and ultrasound processing methods using echo time shifts was used, IR thermography

has the potential to be applied to developing ultrasound thermometry for other types of thermal therapies and data processing methods.

2.6 References

1. C. Simon, P. Vanbaren and E. S. Ebbini, "Two-dimensional temperature estimation using diagnostic ultrasound," *IEEE Trans Ultrason Ferroelectr Freq Control* 45(4), 1088-1099 (1998)

2. H. L. Liu, M. L. Li, T. C. Shih, S. M. Huang, I. Y. Lu, D. Y. Lin, S. M. Lin and K. C. Ju, "Instantaneous frequency-based ultrasonic temperature estimation during focused ultrasound thermal therapy," *Ultrasound Med Biol* 35(10), 1647-1661 (2009)

3. R. M. Arthur, D. Basu, Y. Z. Guo, J. W. Trobaugh and E. G. Moros, "3-D in vitro estimation of temperature using the change in backscattered ultrasonic energy," *IEEE Trans Ultrason Ferroelectr Freq Control* 57(8), 1724-1733 (2010)

4. P. H. Tsui, Y. C. Shu, W. S. Chen, H. L. Liu, I. T. Hsiao and Y. T. Chien, "Ultrasound temperature estimation based on probability variation of backscatter data," *Med Phys* 39(5), 2369-2385 (2012)

5. R. Maass-Moreno, C. A. Damianou and N. T. Sanghvi, "Noninvasive temperature estimation in tissue via ultrasound echo-shifts .2. In vitro study," *J Acoust Soc Am* 100(4), 2522-2530 (1996)

6. W. J. Fry and R. B. Fry, "Determination of absolute sound levels and acoustic absorption coefficients by thermocouple probes - theory," *J Acoust Soc Am* 26(3), 294-310 (1954)

7. H. Morris, I. Rivens, A. Shaw and G. ter Haar, "Investigation of the viscous heating artefact arising from the use of thermocouples in a focused ultrasound field," *Phys Med Biol* 53(17), 4759-4776 (2008)

8. I. Rivens, A. Shaw, J. Civale and H. Morris, "Treatment monitoring and thermometry for therapeutic focused ultrasound," *Int J Hyperthermia* 23(2), 121-139 (2007)

9. R. L. Clarke and G. R. ter Haar, "Temperature rise recorded during lesion formation by high-intensity focused ultrasound," *Ultrasound Med Biol* 23(2), 299-306 (1997)

10. N. A. Diakides, M. Diakides, J. C. Lupo, J. L. Paul and R. Balcerak, "Advances in medical infrared imaging," in *Medical Infrared Imaging*, N. A. Diakides and J. D. Bronzino, Eds., 1-1-1-13, CRC Press, New York, NY (2008)

11. K. Ogan, W. W. Roberts, D. M. Wilhelm, L. Bonnell, D. Leiner, G. Lindberg, L. R. Kavoussi and J. A. Cadeddu, "Infrared thermography and thermocouple mapping of radiofrequency renal ablation to assess treatment adequacy and ablation margins," *Urology* 62(1), 146-151 (2003)

12. C. Song, B. Tang, P. A. Campbell and A. Cuschieri, "Thermal spread and heat absorbance differences between open and laparoscopic surgeries during energized dissections by electrosurgical instruments," *Surg Endosc* 23, 2480-2487 (2009)

13. E. Y. K. Ng, "A review of thermography as promising non-invasive detection modality for breast tumor," *Int J Therm Sci* 48(5), 849-859 (2009)

14. C. Hildebrandt, C. Raschner and K. Ammer, "An overview of recent application of medical infrared thermography in sports medicine in Austria," *Sensors* 10(5), 4700-4715 (2010)

15. P. Patel, A. Luk, A. Durrani, S. Dromi, J. Cuesta, M. Angstadt, M. Dreher, B. Wood and V. Frenkel, "In vitro and in vivo evaluations of increased effective beam width for heat deposition using a split focus high intensity ultrasound (HIFU) transducer," *Int J Hyperthermia* 24(7), 537-549 (2008)

16. S. Bobkova, L. Gavrilov, V. Khokhlova, A. Shaw and J. Hand, "Focusing of high-intensity ultrasound through the rib cage using a therapeutic random phased array," *Ultrasound Med Biol* 36(6), 888-906 (2010)

17. J. W. Hand, A. Shaw, N. Sadhoo, S. Rajagopal, R. J. Dickinson and L. R. Gavrilov, "A random phased array device for delivery of high intensity focused ultrasound," *Phys Med Biol* 54(19), 5675-5693 (2009)

18. A. Shaw and J. Nunn, "The feasibility of an infrared system for real-time visualization and mapping of ultrasound fields," *Phys Med Biol* 55(11), N321-N327 (2010)

19. M. R. Myers and D. Giridhar, "Theoretical framework for quantitatively estimating ultrasound beam intensities using infrared thermography," *J Acoust Soc Am* 129(6), 4073-4083 (2011)

20. C. Song, B. Marshall, D. McLean, T. G. Frank, W. Sibbett, A. Cuschieri and P. A. Campbell, "Thermographic investigation of the heating effect of high intensity focused ultrasound," in *Proc 27th Annual Intl Conf IEEE Engin Med Biol Soc*, 3456-3458, IEEE (2005)

21. Z. Qiu, J. Gao, S. Cochran, Z. H. Huang, G. Corner and C. L. Song, "The development of therapeutic ultrasound with assistance of robotic manipulator," in *Proc 35th Annual Intl Conf IEEE Engin Med Biol Soc*, 733-736, IEEE (2009)

22. F. A. Duck, *Physical Properties of Tissue*, Academic Press Inc., San Diego, CA (1990)

23. J. C. Bamber, "Speed of sound," in *Physical principles of medical ultrasonics*, C. R. Hill, J. C. Bamber and G. R. ter Haar, Eds., 167-190, John Wiley & Sons, Ltd, Chicester, West Sussex, England (2004)

24. E. L. Madsen, J. A. Zagzebski, R. A. Banjavie and R. E. Jutila, "Tissue mimicking materials for ultrasound phantoms," *Med Phys* 5(5), 391-394 (1978)

25. E. L. Madsen, J. A. Zagzebski and G. R. Frank, "Oil-in-gelatin dispersions for use as ultrasonically tissue-mimicking materials," *Ultrasound Med Biol* 8(3), 277-287 (1982)

26. T. L. Bergman, A. S. Lavine, D. P. Dewitt, and F. P. Incropera, "Radiation: processes and properties," in *Introduction to heat transfer*, 733-826, John Wiley & Sons, Inc., Hoboken, NJ (2011)

27. R. P. Madding, "Emissivity measurement using infrared imaging radiometric cameras," in *Encyclopedia of optical engineering*, R. G. Driggers, Ed., 475-483, CRC Press, New York, NY (2003)

28. R. Seip, P. VanBaren, C. A. Cain and E. S. Ebbini, "Noninvasive real-time multipoint temperature control for ultrasound phased array treatments," *IEEE Trans Ultrason Ferroelectr Freq Control* 43(6), 1063-1073 (1996)

29. R. M. Arthur, W. L. Straube, J. W. Trobaugh and E. G. Moros, "Non-invasive estimation of hyperthermia temperatures with ultrasound," *Int J Hyperthermia* 21(6), 589-600 (2005)

30. V. Rieke and K. Butts Pauly, "MR thermometry," *J Magn Reson Imaging* 27(2), 376-390 (2008)

31. G. L. Ye, P. P. Smith and J. A. Noble, "Model-based ultrasound temperature visualization during and following HIFU Exposure," *Ultrasound Med Biol* 36(2), 234-249 (2010)

32. A. Anand, D. Savery and C. Hall, "Three-dimensional spatial and temporal temperature imaging in gel phantoms using backscattered ultrasound," *IEEE Trans Ultrason Ferroelectr Freq Control* 54(1), 23-31 (2007)

33. D. Liu and E. S. Ebbini, "Real-time 2-D temperature imaging using ultrasound," *IEEE Trans Biomed Eng* 57(1), 12-16 (2010)

34. C. Öhman, "Measurement in thermography," 22-35, FLIR Systems AB (2001)

CHAPTER 3

Characterization of lesion formation and bubble activities during high-intensity focused ultrasound ablation using temperature-derived parameters

In chapter 2 we introduced a new platform to evaluate ultrasound thermometry. However, ultrasound thermometry is known to have a limited working temperature range up to 50 °C due to the small changes in acoustic properties (e.g., speed of sound) at temperatures > 50 °C. Therefore for high-intensity focused ultrasound (HIFU) ablation monitoring, an alternative imaging method is needed. It is also critical to establish a better understanding of the temperature distribution during HIFU heating as well as the temperature characteristics relevant to HIFU events such as tissue coagulation and bubble activities. Therefore in this chapter, we developed a system using infrared (IR) thermography and bright-field imaging to measure tissue surface temperature during the course of HIFU application and to correlate HIFU events with several temperature-derived parameters. The threshold for tissue thermal damage based on temperature time history was also experimentally determined for porcine cardiac tissue. Although IR thermography is limited to monitoring HIFU ablation when the focus is placed near an accessible tissue surface, the identified relations between temperature changes and HIFU events are applicable in general.

The work in this chapter has been published in Infrared Physics & Technology 60, 108-117 (2013) entitled "Characterization of lesion formation and bubble activities during high-intensity focused ultrasound ablation using temperature-derived parameters".

3.1 Introduction

During HIFU heating, the tissue temperature evolves as a function of time and spatial location as described by the bioheat equation[1-3]

$$\frac{\partial T}{\partial t} = \nabla \cdot \kappa \nabla T - \frac{T}{\tau} + Q_m + Q_{ex}, \tag{3.1}$$

where T is the temperature (^{o}C), t is the time (s), κ is the thermal diffusivity (m^2/s), and τ is the perfusion time constant (s). Q_m is the metabolic heat generation (^{o}C/s) and Q_{ex} is the external heat source (^{o}C/s) provided by HIFU, which is expressed as

$$Q_{ex} = \frac{2\alpha_{ab} f}{c_v} \cdot I_0 e^{-2f \cdot \int_{path} \alpha_{atten}(z) dz} \tag{3.2}$$

where α_{ab} and α_{atten} are the absorption and attenuation coefficient (neper/MHz-cm), f is the ultrasound frequency (MHz), c_v is the volume specific heat (J/cm^3·K), and I_0 is the ultrasound free-field intensity (W/cm^2). The ultrasound intensity at a given spatial location is its free-field intensity attenuated by the exponential term where the effect of attenuation is integrated along the beam propagating path.

Temperature monitoring during HIFU ablation is important because tissue necrosis or lesion formation depends on the thermal dose[4-6] which is determined by the cumulative effect of heat deposited in the tissue. Given the threshold of tissue damage as evaluated by the critical cumulative equivalent minutes at 43 °C (CEM_{43}) for a specific tissue type, the evolution of lesion extent can be predicted.[7,8] Typically, a critical CEM_{43} of 240 min has been

used extensively to predict tissue coagulation in kidney, liver, and muscle,[9,10] although it actually varies across species as well as tissue types.[11] The true threshold is often difficult to obtain due to the difficulty in determining the temporal temperature profile during lesion formation. Also, prediction errors may arise when the value used was obtained from experiments with a much different temperature range or heating mechanism (e.g., heating rate, intensity).[12]

During HIFU application, lesion formation results in changes of the thermal, mechanical, and acoustic properties of the tissue. These changes, along with other events induced by HIFU heating, can alter the course of temperature evolution. In particular, degassing, boiling, vaporization, and cavitation in tissue[13,14] often occur due to excessive heating, rapid temperature increase, and high level of acoustic pressures. In some cases, the combined effect of high acoustic pressure and rapid heating may generate unwanted macroscopic cavities or tissue fragmentation. These events, which result in destruction of local tissue integrity and changes of material properties, not only cause inefficient ablation of distal tissue segments[15] and altered lesion location, shape, and size from the original treatment plan, but also render the prediction of tissue status from temperature measurement difficult.

Given the above concerns, it is therefore necessary to provide a system to measure the spatiotemporal temperature distribution during HIFU application and determine temperature characteristics relevant to HIFU events such as tissue coagulation and bubble activities. It is also important to build a system capable of measuring the critical CEM_{43} for any tissue type of interest.

As demonstrated in Chapter 2, IR thermography has its advantage in easy implementation and capability of non-contact, real-time monitoring of surface temperature with high temporal and spatial resolution. Laparoscopic IR systems have also been developed and used in assessing tissue necrosis during radiofrequency ablation[16] and tested on porcine models to provide additional anatomic and physical details from the differences in temperature between adjacent structures and organs.[17,18] However, IR thermography has only been used in a few HIFU-related studies, in which the two dimensional (2D) spatiotemporal IR images of temperature were not fully exploited.

Therefore in this chapter, we employed IR thermal imaging with synchronized bright-field imaging to measure temperature during HIFU exposures and determined useful temperature-derived markers indicative of HIFU events. Experiments were conducted using *ex-vivo* cardiac tissue, for the purpose of ultimately improving HIFU ablation of cardiac arrhythmia.[19,20] We used IR imaging to measure tissue surface temperature during HIFU ablation. We first conducted experiments with the HIFU focus placed close to and slightly below the tissue surface where lesion formation and other events can be observed on the surface. In this way, changes in temperature-derived parameters related to lesion formation, overheating and bubble formation during HIFU application could be identified to permit corroboration of tissue changes with temperature measurements by IR imaging. This registered observation also allows computation of the thermal dose and determination of the critical CEM_{43} for myocardium tissue. We then extended our experimental studies to subsurface HIFU ablation to identify the characteristic temperature behaviors in this context. Finally, we investigated the potential of using lower intensity, non-ablative focused ultrasound (FUS) exposures in conjunction with IR imaging to detect the presence of lesion.

3.2 Materials and methods

3.2.1 Tissue specimens and emissivity measurement

Ex-vivo porcine myocardium tissue specimens obtained from a local abattoir were used in this study. We used the same IR camera (Silver 5600, FLIR Systems, Boston, MA, USA) described in Sec. 2.2.2. To measure the emissivity ε for myocardium, a flat surface of the tissue specimen was imaged with the IR camera perpendicular to the surface. Emissivity was measured using the black tape method[21] where the Scotch Super 33+ Vinyl Electrical Tape (3M Company, St. Paul, MN, USA) with a known emissivity of 0.95 was used. The emissivity of coagulated myocardium was also measured after coagulation in a microwave oven, where different levels of dehydration were generated by applying various durations of microwave exposure.

3.2.2 Experimental setup and IR imaging

The schematic of the IR-HIFU system is shown in Fig. 3.1. IR imaging was performed using two integration (exposure) times for measurements ranging from 15 °C to 120 °C, and conversion from IR radiance to temperature was performed using the manufacturer's calibration and non-uniformity corrections.

To generate HIFU exposures with adjustable amplitude and duration, the HIFU system used two function generators (33220A, Agilent, Santa Clara, CA, USA), a power amplifier (325LA, ENI, Rochester, NY, USA), and a focused transducer (3.98 MHz center frequency, F = 1, Blatek, Inc., State College, PA, USA). The HIFU transducer was calibrated using a hydrophone (HNR-0500, Onda, Sunnyvale, CA, USA) and its − 6 dB focal width and focal length were measured as 0.9 mm and 4.6 mm, respectively. Experiments were performed with the transducer submerged in water facing up towards a tissue specimen with

its top surface above the water level to allow IR temperature measurements at a 50 Hz frame rate. (The tissue needed to be submerged on the underside to allow HIFU propagation in the specimen.) A plastic holder with an acoustically transparent bottom (Tegaderm, 3M, St. Paul, MN, USA) was used to hold the specimen and to prevent water from permeating into the tissue during HIFU exposures.

The IR camera was positioned perpendicular to the tissue surface, while an angled video camera at 24 Hz frame rate (D5000, Nikon, Melville, NY, USA) was used for bright-field imaging to monitor the tissue surface and identify lesion, cavity formation, and water extraction or tissue dehydration due to HIFU application. An indented ruler visible in both bright-field and IR images was placed on the edges of the tissue specimen for alignment. HIFU exposures and IR imaging acquisition were synchronized by a data acquisition system (OMB-DAQ-3000, Omega Engineering, Stamford, CT, USA). Bright-field imaging was synchronized by capturing a green LED light signal which turned on when IR imaging started. All image analysis and computations were performed using MATLAB (R2010a, Mathworks, Natick, MA, USA) offline.

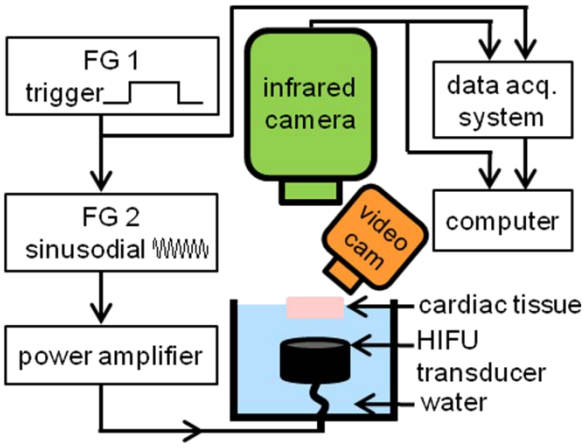

Figure 3.1 Schematic diagram of the experimental setup for IR thermography with HIFU heating.

3.2.3 HIFU ablation

Ablation was conducted using continuous wave HIFU exposures (1060 and 1500 W/cm^2 focal intensity) with various exposure durations. To only induce temperature increase within the tissue without generating tissue coagulation as a control, non-ablative (125 and 283 W/cm^2) continuous wave HIFU exposures were used. The HIFU parameters were chosen based on previous experiments to ensure the desired outcome (i.e., with or without generating lesion). IR imaging and bright-field imaging were performed before, during, and after HIFU application. Gross images of the tissue cross-section were taken after HIFU application and outcomes were classified into three categories: (1) non-ablative: no lesion was formed, (2) normal lesion: lesion formed without signs of cavitation or excessive heating, and (3) overheated lesion: lesion with cavity and/or discoloration within the lesion core that may be associated with changes beyond coagulation, such as dehydration and/or charring/carbonization. Only cases which could be clearly classified were included in this study.

3.2.4 Bright-field imaging

To determine the evolution of the lesion on the tissue surface, bright-field images were analyzed by first converting the true color RGB images into grayscale images using the rgb2gray.m function in MATLAB. After image conversion, a converted pre-HIFU reference frame was subtracted from all frames in the video sequence to generate “processed bright-field images.”

To ensure that tissue discoloration is an indication of coagulation, in our preliminary experiments, we stained tissue specimens with HIFU lesions using Masson's Trichrome and the lesion boundaries matched well between the bright-field image and histology (Fig. 3.2). However, histology stain was not used in this study to correlate with temperature-derived parameters due to its limitation to post-treatment assessment and distortion of tissue geometry during sectioning.

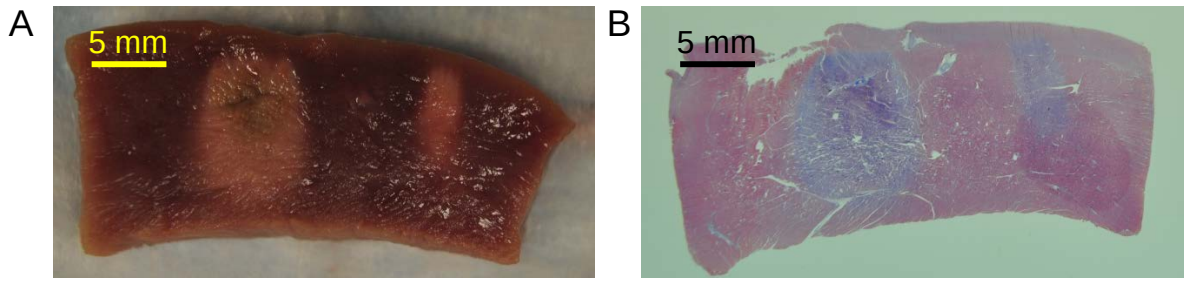

Figure 3.2 (A) Gross image and (B) corresponding histology with Masson's trichrome stain on porcine cardiac tissue with two regions of HIFU-induced thermal lesions.

3.2.5 Time derivatives of temperature change

To characterize lesion and bubble formation, the first and second order time derivatives of temperature were calculated from the experimental data using

$$\frac{\partial T}{\partial t}(x,y,t) \approx \frac{T(x,y,t+\Delta t)-T(x,y,t-\Delta t)}{2\Delta t}, \tag{3.3}$$

$$\frac{\partial^2 T}{\partial t^2}(x,y,t) \approx \left[\frac{\partial T}{\partial t}(x,y,t+\Delta t)-\frac{\partial T}{\partial t}(x,y,t-\Delta t)\right] \Big/ 2\Delta t, \tag{3.4}$$

where Δt is the duration between IR frames. A second order low-pass Butterworth filter with −3dB cutoff frequency of 2.5 Hz was applied to the temporal temperature data prior to taking the first derivative, and another one with −3dB cutoff frequency of 5 Hz was applied to the

first time derivative before taking the second time derivative. Because the initial rate of temperature change during HIFU is directly proportional to HIFU intensity,[22] the normalized derivative

$$\dot{\theta}(x,y,t) = \frac{\partial T / \partial t(x,y,t)}{\partial T / \partial t(x,y,t=0)} \tag{3.5}$$

was also computed to better allow for comparison between different exposure intensities and different spatial locations. Its corresponding normalized second derivative was computed from Eq. (3.5) by

$$\ddot{\theta}(x,y,t) \approx \frac{\dot{\theta}(x,y,t+\Delta t) - \dot{\theta}(x,y,t-\Delta t)}{2\Delta t}. \tag{3.6}$$

3.2.6 Thermal damage

The temperature data were used to evaluate the thermal damage based on CEM_{43} using[4]

$$CEM_{43} = \sum_{t=0}^{t_f} R^{(43-\bar{T})} \Delta t, \tag{3.7}$$

where $\bar{T}$ is the average temperature during time Δt, t_f is the final time, $R = 0.25$ below 43 °C, and $R = 0.5$ above 43 °C. To determine the critical CEM_{43} for myocardium, one sequence of IR images and bright-field images where lesion formation was observed at the surface during HIFU ablation (1060 W/cm^2, 10 s, focused at 3 mm beneath surface) was analyzed. For the purposes of computing CEM_{43}, the lesion must be formed only by thermal effects. As such, experimental data were selected to have no observable generation of bubbles or cavities on the tissue surface.

The processed bright-field images were first resized to have the same resolution as the IR images using bicubic interpolation (imresize.m function in MATLAB). Then the lesion boundaries were manually segmented on the processed bright-field images based on the gray-scale intensities at five different time points (t = 6, 7, 8, 9, 10 s) when the surface lesion grew large enough to have distinguishable lesion boundaries. The true lesion binary masks were formed with the areas inside the boundaries identified as lesions and outside as non-lesions. The CEM_{43} images at the corresponding time frames were computed using Eq. (3.7).

3.2.7 Receiver-operating characteristic (ROC) curves

To determine the thresholds for lesion and bubble formation based on the data derived from the temperature measurements (e.g., $\ddot{\theta}$) and the critical CEM_{43} for lesion formation, classifications based on ROC curves[23] were used.

For any given CEM_{43} image, a time threshold τ can be applied to classify each pixel as lesion ($CEM_{43} > \tau$) or non-lesion ($CEM_{43} < \tau$) and thereby form a "predicted lesion" binary matrix at each τ. By comparing the "predicted lesion" binary matrix with the "true lesion" binary mask from the processed bright-field images, the number of pixels that were true positive (*TP*), false positive (*FP*), true negative (*TN*), and false negative (*FN*) were calculated at each τ. (A pixel was considered to be *TP* if it was predicted to be lesion and actually was lesion, *FP* if it was predicted to be lesion but was not lesion, *TN* if it was predicted not to be lesion and was not lesion, and *FN* if it was predicted not to be lesion and was lesion.) An overall empirical ROC curve can be drawn by plotting the true positive fraction ($TPF = TP_{\text{total}} / P_{\text{total}}$) versus the false positive fraction ($FPF = FP_{\text{total}} / N_{\text{total}}$) where the

number of pixels were summed from the five frames, i.e., $TP_{total} = \sum_{i=1}^{5} TP_i$. The area under curve (AUC) was computed to evaluate the performance of the classifier τ. The accuracy at each threshold is calculated as (TP_{total} + TN_{total}) / (P_{total} + N_{total}), and the critical CEM_{43} was determined by finding the τ value which resulted in the maximum accuracy. The thresholds for lesion and bubble formation based on the data derived from temperature measurements were determined following a similar procedure. Due to the imbalanced number of datasets for ablative and non-ablative experiments, the non-ablative datasets were over-sampled using the synthetic minority over-sampling technique (SMOTE[24]) prior to performing ROC analysis in the determination of the lesion formation threshold.

3.2.8 Thermal probing: non-ablative FUS heating on HIFU lesions

To investigate the spatiotemporal temperature distribution affected by the presence of HIFU lesions, in addition to the experiments where surface temperature was measured during the HIFU ablation, two sets of experiments were performed with FUS exposures applied on tissues with pre-generated subsurface HIFU lesions (*ex-vivo* porcine myocardium Specimen 1 and 2). We refer the process of applying the lower intensity, non-ablative FUS exposures to characterize tissue properties as “thermal probing”. In these experiments, FUS exposures (125 W/cm^2, 100% DC, 5 s) were applied with the focus placed at 3 mm beneath the tissue surface to induce temperature increase without generating tissue changes. FUS probing exposure was applied before any lesion generation in the tissue as a control. Multiple ablative FUS exposures (1500 W/cm^2) were applied to generate lesion in the subsurface volume in each tissue specimen, with the lesion in Specimen 2 purposely generated to be larger than the lesion in Specimen 1. Post-lesion thermal probing exposure with the same

intensity and duration as the control was then applied to induce temperature increase without generating additional tissue coagulation. IR images before and after lesion formation were compared using the temperature rise, computed using $\Delta T(x, y, t) = T(x, y, t) - \check{T}(x, y, t < 0)$, where $T(x, y, t)$ is the measured surface temperature at a given spatial location (x, y) at time t and $\check{T}(x, y, t < 0)$ is the temporal average temperature from 0 to 2 seconds prior to FUS application. The pre-lesion temperature rise images were subtracted from the post-lesion images in order to detect the changes in tissue properties to reveal the presence of HIFU lesion.

3.3 Results and discussion

3.3.1 Emissivity of porcine myocardium tissue

The emissivity of porcine myocardium tissue specimens used in our study was measured to be 0.857 ± 0.006 ($n = 3$), in agreement with the reported epicardium emissivity ($0.84 - 0.89$) measured using a monochromator.[25] The emissivity of microwaved myocardium was measured to be $0.82 - 0.84$, with the lower value corresponding to the more dehydrated specimens. These results are consistent with a previous study where dehydration in skin leads to decreased emissivity.[26] In this study, emissivity was set to 0.86 for IR imaging of all experiments.

3.3.2 Characteristic features of spatiotemporal evolution of temperature during HIFU ablation

In these experiments (total $n = 28$), the HIFU focus was placed slightly below the tissue surface (0 – 3 mm) such that lesions induced by HIFU readily extended to the surface and were observable by bright-field imaging. Figure 3.3 shows a typical example of synchronized IR images (Fig. 3.3A) and bright-field images (Fig. 3.3B) of the tissue surface during an ablative HIFU exposure (1060 W/cm^2, 20 s). Temperatures as a function of time at different locations are shown in Fig. 3.3C.

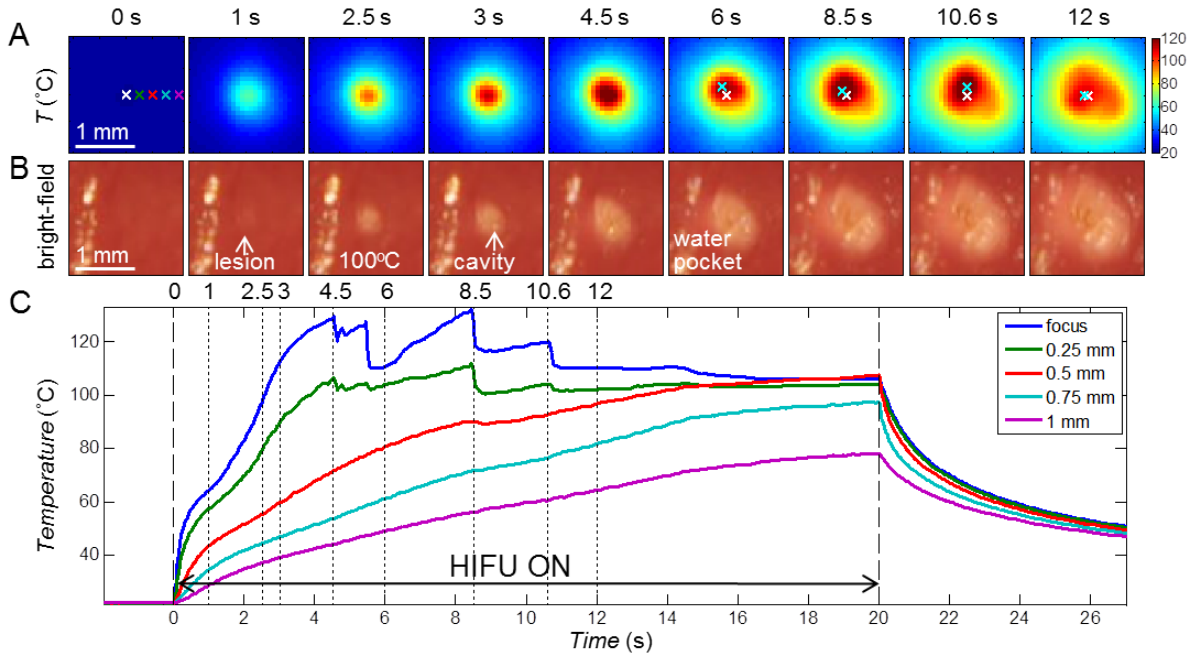

Figure 3.3 IR measurement of temperature with ablative HIFU exposure (1060 W/cm^2, 20 s) with focus placed at the surface. (A) IR images showing the surface temperature T (°C). The spatial peak temperature (cyan cross) is indicated in the images after t = 6 s, deviating from the original center focus (white cross). (B) Bright-field images of the tissue surface showing lesion and cavity formation. The bright stripe on the left of each image is due to the presence of some water. (C) Time evolution of T at the focus, 0.25, 0.5, 0.75, and 1 mm to the right of the focus (indicated on the first IR image in (A)).

Several characteristics were identified in the spatiotemporal evolution of the surface temperature during HIFU ablation. First, at and near the HIFU focal location, the temperatures increased rapidly initially (< 0.5 s after HIFU application at $t = 0$ s), while the rate of temperature increase (slope or $\partial T/\partial t$) quickly dropped from the maximum value, as expected from prediction of linear bioheat equation with a constant heat source. However, at about $t = 0.8 - 1$ s, the temperature slope increased again, indicating faster rise of temperature. This sudden enhanced increase of temperature corresponded to lesion formation as identified by the bright-field images (Fig. 3.3B). Second, as heating continued, a small cavity formed near the focus ($t = 3$ s) and the temperature (Fig. 3.3C) correspondingly showed irregular variations. Third, a small pocket of water came out of the tissue and accumulated near the lesion/cavity area ($t = 6$ s), accompanied by a flattening of the temperature profile, deviating from the expected increase of temperature predicted by the bioheat equation.[1-3] The temperature stayed almost constant near 100 °C until the end of the HIFU ($t = 20$ s), after which the temperature decreased. Temperatures at locations farther away from the focus without lesion formation increased during HIFU exposure and decreased smoothly after HIFU exposure as expected.

Temperature changes during HIFU lesion formation. Correlation of lesion formation with the sudden increase in $\partial T/\partial t$ shown in Fig. 3.3 is further illustrated by a closer examination of the temperature change in the first 2.4 s (Figs. 3.4A – C and 3.5A – C). In particular, the time point of the reversal of $\partial T/\partial t$ (Fig. 3.5B, solid arrow) can be easily identified by the zero-crossing of $\partial^2 T/\partial t^2$ (Fig. 3.5C, solid arrow). In contrast, in a tissue exposed to HIFU intensity of 283 W/cm^2 (5 s duration) without lesion generation (Figs. 3.4D, 3.4E, 3.5D – F), $\partial T/\partial t$ continued to decrease from its initial maximum in the

course of temperature evolution (Fig. 3.5E) without zero-crossing (Fig. 3.5F). The zero-crossing of $\partial^2 T/\partial t^2$ was observed to correspond to surface lesion formation in most experiments. To compare between exposures of different intensities (in different experiments and at different spatial locations) based on these observations, we developed a criterion for lesion identification from the maximum value of the normalized second time derivative

$$\ddot{\theta}_{\max} = \max\left[\ddot{\theta}(x, y, t)\right] \text{ over } t^* < t < t_{end} \tag{3.8}$$

where t^* is the time of minimum $\ddot{\theta}$ (e.g., as indicated by the dotted arrows in Figs. 3.5C and 3.5F) at the start of HIFU exposure (0 − 1 s) at each (x, y) location within 0.3 mm (smaller than half the focal width) from the HIFU focus, and t_{end} is the end time of HIFU exposure. To avoid errors from noise when taking derivatives from small temperature changes, only $\ddot{\theta}$ with $\partial T/\partial t > 2$ °C/s were considered. Figure 3.6 shows the histogram of $\ddot{\theta}_{\max}$ for all ablative (including HIFU outcomes of normal and overheated lesions, $n = 22$, 549 locations, where each location is represented by one pixel in the IR images) and non-ablative ($n = 6$, 222 locations) experiments. This classifier was determined to have an ROC AUC of 0.999 and with a threshold of $\ddot{\theta}_{\max} = 0.05\ \text{s}^{-1}$ providing 99.1 % accuracy for lesion identification. The threshold is close to zero as expected, corresponding to an occurrence of zero-crossing when lesion forms.

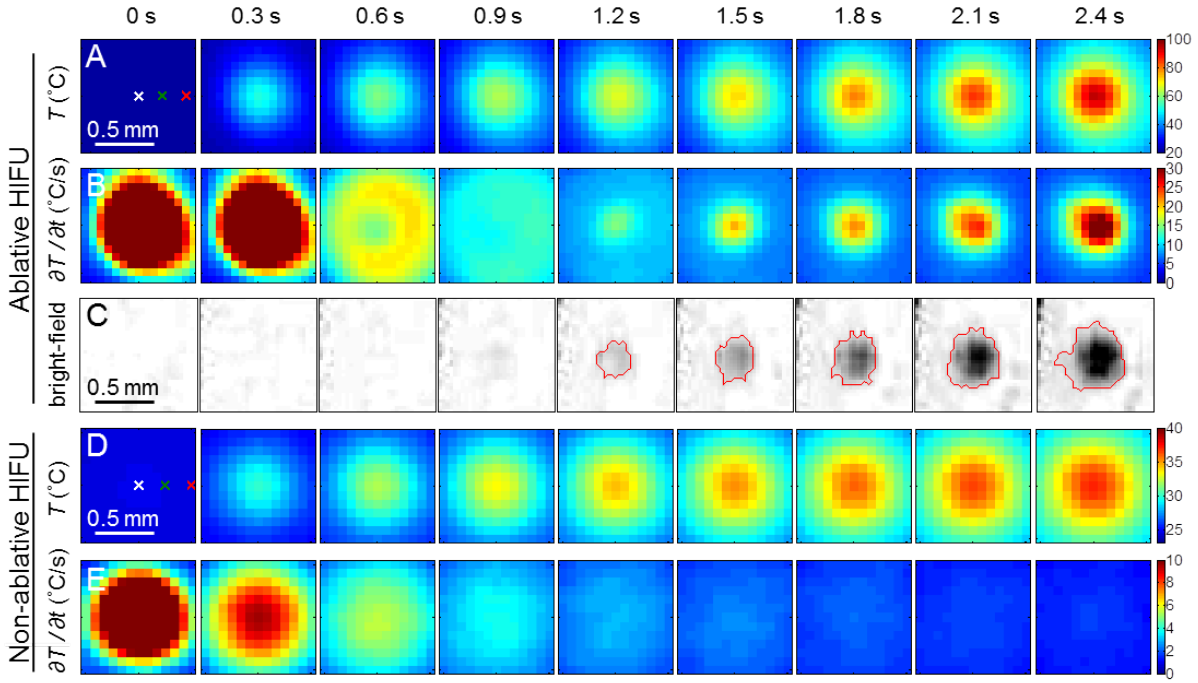

Figure 3.4 (A – C) Ablative HIFU exposure with focus placed at the surface: Zoomed-in images of the first 2.4 s in Fig. 3.3 showing (A) IR images of the surface temperature T (°C), (B) images of the rate of temperature change $\partial T/\partial t$ (°C/s), and (C) processed bright-field images of the tissue surface showing lesion formation. The red line indicates the lesion boundary. (D – E) Non-ablative HIFU exposure with focus placed at the surface: The first 2.4 s during a non-ablative HIFU exposure (283 W/cm^2, 5 s duration) showing (D) IR images of T (°C) and (E) images of $\partial T/\partial t$ (°C/s).

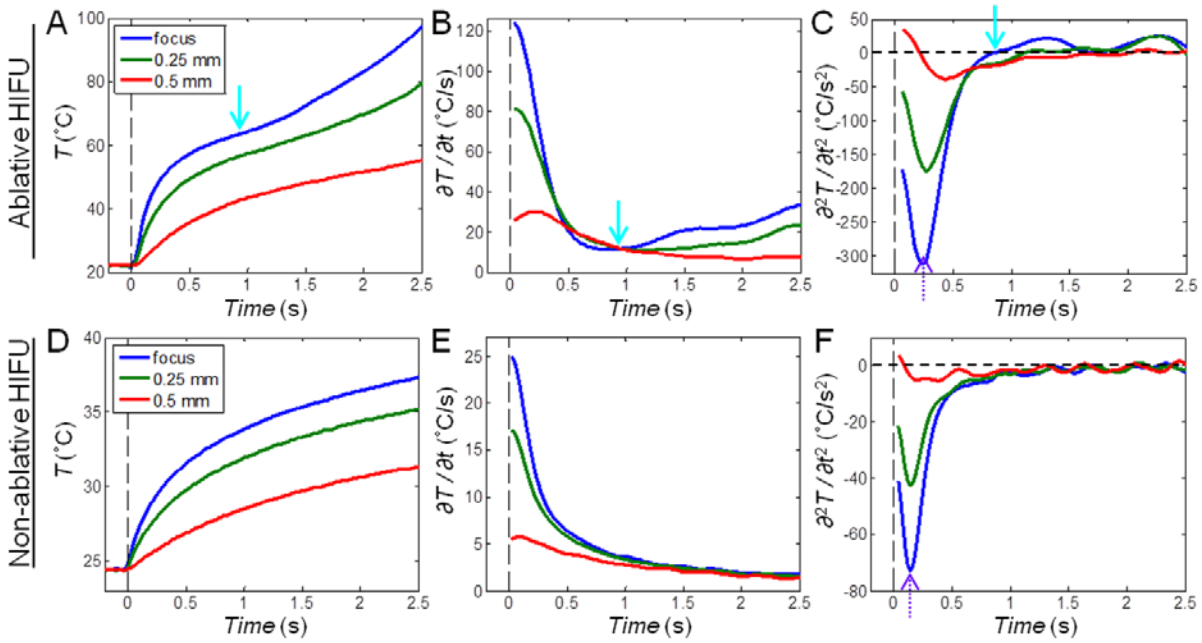

Figure 3.5 Time evolution of temperature T (°C), the rate of temperature change $\partial T/\partial t$ (°C/s), and the second derivative of temperature change $\partial^2 T/\partial t^2$ (°C/s^2) corresponding to Fig. 3.4. The points at the focus and 0.25 mm and 0.5 mm to the right of the focus are shown (indicated on the first IR image in Figs. 3.4A and 3.4D. (A – C) Ablative HIFU exposure: Extra heating is indicated by the solid cyan arrows at 0.8 − 1 s when lesion starts to form. (D – F) Non-ablative HIFU exposure: $\partial T/\partial t$ continues to decrease without any reversal. The dotted purple arrows indicate the time point when $\partial^2 T/\partial t^2$ reaches its minimum value.

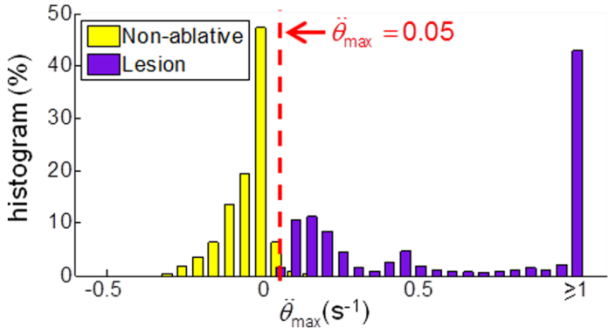

Figure 3.6 Determination of the criterion for surface lesion formation: Histogram of the maximum normalized second derivative of temperature change $\ddot{\theta}_{max}$ for non-ablative and ablative HIFU ablations. The dashed line indicates a threshold of $\ddot{\theta}_{max} = 0.05$ s^{-1} which provided the highest accuracy for lesion identification.

The increase in $\partial T/\partial t$, or the zero-crossing of $\ddot{\theta}_{max}$, can be explained by the increase in acoustic attenuation coefficient in the coagulated tissue compared to normal tissue,[27,28] resulting in enhanced absorption of ultrasound energy and HIFU heating. The faster rate of temperature increase will be even more significant if the temperature was corrected to account for the changes in emissivity due to lesion formation (see Sec. 3.3.1). This increase in heating rate has been observed in previous studies using thermocouples.[29] As the attenuation and absorption are affected by temperature and thermal dose CEM_{43},[30] the increase in the heating rate is most significant when a high thermal dose is deposited in a short period of time.

Overheating: cavity formation and water extraction. During HIFU exposures (intensity > 1000 W/cm^2), small cavities often appeared after lesion formation, as shown by the bright-field images (e.g., Fig. 3.3B, t = 3 s). As a result, the temperature near the focus became unsteady (Fig. 3.3C, t > 3 s), due to the loss of tissue integrity. Eventually, the spatial temperature distribution around the lesion became irregular and asymmetric (Fig. 3.3A, t > 6 s), accompanied by the appearance of water near the lesion/cavity area which seemed to be released/extracted from tissue bulk itself (the tissue specimen was water-sealed from below).

Cavity formation can be attributed to thermally-mediated gas pockets and cavitation associated with high acoustic pressures. In most cases with apparent cavity formation, an asymmetric temperature distribution was observed. To describe the asymmetric temperature distribution, we denoted the displacement of the spatial location of the peak temperature (e.g., Fig. 3.3A, cyan cross) from the initial center (e.g., Fig. 3.3A, white cross) at time t as $d(t)$. Figure 3.7 shows a box plot of the maximum displacement d_{max} during the entire time course

of the HIFU exposure, where $d_{max} = \max[d(t)]$ over $t = 0 < t < t_{end}$. Using the unequal variance t-test (Behrens-Fisher problem), d_{max} for ablative HIFU exposures with overheating and/or cavity formation (mean ± S.D. = 0.315 ± 0.113 mm, $n = 15$) was significantly different from cases of non-ablative (0.075 ± 0.039 mm, $n = 6$, $p < 0.001$) and normal ablative HIFU exposures (without overheating) (0.143 ± 0.130 mm, $n = 7$, $p = 0.01$). No significant difference existed between the cases of non-ablative and normal ablative HIFU exposures ($p = 0.22$). The threshold to distinguish between overheated and normal lesions is 0.16 mm providing 90.9 % accuracy with an ROC AUC of 0.86. Therefore d_{max} can be used to identify excessive heating during HIFU applications.

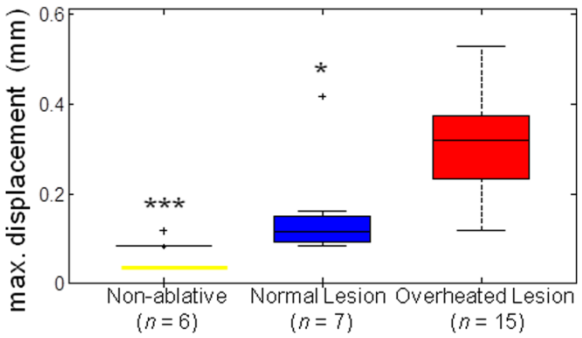

Figure 3.7 Determination of criterion for overheated surface lesions: Maximum displacement of spatial peak temperature location d_{max} from surface HIFU ablation experiments for non-ablative, normal lesion, and overheated lesion cases. The level of statistical significance compared with the overheated lesion cases is represented by triple asterisk (***) if $p < 0.001$and single asterisk (*) if $p < 0.05$. A threshold of 0.16 mm provides the highest accuracy to differentiate between normal and overheated surface lesions.

Thermal damage threshold. The lesion regions, determined from the bright-field images, were used to find the thermal damage threshold for the myocardium tissue specimens. The true lesion boundary was determined manually on each of the processed bright-field image, as shown by the example in Fig. 3.8A (t = 9 s in the HIFU experiment: 1060 W/cm^2, 10 s, focused at 3 mm beneath surface). The corresponding CEM_{43} image (Fig. 3.8B) was thresholded by a set of times τ ranging from 0 to 5×10^3 min. The overall ROC curve (Fig. 3.8C) was calculated from the average of *TP*, *TN*, *FP*, and *FN* from the five frames (t = 6, 7, 8, 9, 10 s, each with a different lesion size), and the AUC was 0.99. From the overall accuracy curve (Fig. 3.8D), the optimal critical CEM_{43} for lesion formation is 170 min. The predicted lesion boundary using CEM_{43} = 170 min is indicated on the processed bright-field image and the CEM_{43} image (Figs. 3.8A and 3.8B), within the normal range of soft tissues (40–240 min[11]).

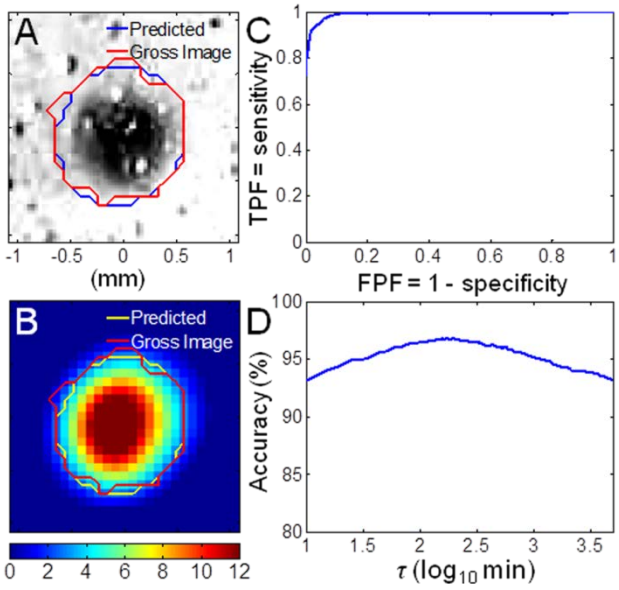

Figure 3.8 Determination of the critical CEM_{43}: (A) Processed bright-field image (t = 9 s) with lesion at the center, mapped with true lesion boundary (red) and the predicted lesion boundary using critical CEM_{43} = 170 min (blue). (B) Corresponding parametric image of CEM_{43} on a logarithmic scale. (C) Overall empirical receiver-operating characteristic (ROC) curve with area under the curve (AUC) = 0.99. (D) Overall accuracy as a function of threshold τ. The maximum accuracy occurs at 170 min.

The critical CEM_{43} for cardiac tissue has been estimated to be 128 min[5] but has not been experimentally determined. In this study, by deliberately forming the lesion on the tissue surface and evaluating the spatiotemporal temperature increase with confirmed lesion formation, the threshold of tissue coagulation was readily determined experimentally. Although *ex-vivo* samples lack perfusion and tissue viability which could affect how the thermal damage can be assessed,[11] the use of IR imaging to determine the thermal damage threshold can be easily carried out in both *ex-vivo* and *in-vivo* studies on various different tissue types and specimens.

3.3.3 Spatiotemporal temperature changes for subsurface HIFU ablation

In these experiments (total $n = 39$), the focus of the HIFU transducer was placed 3 – 8 mm beneath the tissue surface. The spatiotemporal temperature measured on the surface was correlated with HIFU events occurring at the subsurface volume based on characteristics observed from the experiments with lesion formation on the surface (Sec. 3.3.2).

Temperature changes during HIFU lesion formation. Figure 3.9 shows an example of the IR images (Fig. 3.9A), $\partial T/\partial t$ images (Fig. 3.9B), and the corresponding bright-field images of the surface (Fig. 3.9C) from an ablation experiment (1060 W/cm^2, 10 s) with the focus placed at 3 mm beneath the surface. As in the case of surface ablation, the temperature at the surface above the HIFU focus increased rapidly after the start of HIFU application. The value of $\partial T/\partial t$ was the highest at the start of the HIFU exposure and then decreased. A reversal of $\partial T/\partial t$ which corresponded to the zero-crossing of $\partial^2 T/\partial t^2$ occurred at 2 s (Figs. 3.9B and 3.9E, Marker [1]), suggesting subsurface lesion formation based on the similar characteristics as those of surface lesion formation (e.g., Figs. 3.4B and 3.5B, starting

t = 1 s) despite no visible surface lesion and CEM_{43} of 0.42 min at the center point (Fig. 3.9F, Marker [1]). $\partial T/\partial t$ continued to increase after 2 s, and lesion appeared on the surface at 3.5 to 4 s (Fig. 3.9C), when the CEM_{43} was from 111 to 802 min. The CEM_{43} reached 170 min at 3.62 s (Fig. 3.9F, Marker [2]). The gross image of the lesion cross-section is shown in Fig. 3.9G.

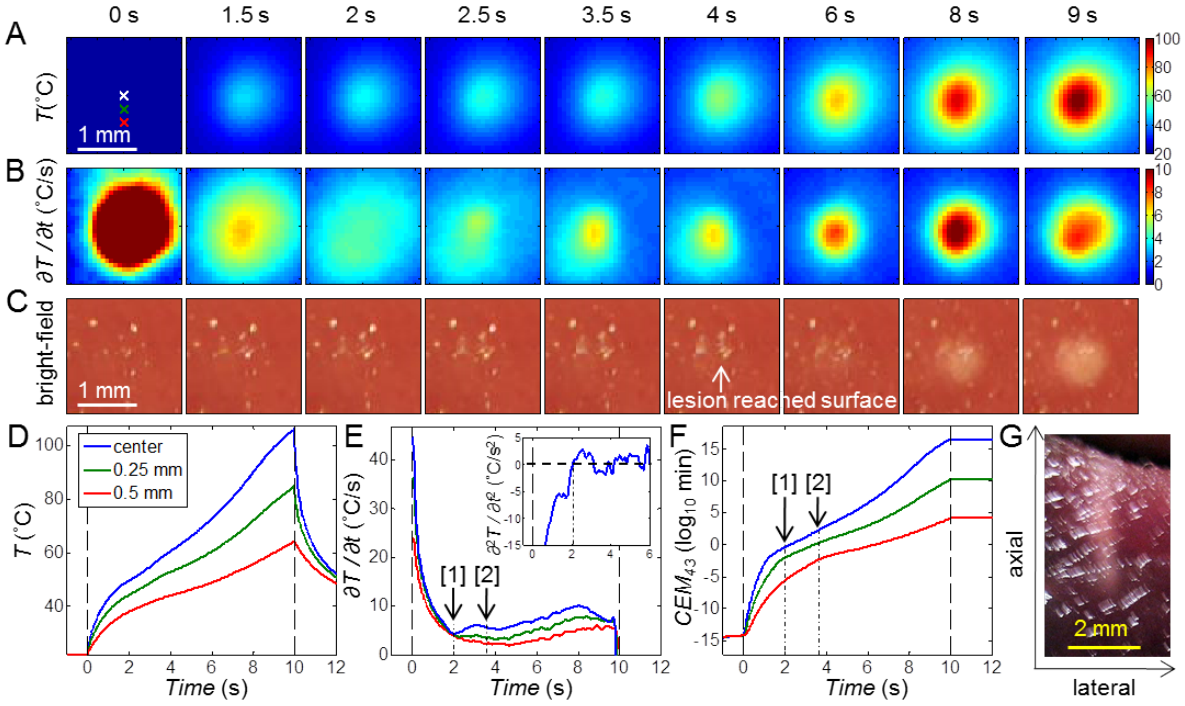

Figure 3.9 Ablative HIFU exposures (1060 W/cm^2, 10 s duration) with the focus placed at 3 mm beneath the surface. (A) IR images showing the surface temperature T (°C). (B) Images of the rate of temperature change $\partial T/\partial t$ (°C/s). (C) Bright-field images of the tissue surface showing lesion formation. (D) Time evolution of T at the center and 0.25 mm and 0.5 mm below the center (indicated on the first IR image in (A)). (E) Corresponding time evolution of $\partial T/\partial t$: [1] $\partial T/\partial t$ starts to increase at 2 s, suggesting lesion formation in subsurface; [2] The CEM_{43} reaches 170 min at 3.62 s, predicting lesion formation at the surface between 3.5 and 4 s (see frame with arrow in (C)). The upper-right box shows the time evolution of $\partial^2 T/\partial t^2$ (°C/s^2) at the center. The first zero-crossing occurred at 2 s. (F) Corresponding time evolution of CEM_{43}: [1] 0.42 min at 2 s; [2] 170 min at 3.62 s. (G) Gross image of the lesion cross-section. Axial is the direction which ultrasound beams propagated, from the bottom surface of the tissue to the top surface.

Using the criterion developed for lesion identification defined in Eq. (3.8), we classified the sets of experiments with a subsurface HIFU ablation based on the surface temperature measurements. We only considered $\ddot{\theta}$ with $\partial T/\partial t > 0.5$°C/s, which is a lower criterion compared to surface ablations (Sec. 3.3.2) due to the smaller temperature rise. Two sets of experiments were excluded due to skipped IR images, resulting in varying time intervals Δt which prohibited comparable time derivatives of temperature. Figure 3.10 shows the histogram of $\ddot{\theta}_{max}$ for all ablative (including HIFU outcomes of normal and overheated lesions, $n = 30$, 2102 locations) and non-ablative ($n = 7$, 363 locations) experiments. This classifier was determined to have an ROC AUC of 0.80 and with a threshold of $\ddot{\theta}_{max} = 0.03$ s^{-1} providing 84.1 % accuracy for lesion identification. When the lesion is at a larger depth, its effect on the surface temperature is reduced due to the longer distance for heat conduction to reach the surface. This also explains the smaller AUC compared to the classification with a surface HIFU focus (0.999, see Sec. 3.3.2).

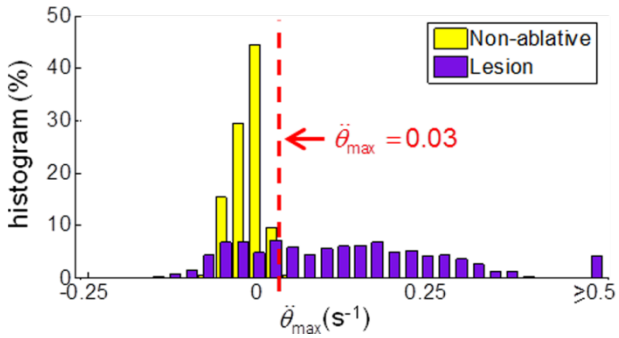

Figure 3.10 Determination of criterion for subsurface lesion formation: Histogram of the maximum normalized second derivative of temperature change $\ddot{\theta}_{max}$ for non-ablative and ablative HIFU ablations. The dashed line indicates a threshold of $\ddot{\theta}_{max} = 0.03$ s^{-1} which provided the highest accuracy for lesion identification.

Overheating: cavity formation and tissue dehydration. We examined whether similar characteristics of temperature irregularities, stagnation, and asymmetric distribution observed with the occurrence of cavity formation and tissue dehydration (or water extraction from tissue) in the cases of surface ablation (Sec. 3.3.2) can be regarded as indications of excessive heating in subsurface HIFU ablation.

Figure 3.11 shows a comparison of three temperature profiles from experiments where HIFU exposures (1500 W/cm^2) with durations of 5, 10, and 15 s were applied with the focus placed at 5 mm beneath the tissue surface. The temperature images (Fig. 3.11A) and time profiles (Figs. 3.11D and 3.11E, red line) for the shorter exposure ablation were smooth with no abrupt increase in $\partial T/\partial t$. (The effect of lesion formation on the surface temperature was reduced in these cases due to the longer distance for heat to conduct to the surface.) The gross image of the corresponding tissue section (Fig. 3.11F) shows a small lesion with no sign of cavity formation.

With longer exposure times (10 and 15 s) (Figs. 3.11B and 3.11C), the temperature profiles (Fig. 3.11D, green and blue lines, respectively) showed the temperature reaching a plateau with a slight drop around 8 s while the HIFU exposure was still on. Afterwards, asymmetry in the spatial distribution of the temperature was observed, with the location of the peak temperature shifted away from its original central location with time. This is similar to the cases with surface ablation where cavity formation and tissue dehydration/water extraction were observed. Although no direct correlation of subsurface HIFU events with the temperature evolution was obtained, lesions observed in the gross images (Fig. 3.11F) exhibited discoloration in the lesion core which is often associated with overheating. The

lesions also had a foam-like appearance, in contrast with the lesion generated by the 5 s HIFU exposure.

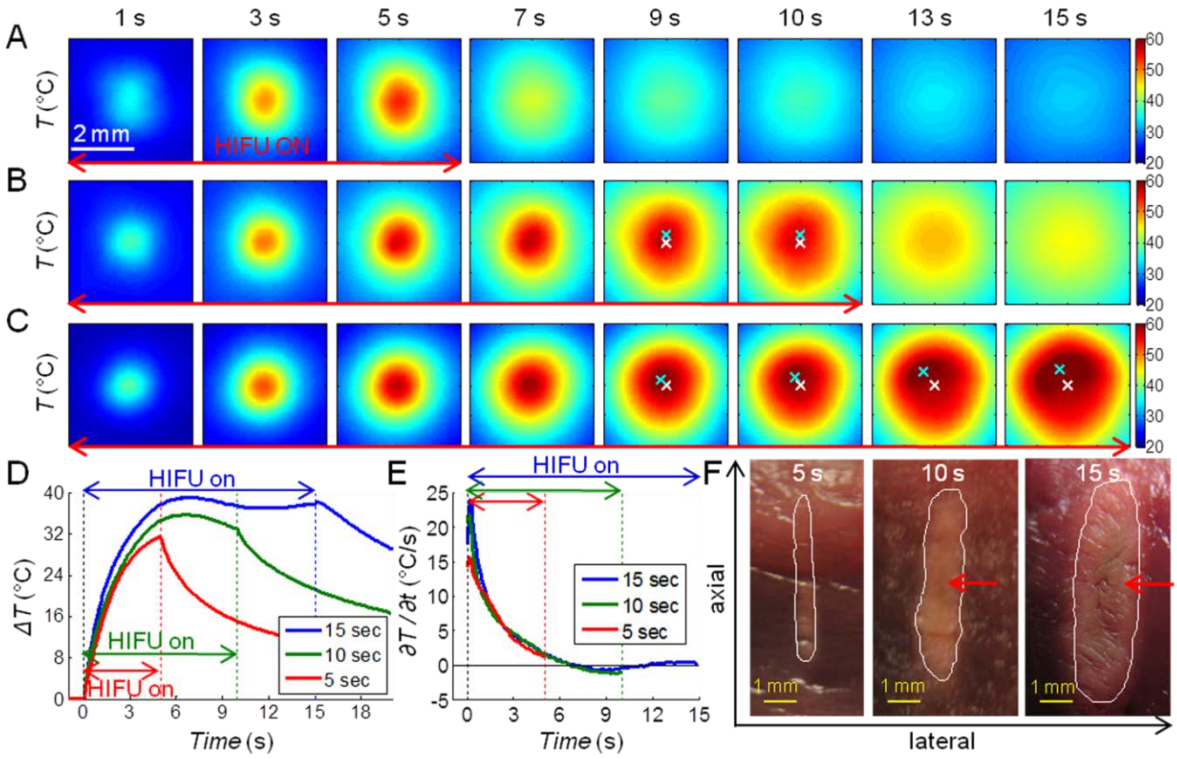

Figure 3.11 Three sets of IR images of temperature T (°C) during ablative HIFU exposures (1500 W/cm^2) with the focus placed at 5 mm beneath the surface. Duration of HIFU exposures is (A) 5 s, (B) 10 s, and (C) 15 s. The spatial peak temperature (cyan cross) and the original center focus (white cross) are indicated in (B) and (C). (D) Time evolution of the temperature change $\Delta T(t) = T(t) - T(t = 0)$ and (E) the rate of temperature change $\partial T/\partial t$ (°C/s) at the center of the temperature distribution. (F) Gross images of the lesion cross-sections. The white contours indicate manually-drawn lesion boundaries, and the red arrows indicate regions with discoloration, suggesting overheating. Axial is the direction which ultrasound beams propagated, from the bottom surface of the tissue to the top surface.

Figure 3.12 shows a box plot of d_{max} from surface temperature measurements in subsurface HIFU experiments. Using the unequal variance t-test, d_{max} for ablative HIFU exposures with overheating (0.842 ± 0.631 mm, n = 15) was significantly different from the non-ablative (0.206 ± 0.081 mm, n = 8, p < 0.01) and ablative HIFU exposures without overheating (0.204 ± 0.058 mm, n = 16, p < 0.01) cases. No significant difference occurred between the non-ablative and ablative HIFU exposures without overheating cases (p = 0.96). The threshold to distinguish between overheated and normal lesions is 0.29 mm providing 93.5 % accuracy with an ROC AUC of 0.99. d_{max} of the overheated lesions is larger in these experiments compared to the surface HIFU experiments (0.315 ± 0.113 mm, see Fig. 3.7), probably because the ultrasound propagation was blocked and/or disturbed in the subsurface volume, resulting in a more asymmetric surface temperature distribution.

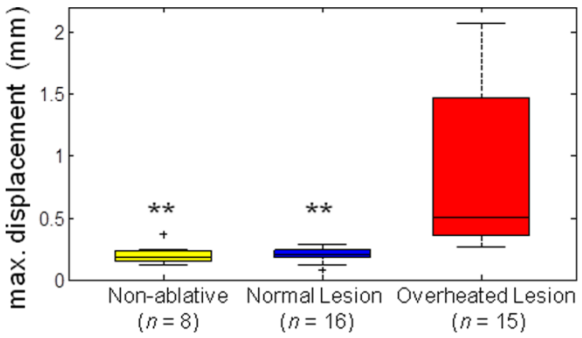

Figure 3.12 Determination of criterion for overheated subsurface lesions: Maximum displacement of spatial peak temperature location d_{max} from subsurface HIFU ablation experiments for non-ablative, normal lesion, and overheated lesion cases. The level of statistical significance compared with the overheated lesion cases is represented by double asterisk (**) if p < 0.01. A threshold of 0.29 mm provides the highest accuracy to differentiate between normal and overheated subsurface lesions.

3.3.4 Thermal probing: temperature distribution with and without HIFU lesions

Control images of temperature rise on the tissue surface generated by the lower intensity, non-ablative FUS exposure before any lesion generation are shown in Figs. 3.13A and 3.14A. A maximum temperature rise of 5.33°C was generated in both specimens. The images of temperature increase induced by the probing exposure after lesion formation in tissue (Figs. 3.13B and 3.14B) showed a higher temperature rise than the control case, with a maximum temperature rise of 8.70°C in Specimen 1 and 10.07°C in Specimen 2 (Figs. 3.13D and 3.14D). The difference in the temperature increase before and after lesion generation is shown in the subtracted images (Figs. 3.13C and 3.14C) as well as the initial heating rate *dT*/*dt* at the start of FUS exposures (Figs. 3.13E, 3.13F, 3.14E and 3.14F). The initial heating rate was dominated by the absorption before heat conduction comes into play.

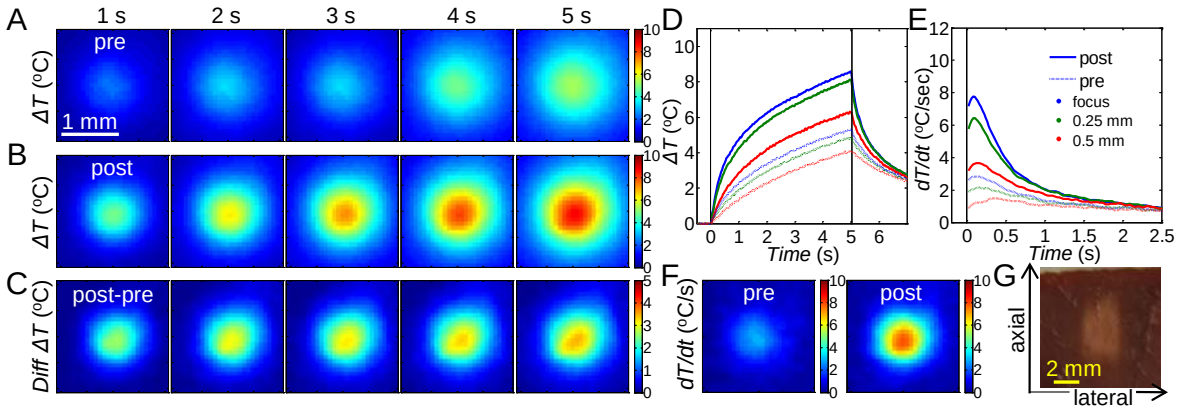

Figure 3.13 Thermal probing of Tissue Specimen 1 with smaller lesion volume: Images showing the temperature rise $\Delta T(x,y,t)$ during (A) pre-lesion probing, (B) post-lesion probing, and (C) the subtraction of the two (Diff $\Delta T(x,y,t)$= post $\Delta T(x,y,t)$−pre $\Delta T(x,y,t)$). (D) 1D plots of the temperature rise ΔT and (E) the rate of temperature change dT/dt at the center point, 0.25 mm and 0.5 mm to the right of the center. (F) The 2D rate of temperature change dT/dt at 0.1 s before and after lesion formation. (G) Gross image of the lesion cross-section. Lesion width = 2.88 mm.

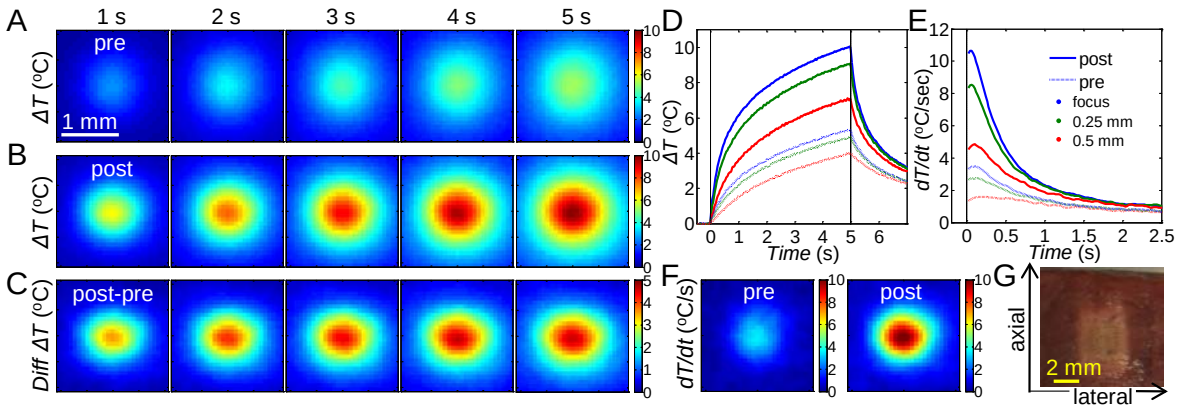

Figure 3.14 Thermal probing of Tissue Specimen 2 with larger lesion volume. (A-G) as in Fig. 3.13. Lesion width = 4 mm.

Current imaging methods where an external energy or heat source is applied to the target specimen to induce a temperature rise includes microwave imaging, active IR imaging,[31] and thermal strain imaging. The introduction of an additional heat source allows visualization of temperature-dependent tissue properties (e.g., speed of sound), and tissue properties related to heat absorption (e.g., acoustic and optical absorption coefficient) and dissipation (e.g., thermal conductivity). Tissue coagulation caused by HIFU ablation changes the tissue properties including heat capacity, attenuation coefficient, sound speed, and thermal conductivity. The change in attenuation is the most significant, and lesions in liver, spleen, and abdominal wall have been found to have twice or more times the attenuation coefficient that of corresponding native (untreated) tissue.[27,28,32] The use of non-ablative FUS exposures to assess tissue properties have been demonstrated with temperature measurements using thermocouples and ultrasound imaging.[33,34] The increase in temperature rise after the formation of subsurface lesions was still observable from the surface temperature (Figs. 3.13F and 3.14F). The results were also comparable to the increase in $\partial T/\partial t$ when lesions formed during HIFU ablation (Section 3.3.2). In these experiments, the temperature

field generated by HIFU was not wide enough to cover the entire lesion. The lesion widths were 2.88 and 4 mm (Figs. 3.13G and 3.14G), respectively, whereas the HIFU field only had a –6 dB focal width of 0.9 mm. However, the extent of the increased temperature rise was still dependent on the lesion size. An array system for beam forming and pulse sequencing which provides uniform heating[35] may improve and simplify interpretation of thermal probing results.

3.3.5 Limitations and future study

As seen from the current results, the use of temperature information during HIFU application can be complex because the irreversible changes of the thermal and acoustical properties of the tissue due to coagulation and the occurrence of bubble and cavity formation can significantly alter the normal course of temperature progression, thereby making it challenging to predict tissue status. While specific characteristics of the temperature evolution of the tissue were shown to provide useful information for monitoring HIFU ablation in this study, additional work will be needed to provide further improved unambiguous determination of specific events relevant to HIFU therapy.

By correlating IR and bright-field images during HIFU treatments spatiotemporally, we were able to determine the critical CEM_{43} for cardiac tissue coagulation experimentally. However, care must be taken when applying the critical CEM_{43} for predicting tissue coagulation. Errors may arise when the value used was obtained from experiments with a much different temperature range or heating mechanism (e.g., heating rate, intensity). For example, the time required for tissue coagulation in thermal therapy (> 50 °C) may be less than the critical CEM_{43} obtained from experiments in the hyperthermia temperature range (40 – 45 °C).[12] To make use of the simplicity of the thermal dose model and to ensure

prediction accuracy, a chart of applicable critical CEM_{43} in various different ranges of temperature could be further established using the same experimental set-up and processing method used in this study with varying HIFU intensities and exposure durations.

In this study, cavity formation and bubble generation were determined by visual inspection from the bright-field images. To monitor gas bubble or cavity formation, especially in the subsurface HIFU experiments, passive cavitation detection techniques[14,36,37] could be incorporated in future studies. It would also be of interest to determine whether bubbles and cavities are formed from boiling or acoustic cavitation or the combination of both under current HIFU settings.

It is possible that phenomena such as lesion formation, water dehydration and overheating may result in different temperature behaviors *in-vivo* and even for different tissue types. In order to provide temperature markers more relevant for *in-vivo* HIFU applications, the current study needs to be extended to experiments that consider other effects such as blood perfusion on HIFU ablation. Studies are also needed to more systematically determine the robustness and accuracy of the temperature markers for HIFU induced tissue coagulation and other changes. One area that could improve the current study is to implement better methods for detecting tissue coagulation on the surface because fast deposition of energy from HIFU application results in CEM_{43} varying significantly temporally and spatially, making the selection of lesion boundaries critical. For example, methods that can detect lesion formation on the cellular or molecular level will provide more accurate detection.

3.4 Conclusions

Experimental results obtained from this *ex-vivo* study demonstrate that parameters derived from the spatiotemporal changes of temperature measured at a tissue surface by real-time IR imaging exhibit characteristic changes corresponding to lesion formation, cavity generation, and water extraction/tissue dehydration during HIFU ablation. The temperature-derived parameters established in our study ($\ddot{\theta}_{\max}$, $d_{\max}$) have the potential to provide useful information for real-time HIFU monitoring. The study also demonstrated a method of determining of the critical CEM_{43} for cardiac tissue via spatiotemporal correlation of IR and bright-field images during HIFU exposure that provides results consistent with existing literature values. Results also demonstrate that thermal probing using lower intensity, non-ablative FUS exposures can detect the presence of lesion using IR temperature imaging.

The methods described herein suggest that IR imaging may be useful for direct HIFU monitoring where a tissue surface is accessible with a shallow HIFU focal location such as in breast cancer and skin cancer treatments or during open-chest/open-abdomen surgeries. The temperature-derived markers described in this study also have the potential serve to complement HIFU monitoring within a tissue volume by other methods, such as MRI, where direct determination of tissue status and other events is not possible in real time. As shown by the subsurface HIFU ablations, these temperature-derived parameters are applicable and useful even when direct temperature measurements of the region of interest are not feasible, provided the temperature information in the nearby regime is available.

3.5 References

1. H. H. Pennes, "Analysis of tissue and arterial blood temperatures in the resting human forearm," *J Appl Physiol* 1(2), 93-122 (1948)

2. W. L. Nyborg, "Solutions of the bio-heat transfer equation," *Phys Med Biol* 33(7), 785-792 (1988)

3. F. P. Curra, P. D. Mourad, V. A. Khokhlova, R. O. Cleveland and L. A. Crum, "Numerical simulations of heating patterns and tissue temperature response due to high-intensity focused ultrasound," *IEEE Trans Ultrason Ferroelectr Freq Control* 47(4), 1077-1089 (2000)

4. S. A. Sapareto and W. C. Dewey, "Thermal Dose Determination in Cancer-Therapy," *Int J Radiat Oncol* 10(6), 787-800 (1984)

5. D. Haemmerich, J. G. Webster and D. M. Mahvi, "Thermal dose versus isotherm as lesion boundary estimator for cardiac and hepatic radio-frequency ablation," in *Proc 25th Annual Intl Conf IEEE Engin Med Biol Soc*, 134-137, IEEE (2003)

6. C. A. Damianou, K. Hynynen and X. B. Fan, "Evaluation of accuracy of a theoretical-model for predicting the necrosed tissue volume during focused ultrasound surgery," *IEEE Trans Ultrason Ferroelectr Freq Control* 42(2), 182-187 (1995)

7. S. J. Graham, L. Chen, M. Leitch, R. D. Peters, M. J. Bronskill, F. S. Foster, R. M. Henkelman and D. B. Plewes, "Quantifying tissue damage due to focused ultrasound heating observed by MRI," *Magn Reson Med* 41(2), 321-328 (1999)

8. S. H. Wong, R. D. Watkins, M. Kupnik, K. B. Pauly and B. T. Khuri-Yakub, "Feasibility of MR-temperature mapping of ultrasonic heating from a CMUT," *IEEE Trans Ultrason Ferroelectr Freq Control* 55(4), 811-818 (2008)

9. A. H. Chung, F. A. Jolesz and K. Hynynen, "Thermal dosimetry of a focused ultrasound beam in vivo by magnetic resonance imaging," *Med Phys* 26(9), 2017-2026 (1999)

10. D. R. Daum, N. B. Smith, R. King and K. Hynynen, "In vivo demonstration of noninvasive thermal surgery of the liver and kidney using an ultrasonic phased array," *Ultrasound Med Biol* 25(7), 1087-1098 (1999)

11. P. S. Yarmolenko, E. J. Moon, C. Landon, A. Manzoor, D. W. Hochman, B. L. Viglianti and M. W. Dewhirst, "Thresholds for thermal damage to normal tissues: An update," *Int J Hyperthermia* 27(4), 320-343 (2011)

12. X. M. He, S. Bhowmick and J. C. Bischof, "Thermal therapy in urologic systems: a comparison of Arrhenius and thermal isoeffective dose models in predicting hyperthermic injury," *J Biomech Eng* 131(7), 074507 (2009)

13. V. A. Khokhlova, M. R. Bailey, J. A. Reed, B. W. Cunitz, P. J. Kaczkowski and L. A. Crum, "Effects of nonlinear propagation, cavitation, and boiling in lesion formation by high intensity focused ultrasound in a gel phantom," *J Acoust Soc Am* 119(3), 1834-1848 (2006)

14. C. C. Coussios, C. H. Farny, G. ter Haar and R. A. Roy, "Role of acoustic cavitation in the delivery and monitoring of cancer treatment by high-intensity focused ultrasound (HIFU)," *Int J Hyperthermia* 23(2), 105-120 (2007)

15. F. L. Lizzi, "High-precision thermotherapy for small lesions," *Eur Urol* 23 Suppl 1, 23-28 (1993)

16. K. Ogan, W. W. Roberts, D. M. Wilhelm, L. Bonnell, D. Leiner, G. Lindberg, L. R. Kavoussi and J. A. Cadeddu, "Infrared thermography and thermocouple mapping of radiofrequency renal ablation to assess treatment adequacy and ablation margins," *Urology* 62(1), 146-151 (2003)

17. C. Song, B. Tang, P. A. Campbell and A. Cuschieri, "Thermal spread and heat absorbance differences between open and laparoscopic surgeries during energized dissections by electrosurgical instruments," *Surg Endosc* 23, 2480-2487 (2009)

18. J. A. Cadeddu, S. V. Jackman and P. G. Schulam, "Laparoscopic infrared imaging," *J Endourol* 15(1), 111-116 (2001)

19. M. A. Groh, O. A. Binns, H. G. Burton, G. L. Champsaur, S. W. Ely and A. M. Johnson, "Epicardial ultrasonic ablation of atrial fibrillation during concomitant cardiac surgery is a valid option in patients with ischemic heart disease," *Circulation* 118(14), S78-S82 (2008)

20. S. Mitnovetski, A. A. Almeida, J. Goldstein, A. W. Pick and J. A. Smith, "Epicardial high-intensity focused ultrasound cardiac ablation for surgical treatment of atrial fibrillation," *Heart Lung Circ* 18(1), 28-31 (2009)

21. R. P. Madding, "Emissivity measurement using infrared imaging radiometric cameras," in *Encyclopedia of optical engineering* R. G. Driggers, Ed., 475-483, CRC Press, New York, NY (2003)

22. W. J. Fry and R. B. Fry, "Determination of absolute sound levels and acoustic absorption coefficients by thermocouple probes - theory," *J Acoust Soc Am* 26(3), 294-310 (1954)

23. C. E. Metz, "Basic principles of ROC analysis," *Semin Nucl Med* 8(4), 283-298 (1978)

24. N. V. Chawla, K. W. Bowyer, L. O. Hall and W. P. Kegelmeyer, "SMOTE: Synthetic minority over-sampling technique," *J Artif Intell Res* 16, 321-357 (2002)

25. J. Steketee, "Spectral emissivity of skin and pericardium," *Phys Med Biol* 18(5), 686-694 (1973)

26. D. Mitchell, C. H. Wyndham and T. Hodgson, "Emissivity and transmittance of excised human skin in its thermal emission wave band," *J Appl Physiol* 23(3), 390-394 (1967)

27. N. L. Bush, I. Rivens, G. R. ter Haar and J. C. Bamber, "Acoustic properties of lesions generated with an ultrasound therapy system," *Ultrasound Med Biol* 19(9), 789-801 (1993)

28. V. Zderic, A. Keshavarzi, M. A. Andrew, S. Vaezy and R. W. Martin, "Attenuation of porcine tissues in vivo after high-intensity ultrasound treatment," *Ultrasound Med Biol* 30(1), 61-66 (2004)

29. R. L. Clarke and G. R. ter Haar, "Temperature rise recorded during lesion formation by high-intensity focused ultrasound," *Ultrasound Med Biol* 23(2), 299-306 (1997)

30. C. A. Damianou, N. T. Sanghvi, F. J. Fry and R. Maass-Moreno, "Dependence of ultrasonic attenuation and absorption in dog soft tissues on temperature and thermal dose," *J Acoust Soc Am* 102(1), 628-634 (1997)

31. A. Nowakowski, "Quantitative active dynamic thermal IR-imaging and thermal tomography in medical diagnostics," in *Medical infrared imaging*, N. A. Diakides and J. D. Bronzino, Eds., 7-1-7-29, CRC Press, New York, NY (2008)

32. R. L. Clarke, N. L. Bush and G. R. ter Haar, "The changes in acoustic attenuation due to in vitro heating," *Ultrasound Med Biol* 29(1), 127-135 (2003)

33. H. Yao, R. Griffin and E. S. Ebbini, "Noninvasive localized ultrasonic measurement of tissue properties," in *2004 IEEE Ultrasonics Symp Proc*, 724-727 (2004)

34. D. Liu and E. S. Ebbini, "Real-time 2-D temperature imaging using ultrasound," *IEEE Trans Biomed Eng* 57(1), 12-16 (2010)

35. T. Hall and C. Cain, "A low cost compact 512 channel therapeutic ultrasound system for transcutaneous ultrasound surgery," *AIP Conf Proc* 829, 445-449 (2006)

36. B. A. Rabkin, V. Zderic, L. A. Crum and S. Vaezy, "Biological and physical mechanisms of HIFU-induced hyperecho in ultrasound images," *Ultrasound Med Biol* 32(11), 1721-1729 (2006)

37. T. D. Mast, V. A. Salgaonkar, C. Karunakaran, J. A. Besse, S. Datta and C. K. Holland, "Acoustic emissions during 3.1 MHz ultrasound bulk ablation in vitro," *Ultrasound Med Biol* 34(9), 1434-1448 (2008)

Chapter 4

Dual-wavelength photoacoustic technique for monitoring tissue status during thermal treatments

Photoacoustic (PA) techniques have been exploited for monitoring thermal treatments including high-intensity focused ultrasound (HIFU) ablations.[1,2] It also allows a deeper imaging depth compared to infrared thermography discussed in Chapter 3. However, PA signals depend on not only tissue temperature but also tissue optical properties, which indicate tissue status (e.g., native or coagulated). The changes in temperature and tissue status often occur simultaneously during thermal treatments, so both effects cause changes to PA signals. In this chapter, we propose a new dual-wavelength PA technique to monitor tissue status independent of tissue temperature. Real-time HIFU monitoring was not performed due to limitations on our laser system, but the feasibility was demonstrated on pre-generated HIFU lesions and real-time tissue changes was investigated through experiments subjected to water-bath heating.

The work in this chapter has been published in Journal of Biomedical Optics 18(6), 067003 (2013) entitled “Dual-wavelength photoacoustic technique for monitoring tissue status during thermal treatments”.

4.1 Introduction

PA effect refers to a phenomenon in which thermoelastic pressure waves (acoustic waves) are generated by the absorption of electromagnetic energy (e.g., optical or radiofrequency waves).[3] PA imaging often uses short nanosecond laser pulses to excite megahertz ultrasound waves from optically absorbing objects, thus derives its imaging contrast from the optical properties of the imaged object. PA imaging has been shown to be capable of providing structural, functional and molecular information,[3,4] and is capable of visualizing deeply seated tumors[4,5] and showing tumor vasculature.[6] Recent advances in PA imaging enable achievement of microscopic resolution from a few microns[7] down to submicron.[8] Its potential as a diagnostic tool is also intensively investigated.[4,9] However, studies on the use of PA imaging for real-time monitoring of therapeutic processes are still at an early stage.

A system for PA-guided HIFU ablation has its advantage by using the same ultrasound transducer (either a single element transducer[10] or an array probe[11]) for both the HIFU treatment and PA signal detection. Estimation of tissue temperatures below coagulation level may be achieved from PA signal intensity.[12-15] Real-time temperature monitoring using PA techniques has been explored during photothermal[16-18] and HIFU treatment.[1,2] Most of these studies focused on temperature measurements although tissue alteration during the thermal treatments, which resulted in changes in tissue optical properties, also contributed to the changes in PA signals. From empirical observations, a relation between PA signal intensity and thermal dose, instead of temperature, has been suggested as a better parameter for coagulation monitoring.[1] In all these studies, laser excitation at a single wavelength in the visible or near-infrared spectrum was employed, and to estimate

temperature, a relation between PA signals and temperature was acquired in advance as a calibration.[14,16]

Another suggested PA method for thermal treatment monitoring is based on the changes in the optical properties in thermally treated tissues. Tissues at different statuses (e.g., native or coagulated) have different compositions, resulting in different optical properties. Therefore PA signal intensity is dependent on the tissue status. In most studies, the PA signal intensity increased during or after coagulation, presumably as a result of the increased chromophore concentration due to dehydration[19] and/or the formation of methemoglobin (MetHb), a strong optical absorber over a broad optical spectrum.[19-21] Contradictory to the findings from most *ex-vivo* studies, Chitnis et al. reported a negative contrast in HIFU lesions in the kidney of a live rat,[22] which was explained by the difference in the heating mechanism and the difference between *in-vivo* and *ex-vivo* conditions. However, no matter whether coagulated tissue exhibits a negative or positive contrast, PA signals at a single wavelength cannot provide a clear indication of tissue changes in real-time because the increasing temperature during thermal treatment also affects PA signals.

Considering the thermal expansion of an absorbing medium heated by a short laser pulse with incident laser fluence F_0, the PA effect can be expressed by calculating the pressure rise $\Delta P(z)$ in the irradiated volume under temporal pressure confinement[23,24]

$$\Delta P(z) = \left(\frac{\beta c^2}{C_p}\right)\mu_a F = \Gamma \mu_a F(z) = \Gamma \mu_a e^{-z\sqrt{3\mu_a(\mu_a+\mu_s')}} F_0, \tag{4.1}$$

where μ_a and μ_s' are the optical absorption coefficient and reduced scattering coefficient, respectively; z is the depth along the photoacoustic receiving beam; and $\Gamma = \beta c^2/C_p$ is the Grüneisen parameter with β, c, and C_p being the thermal coefficient of volume expansion,

speed of sound, and heat capacity at constant pressure, respectively. Γ is both temperature and tissue type/status dependent. When the tissue status remains unchanged, Γ is often empirically assumed to be linearly related to temperature.[14] However, variations in the contents of water, lipid, proteins and other materials in different tissues yield different β, c, and C_p, and different dependencies of these parameters on temperature.[14,25] For example, PA signal amplitude in lipid-rich plaques and lard decreases with temperature rise, which is clearly different from water-based tissues.[26,27]

In order to resolve the problem of combined effects from tissue temperature and optical properties on PA signals during thermal treatments, we propose a dual-wavelength PA technique. The temperature-dependent Γ in Eq. (4.1) is removed by dividing PA signal intensities obtained at two different wavelengths at the same temperature. The resulting ratio will then depend only on the tissue optical properties, thus tissue status may be obtained without the effect of tissue temperature. In this study, we conducted experiments using water bath heating of *ex-vivo* porcine myocardium tissue specimens to test our proposed dual-wavelength PA technique. Its feasibility for HIFU monitoring was demonstrated using two experimental groups, one with untreated tissue samples and the other with HIFU treated tissue samples including thermal coagulated lesion.

4.2 Materials and methods

4.2.1 Theory of dual-wavelength PA technique

In this study, we examined the simplest case where the PA signals were generated from locations close to tissue surface. In this case, Eq. (4.1) can be simplified into $\Delta P(z=0)=\Gamma\mu_a F_0$. In most former studies,[2,12-16,18] the temperature dependency of tissue optical properties was not considered because major tissue absorbers, such as hemoglobin, have been reported to exhibit minor changes in optical absorption (< 3.5 %) over the temperature range of 20 – 40 °C.[28] It was also found that, in the temperature range below coagulation threshold, the optical absorption coefficient μ_a in both human skin[29] and canine prostate[30] had not much change with increased temperature. Although in these studies, negligible changes in optical absorption with temperature increase were observed only at low temperature range (up to 40 °C) since it is not feasible to measure the optical properties at high temperatures without inducing changes in tissue composition, we assume that the temperature dependency of tissue optical properties would still be negligible through the entire temperature range (up to temperatures above coagulation threshold). On the contrary, μ_a is highly dependent on the tissue type/status. For example, thermal induced tissue coagulation could lead to significant changes in μ_a.[31-35] Therefore, in this work, μ_a is expressed as a function of laser wavelength and tissue type/status. The laser-induced pressure rise can now be expressed as

$$\Delta P=\Gamma\left(\text{tissue status } s,\text{ temperature } T\right)\cdot\mu_a\left(\text{tissue status } s,\text{ wavelength } \lambda\right)F_0. \quad (4.2)$$

If we obtain PA signals using two different wavelengths, λ_1 and λ_2, at the same temperature and the same time when the tissue status is also the same, the induced pressure rise can be written as $\Delta P_{(s,T,\lambda_1)}=\Gamma_{(s,T)}\mu_{a(s,\lambda_1)}F_{0(\lambda_1)}$ and $\Delta P_{(s,T,\lambda_2)}=\Gamma_{(s,T)}\mu_{a(s,\lambda_2)}F_{0(\lambda_2)}$, at the two wavelengths

respectively. By dividing $\Delta P_{(s,T,\lambda_1)}$ with $\Delta P_{(s,T,\lambda_2)}$, we define a temperature independent parameter or ratio *k* as

$$k = \frac{\Delta P_{(s,T,\lambda_1)}}{\Delta P_{(s,T,\lambda_2)}} = \frac{\Gamma_{(s,T)}\mu_{a(s,\lambda_1)}F_{0(\lambda_1)}}{\Gamma_{(s,T)}\mu_{a(s,\lambda_2)}F_{0(\lambda_2)}} = \frac{\mu_{a(s,\lambda_1)}}{\mu_{a(s,\lambda_2)}} \cdot \frac{F_{0(\lambda_1)}}{F_{0(\lambda_2)}} = \frac{\mu_{a(s,\lambda_1)}}{\mu_{a(s,\lambda_2)}} \cdot m, \quad (4.3)$$

where $m = F_{0(\lambda_1)} \big/ F_{0(\lambda_2)}$ is irrelevant to the tissue and, therefore, can be assumed constant if the light fluence on the sample is stable or can be normalized by monitoring the laser output energy. Now that the temperature-dependent Γ is eliminated from the equation, the parameter *k* depends only on the optical properties of the tissue, and should be a constant for the same tissue type/status under different temperatures. Because *k* may be different for different tissue types and may change when tissue alteration occurs (e.g., coagulation), it can be used to differentiate various tissues or as an indicator for thermal induced tissue coagulation.

Upon examination of the pressure rise obtained at different temperatures, T_0 and T_1, with corresponding tissue statuses s_0 and s_1, we can write $\Delta P_{(s_0,T_0,\lambda)} = \Gamma_{(s_0,T_0)}\mu_{a(s_0,\lambda)}F_{0(\lambda)}$ and $\Delta P_{(s_1,T_1,\lambda)} = \Gamma_{(s_1,T_1)}\mu_{a(s_1,\lambda)}F_{0(\lambda)}$ based on Eq. (4.2). The relative signal change from T_0 to T_1 is therefore expressed as

$$\frac{\Delta P_{(s_1,T_1,\lambda)} - \Delta P_{(s_0,T_0,\lambda)}}{\Delta P_{(s_0,T_0,\lambda)}} = \frac{\Gamma_{(s_1,T_1)}\mu_{a(s_1,\lambda)}F_{0(\lambda)} - \Gamma_{(s_0,T_0)}\mu_{a(s_0,\lambda)}F_{0(\lambda)}}{\Gamma_{(s_0,T_0)}\mu_{a(s_0,\lambda)}F_{0(\lambda)}} = \frac{\Gamma_{(s_1,T_1)}\mu_{a(s_1,\lambda)} - \Gamma_{(s_0,T_0)}\mu_{a(s_0,\lambda)}}{\Gamma_{(s_0,T_0)}\mu_{a(s_0,\lambda)}}. \quad (4.4)$$

If the tissue status remains the same from T_0 to T_1, then $s_1 = s_0$ and the relative signal change is simplified to $\left(\Gamma_{(s_0,T_1)} - \Gamma_{(s_0,T_0)}\right) \big/ \Gamma_{(s_0,T_0)}$ which is independent of the laser wavelength. Therefore we can expect the relative signal change to be the same for different wavelengths when there is no change in tissue type/status.

4.2.2 HIFU ablation and dual-wavelength PA sensing

Ex-vivo porcine myocardium specimens obtained from the local abattoir were used in this study. To demonstrate the ability of dual-wavelength PA detection technique in monitoring tissue status without being affected by temperature change, one group of tissue specimens were treated with HIFU application to generate thermal lesions prior to PA measurement; while the other group of specimens was untreated. The HIFU system consisted of a HIFU transducer (2 MHz center frequency, F = 0.98, Blatek, Inc., State College, PA), a delay/pulse generator (Model 565, Berkeley Nucleonics Corp., San Rafael, CA), a function generator (33220A, Agilent, Santa Clara, CA), and a power amplifier (325LA, ENI, Rochester, NY) is shown in Fig. 4.1A. A tissue specimen (22 mm × 22 mm × 13 mm) was placed in a plastic holder with the front and the back sides covered by acoustically transparent membranes (Tegaderm, 3M, St. Paul, MN) to prevent possible changes in hydration and concentration of chromophores in the tissue specimen when submersed in water. Each ablation was conducted using a 20 sec pulsed HIFU exposure (1500 W/cm^2 focal intensity, 80% DC, 10 Hz PRF) with the HIFU focus aimed near the tissue surface for visual confirmation of the ablation outcome. The HIFU transducer was moved using translation stages to generate a bigger volume of necrotized tissue.

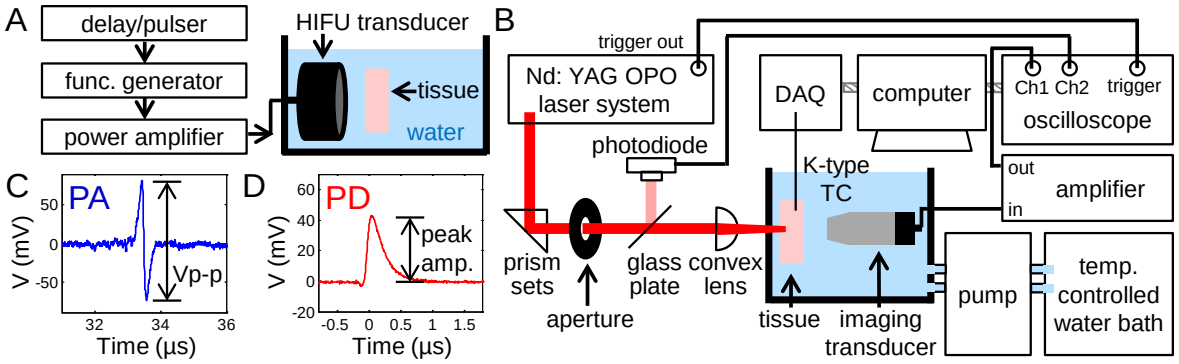

Figure 4.1 Schematic illustration of experimental set-up for (A) HIFU ablation and (B) PA sensing in a temperature controlled water bath. (C, D) Typical photoacoustic (PA) signal and photodiode (PD) signal. Vp-p denotes the peak-to-peak amplitude.

Fig. 4.1B shows the schematic experimental setup to obtain PA signals from the HIFU lesions and non-treated tissues at various temperatures. The system consisted of a temperature-controlled water bath (Precision 280, Thermo Scientific, Waltham, MA), a circulating pump (Peri-Star Pro, World Precision Instruments, Inc., Sarasota, FL), a focused imaging transducer (10 MHz center frequency, V311, Panametrics, Waltham, MA), and a laser source. Tissue temperatures were controlled using the water bath and measured with a K-type thermocouple (0.08 mm diameter, Omega Engineering, Stamford, CT), which was inserted in the specimen and sampled at 20 Hz by a data acquisition system (OMB-DAQ-3000, Omega Engineering). An Nd:YAG (Brilliant B, Quantel, Bozeman, MT) pumped optical parametric oscillator (OPO) system (Vibrant 532 I, Opotek Inc., Carlsbad, CA) provided laser pulses at 700 nm and 800 nm wavelengths with a pulse duration of 5.5 ns and a pulse repetition rate of 10 Hz. These two wavelengths were chosen for two main reasons: (1) the output energy from the laser system is strong and stable in this range; (2) the optical absorptions of oxygenated hemoglobin (HbO_2), deoxygenated hemoglobin (Hb), and MetHb are different between 700 nm and 800 nm,[36,37] which allows the detection of changes in

concentrations of these chromophores due to thermal coagulation. The energy of the laser beam was measured using a photodiode (Model 2031, New Focus, Santa Clara, CA) for later normalization. The PA signals received from the imaging transducer, which worked on the transmission mode, was first amplified by 40 dB with a pre-amplifier (5052PR, Panametrics) and then recorded with a 200 MHz sampling rate on a digital oscilloscope (54380B, Agilent). In this experiment, the temperature was only increased from room temperature to 43 °C to prevent any tissue alteration. For all measurements, the laser beam was centered at the lesion center and the beam size (3 mm in diameter) was smaller than the lesion cross section. PA signals were acquired for 10 sec at each wavelength at each temperature. Gross photos of the tissue specimens were taken after the experiment.

4.2.3 PA spectrum

The PA spectra of the native tissue and HIFU lesions were obtained using the same set-up in Fig. 4.1B. The OPO system was tunable between 680 nm to 950 nm. PA spectrum measurement was performed twice on each specimen: one was a native (untreated) tissue specimen and the other was a tissue specimen with pre-generated HIFU lesions. PA signals were acquired from 680 nm to 950 nm with a 5 nm step size and for 5 sec at each wavelength. The energy of the laser beam was also measured using the photodiode for later normalization. All measurements were performed with the tissue specimen immersed in 23.6 °C water bath.

4.2.4 Thermal treatments using water bath heating

To investigate the changes in signal ratio *k* during thermal treatments, PA sensing was performed on tissue specimens undergoing water bath heating using the same set-up in Fig. 4.1B. The temperature of the water tank was gradually increased from 35 °C to 60 °C, a range to ensure that tissue coagulation occurred during treatment. The heating rate was 0.20 ± 0.03 °C/min from 43 °C to 54 °C and 0.06 ± 0.02 °C/min from 54 °C to 60 °C. The circulating temperature-controlled system required a longer time to raise water temperature at higher temperatures, resulting in the slower heating rate above 54 °C. At each temperature/time measurement point, PA signals were acquired first at 700 nm and then at 800 nm.

4.2.5 Data processing

The normalized PA amplitude was obtained by dividing the peak-to-peak PA signal amplitude (Fig. 4.1C) by the peak amplitude of the photodiode signal (Fig. 4.1D) to minimize the effect due to the fluctuation of the laser energy over time. The measured PA signals were averaged over 10 sec to improve signal-to-noise ratio (SNR). We denote the averaged normalized PA amplitude as *P*. The ratio *k* (which may differ from the *k* in Eq. (4.3) by some constant) was computed using

$$k = P_{700\text{ nm}} / P_{800\text{ nm}}\,, \tag{4.5}$$

where $P_{700\text{ nm}}$ and $P_{800\text{ nm}}$ are the measurements obtained at laser wavelengths of 700 nm and 800 nm, respectively.

To investigate how PA signals depend on temperature and to compare between different wavelengths, the relative signal change (%) of P over temperature was computed based on Eq. (4.4) using

$$\text{relative signal change (\%) at temperature } T = \frac{\left(P_{\lambda,T} - P_{\lambda,T_0}\right)}{P_{\lambda,T_0}} \times 100\%, \qquad (4.6)$$

where λ is 700 nm or 800 nm, and T_0 is the reference temperature.

4.3 Results

4.3.1 PA spectra of native tissue and HIFU lesion

The PA spectra acquired from the native tissue (Fig. 4.2A) and HIFU lesions (Fig. 4.2B) are plotted using the averaged normalized PA amplitude P (averaged over 5 sec). The ratio of P between the HIFU lesions and native tissue (Fig. 4.2D) was calculated by first averaging P from the two measurements (solid red lines in Figs. 4.2A and 4.2B) and then taking their ratio. The PA spectrum of the HIFU lesion has a larger signal intensity compared to that of native tissue across the wavelengths investigated, with the largest increase at the lower end of the spectrum (Fig. 4.2D). $P_{\text{HIFU lesion}}/P_{\text{native tissue}}$ = 7.814 at 700 nm and 5.784 at 800 nm.

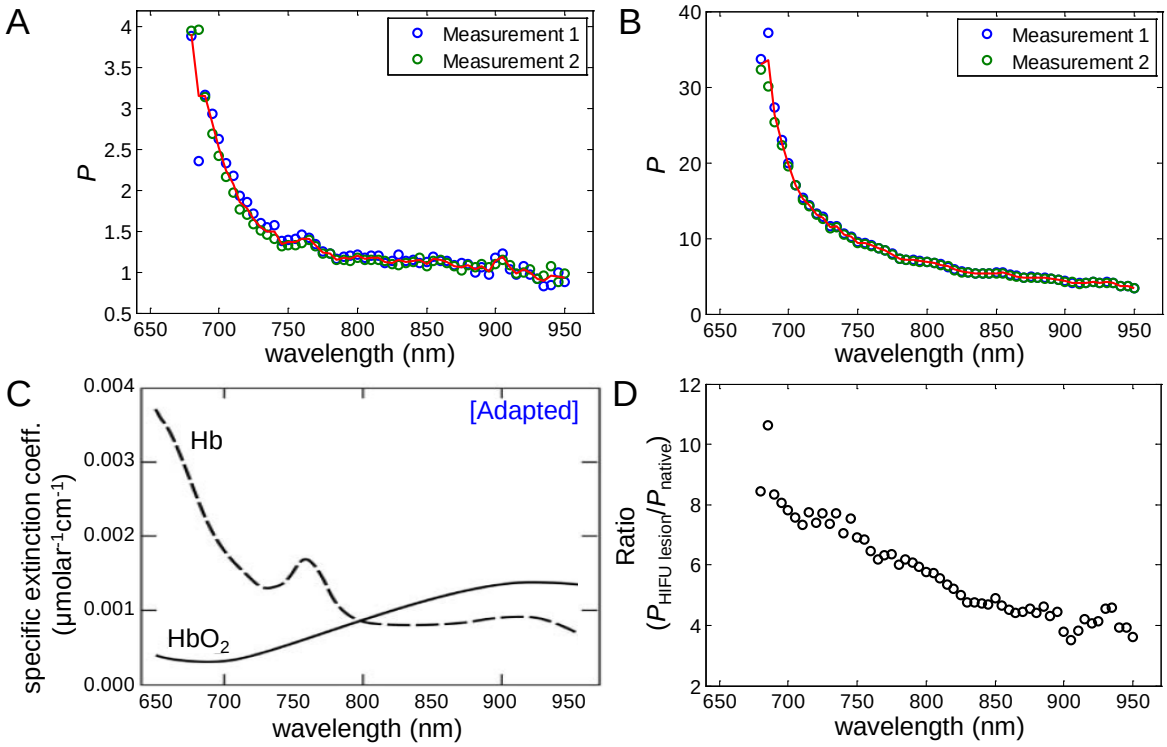

Figure 4.2 Spectrum of averaged normalized PA amplitude P at 680 – 950 nm wavelengths in (A) native tissue and (B) HIFU lesions. The solid red lines are the average from Measurement 1 and 2. (C) Extinction coefficient spectrum of deoxygenated hemoglobin (Hb) and oxygenated hemoglobin (HbO_2). Adapted from[38] D. Delpy and M. Cope, "Quantification in tissue near-infrared spectroscopy," *Philos Trans R Soc B*, 352(1354), 649-659(1997). (D) Ratio = $P_{\text{HIFU lesion}}/P_{\text{native tissue}}$.

4.3.2 Ratio k is temperature-independent

As an example, Fig. 4.3A shows the gross photo of a HIFU lesion on the surface of a tissue specimen. As shown in Figs. 4.3B and 4.3C, the mean ± standard deviation (S.D.) of the relative signal change (%) of the averaged normalized PA amplitude P in the native (no coagulated lesion) tissues (N = 9) and in the HIFU lesions (N = 8) computed using Eq. (4.6) exhibits the same trend for both wavelengths used in the experiments. Since the temperature range was kept below 43 °C, and measurements were made within two hours for each sample, no tissue alteration occurred as observed from the gross photo and calculated using the thermal damage model.[39-41] Thus these results confirmed that the relative percentage change

in the PA signal intensity is independent of the wavelength at any temperature when the tissue properties remain unchanged. Therefore the ratio k between these two wavelengths is expected to be constant at different temperatures, as demonstrated in Fig. 4.4, where $k = P_{700\text{ nm}}/P_{800\text{ nm}}$ is constant from 25 to 43 °C. Combining all data obtained from individual specimens and at ten different temperatures, $k = 2.28 \pm 0.20$ in native tissues ($N = 90$) and 2.70 ± 0.18 in HIFU lesions ($N = 80$). The difference in the k value between these two groups is statistically significant (p-value < 0.001). The threshold for differentiating the two groups is $k = 2.52$, as determined using the receiver-operating characteristic (ROC) curve,[42] providing an 85.3 % accuracy with an area under curve (AUC) of 0.93.

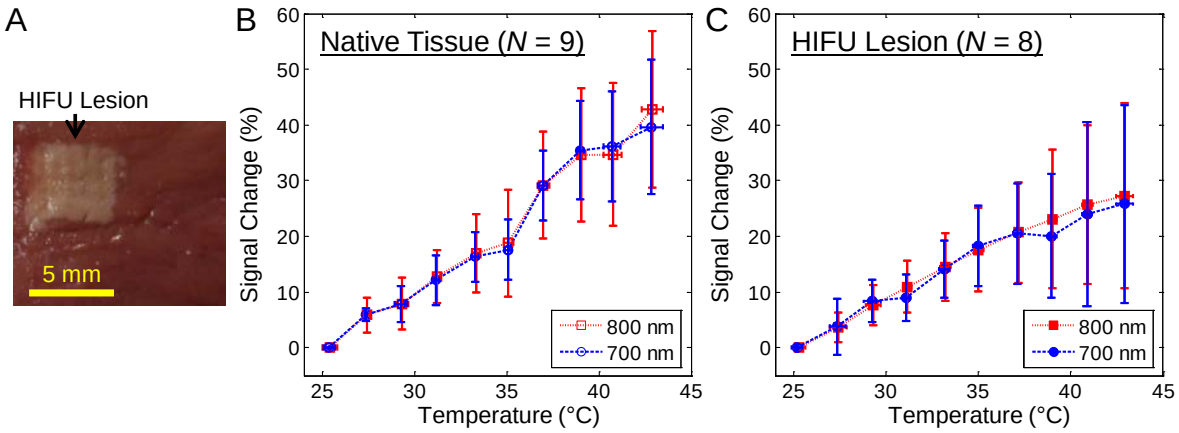

Figure 4.3 (A) Gross photo of a tissue specimen with a HIFU lesion generated before PA experiment. (B, C) The relative signal change (%) of the averaged normalized PA amplitude P in native tissues and in HIFU Lesions. $T_0 = 25.3 \pm 0.3$ °C.

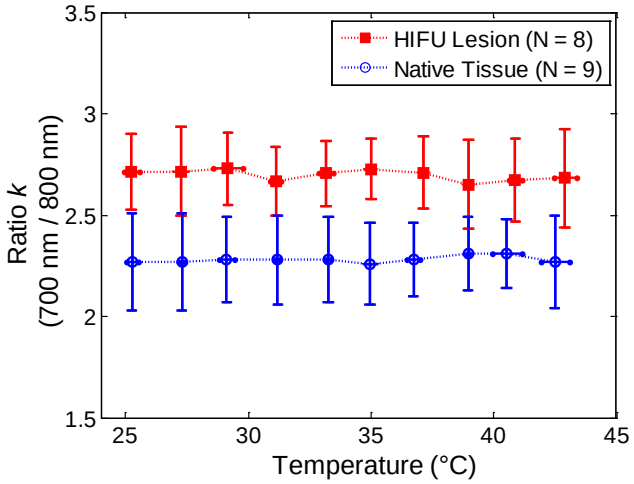

Figure 4.4 Comparison of the dual-wavelength ratio *k* (700 nm/800 nm) in HIFU lesions and native tissues as a function of temperature.

4.3.2 Ratio k increases with tissue changes during thermal treatment

The averaged normalized PA signal *P* at 700 nm and 800 nm from one tissue specimen subjected to water bath heating are shown in Figs. 4.5A and 4.5B to illustrate the change of PA signals with increasing temperature. Both of the PA signal amplitudes obtained with 700 nm and 800 nm laser excitations increased with increasing tissue temperature, with a relatively slower increase below 50 °C and a much faster increase when temperature increased further. However, from either of these single wavelength results, it is difficult to determine when exactly coagulation or changes in tissue status/content occurred, as both increased temperature and tissue alteration caused the PA signals to increase in amplitude.

By taking the ratio of the PA signals from the two wavelengths to eliminate the effect of temperature in the PA signals, the change in tissue status can be better identified as shown in Fig. 4.5C. Unlike *P* which is temperature dependent, *k* is nearly constant with increasing temperature until a sharp increase appeared at 56 °C, which allows clear identification of the temperature at which changes in tissue occurred.

Fig. 4.6A shows the mean ± S.D. of ratio *k* from five independent measurements. Again, it can be seen that *k* is nearly constant before it increases sharply at 55 °C, suggesting changes in the optical properties of the tissues during the coagulation process occurred at this temperature. Coagulation of the tissue samples was confirmed at the end of each experiment. Coagulated tissue appeared pinkish and white in contrast to its original dark red color. Individual curves of *k* for all five specimens are shown in Fig. 4.6B. *k* in each experiment follows a similar trend exhibiting a constant value before it increases sharply at a temperature between 55 to 58 °C.

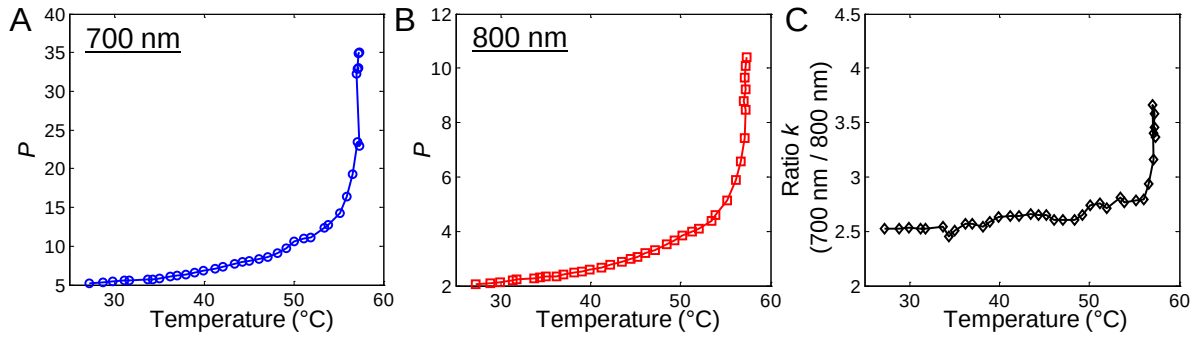

Figure 4.5 An example of coagulation during water bath heating: (A, B) The averaged normalized PA amplitude *P* as a function of temperature at 700 nm and 800 nm wavelengths. (C) Corresponding dual-wavelength ratio *k* (700 nm/800 nm).

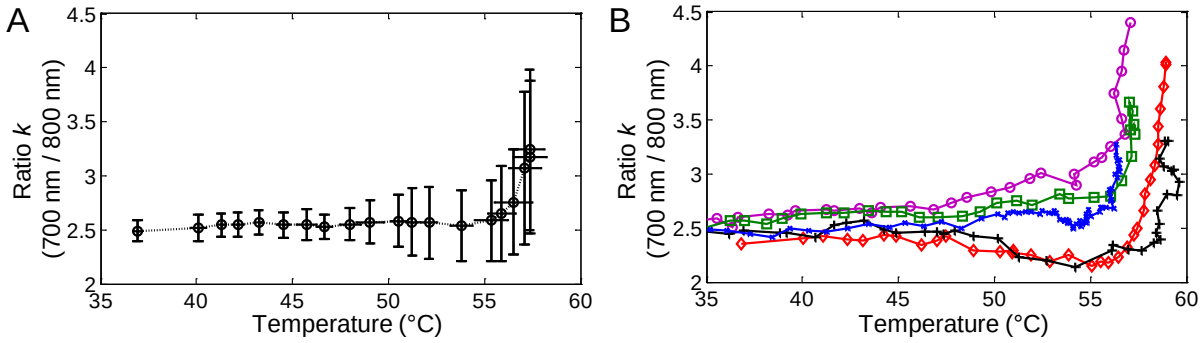

Figure 4.6 Dual-wavelength ratio *k* (700 nm/800 nm) during the coagulation process: (A) Mean ± S.D. (*N* = 5) and (B) individual plots as a function of temperature (°C).

In two sets of measurements, the coagulated tissues were allowed to cool down using the temperature-controlled water bath and k values were obtained in the coagulated tissues at a lower temperature range of $37 - 44$ °C. Our experiments confirmed that k remained constant in this temperature range, similarly as the native tissue samples, except that $k = 5.00 \pm 0.27$ in the coagulated tissues ($N = 19$), which is statistically significantly different from their native state when $k = 2.55 \pm 0.13$ ($N = 14$) with a p-value < 0.001, indicating that the tissue status alone affects the values of k.

4.4 Discussion

4.4.1 Temperature dependence of PA signals

In both experiments when tissue temperature increased with and without generating tissue alterations (Figs. 4.3B. 4.3C, 4.5A, 4.5B), the averaged normalized PA amplitude P increased as reported in previous studies.[1,27,43] The relative signal change (%) in the two tissue types (i.e., with and without HIFU lesion) changes linearly with temperature (in the range of $25 - 43$ °C, without inducing tissue changes) for both wavelengths used, but with a different percentage change under the same temperature increment (Figs. 4.3B and 4.3C). The reason that HIFU lesions have a smaller averaged relative percentage change is likely due to lesser water content in the coagulated tissue compared to non-treated tissues, and β and c of water have higher and positive dependency on temperature.[25] The large S.D. in the relative signal change in both tissue types may be attributed to the variations in tissue composition between different samples, leading to β and c having different dependencies on temperature.[25]

For temperature estimation with PA sensing using a single laser wavelength, a calibration curve determining the relation between PA signal amplitude and temperature is usually required for a specific tissue type. This can be tedious and prone to error, as there are variations in the tissue composition or the proportion of each component from sample to sample. Inaccurate temperature estimations for thermal treatment monitoring can occur if a general calibration curve is used. In comparison, dual-wavelength PA sensing can directly monitor the tissue status change during thermal treatment process, as the ratio *k* remains constant even with increasing temperature until a marked increase occurs due to tissue coagulation. No calibration on the signal-temperature relationship is needed beforehand. In addition, the distinct *k* values for native tissues and HIFU lesions can be used for tissue characterization to detect HIFU lesions.

It is noticed that *k* is smaller in HIFU lesions (Fig. 4.4) measured in our experiments compared to tissue samples coagulated by water bath heating (Fig. 4.6). The differences between the two heating processes (HIFU is fast and localized while water bath heating is slow and global) may lead to different tissue compositions in the coagulated tissues. Another possible reason for the higher *k* in tissues subjected to water bath heating is the much larger coagulated tissue volume as the coagulation occurred in the entire tissue specimen, unlike the HIFU lesions which were of much smaller dimensions (lesion depth ~0.5 mm). Also, ratio *k* of the water bath heated tissue appeared to continue to increase at the end of the heating period, suggesting that further coagulation was possible if longer and/or higher temperature heating was applied.

4.4.2 Changes in optical properties of coagulated tissue

The PA spectrum acquired in native tissue (Fig. 4.2A) exhibits a similar trend as the extinction spectrum of Hb (Fig. 4.2C). Since *ex-vivo* specimens were used in our experiments, the deoxygenation of blood which occurs immediately after the animals are sacrificed[44,45] is likely to result in Hb being the main contributor to the acquired PA signals. To choose the best wavelengths for maximum contrast or sensitivity to monitor tissue changes during thermal treatment, a complete spectrum over a broad range of wavelengths should be investigated to determine the absorption spectrum of each tissue statuses. Although we measured the PA spectrum of the native tissue (Fig. 4.2A) and HIFU lesions (Fig. 4.2B) from 680 nm to 950 nm, measurements up to or higher than 1100 nm where water absorption of light becomes significant may provide additional insight to the role of water content during the tissue coagulation process. Nilsson et al.[46] showed the absorption spectra for rat liver in the native state and laser induced coagulated state, where μ_a in general increased after laser treatment for the wavelengths investigated (600 – 1050 nm) with a slightly higher increase at 700 nm compared to 800 nm. Ritz et al.[47] (400 – 2400 nm) also showed that porcine liver with water bath heating exhibited an increase in μ_a, more at 700 nm compared to 800 nm. These results are compatible with our PA spectrum measurements (Fig. 4.2D) and also the thermal heating results where the ratio (700 nm/800 nm) was greater after coagulation. Since the major chromophores at 700 nm and 800 nm are HbO_2, Hb, and MetHb, the change in ratio *k* due to thermal heating most likely came from changes in proportions of hemoglobin components at high temperatures. Ideally, if we can obtain the complete spectrum over a wide range of laser wavelengths during thermal treatments in real-time, any slight changes in tissue composition can be detected due to the unique absorption

and scattering spectrum from each component. However this may require a long acquisition time and, hence, may not facilitate treatment monitoring in a real-time manner. Even without the complete spectrum, we have shown here that two wavelengths are already sufficient to make distinctions between two different tissue statuses. Measurement at a wavelength with stronger water absorption may be used in the future to provide larger contrast showing dehydration as a result of thermal treatment.

4.4.3 Limitations and future study

For simplicity and to demonstrate the proof of concept, in this study, the PA signals from locations close to the tissue surface were investigated. The monitoring technique can be extended to the subsurface volume under one condition. If we rewrite Eq. (4.1) here: $\Delta P(z) = \Gamma \mu_a e^{-z\sqrt{3\mu_a(\mu_a+\mu_s')}} F_0$, the exponential term indicates the decay in laser fluence as light gets absorbed and scattered in the subsurface volume. If the tissue status/properties between the surface and the target sensing/imaging depth *z* remain unchanged over the treatment period, then the exponential term stays constant and the PA signal can be expressed by $\Delta P(z) = \Gamma \mu_a F$, where $F = e^{-z\sqrt{3\mu_a(\mu_a+\mu_s')}} F_0$. The ratio *k* can then be determined similar to Eq. (4.3). However, if the tissue status between the surface and *z* changes (e.g., looking at a depth beneath a HIFU lesion), then the exponential term is no longer constant and the laser fluence at *z* cannot be monitored or normalized. In other words, the dual-wavelength PA technique has the ability to monitor lesion boundaries in the subsurface volume, but not the volume beneath the lesion boundaries.

Water-bath heating was applied in this study to raise temperature and a uniform temperature distribution was generated inside the tissue specimen. For future studies, it is important to investigate the changes in the shape and intensity of PA signal due to a non-uniform temperature distribution generated during HIFU ablation. It is likely that an imaging ultrasound probe is needed otherwise the shape of the PA signal obtained using a single element transducer may change, and data processing methods other than taking the peak-to-peak voltage may be required.

The limited speed of wavelength tuning of the OPO system used in this study does not allow implementation of real-time monitoring of HIFU ablation with the dual-wavelength PA sensing technique. For future exploration, integrating the HIFU system with PA sensing/imaging in real-time is important. We have performed initial tests using two laser systems, each operating at one wavelength. Details are described in Sec. 5.1.

4.5 Conclusions

We demonstrated the feasibility of a dual-wavelength PA sensing technique to detect changes in tissue optical properties due to thermal treatment. Unlike single wavelength PA methods, our technique uses the temperature-independent ratio of the PA signals obtained at two laser wavelengths. Our method can be used to monitor tissue changes during thermal treatment without the need for a calibrated relation of PA signals and temperature in advance. Our results suggest that the technique may have the potential for monitoring thermal treatments such as those based on photothermal, radiofrequency, and HIFU ablations.

4.6 References

1. H. Cui and X. Yang, "Real-time monitoring of high-intensity focused ultrasound ablations with photoacoustic technique: an in vitro study," *Med Phys* 38(10), 5345-5350 (2011)

2. P. V. Chitnis, J. McLaughlan, J. Mamou, T. Murray and R. A. Roy, "A photoacoustic sensor for monitoring in situ temperature during HIFU exposures," *9th Intl Symp Therapeutic Ultrasound* 1215, 267-272 (2010)

3. M. Xu and L. V. Wang, "Photoacoustic imaging in biomedicine," *Rev Sci Instrum* 77(4), (2006)

4. S. Mallidi, G. P. Luke and S. Emelianov, "Photoacoustic imaging in cancer detection, diagnosis, and treatment guidance," *Trends Biotechnol* 29(5), 213-221 (2011)

5. R. O. Esenaliev, A. A. Karabutov and A. A. Oraevsky, "Sensitivity of laser opto-acoustic imaging in detection of small deeply embedded tumors," *IEEE J Sel Top Quant* 5(4), 981-988 (1999)

6. H. F. Zhang, K. Maslov, G. Stoica and L. H. V. Wang, "Functional photoacoustic microscopy for high-resolution and noninvasive in vivo imaging," *Nat Biotechnol* 24(7), 848-851 (2006)

7. K. Maslov, H. F. Zhang, S. Hu and L. V. Wang, "Optical-resolution photoacoustic microscopy for in vivo imaging of single capillaries," *Opt Lett* 33(9), 929-931 (2008)

8. C. Zhang, K. Masiov, S. Hu, R. M. Chen, Q. F. Zhou, K. K. Shung and L. H. V. Wang, "Reflection-mode submicron-resolution in vivo photoacoustic microscopy," *J Biomed Opt* 17(2), 020501 (2012)

9. X. D. Wang, W. W. Roberts, P. L. Carson, D. P. Wood and J. B. Fowlkes, "Photoacoustic tomography: a potential new tool for prostate cancer," *Biomed Opt Express* 1(4), 1117-1126 (2010)

10. H. Cui, J. Staley and X. Yang, "Integration of photoacoustic imaging and high-intensity focused ultrasound," *J Biomed Opt* 15(2), 021312 (2010)

11. A. Prost, A. Funke, M. Tanter, J. F. Aubry and E. Bossy, "Photoacoustic-guided ultrasound therapy with a dual-mode ultrasound array," *J Biomed Opt* 17(6), 061205 (2012)

12. K. V. Larin, I. V. Larina, M. Motamedi and R. O. Esenaliev, "Monitoring of temperature distribution in tissues with optoacoustic technique in real time," *Proc SPIE* 3916, 311-321 (2000)

13. R. O. Esenaliev, A. A. Oraevsky, K. V. Larin, I. V. Larina and M. Motamedi, "Real-time optoacoustic monitoring of temperature in tissues," *Proc SPIE* 3601, 268-275 (1999)

14. I. V. Larina, K. V. Larin and R. O. Esenaliev, "Real-time optoacoustic monitoring of temperature in tissues," *J Phys D Appl Phys* 38(15), 2633-2639 (2005)

15. M. Pramanik and L. V. Wang, "Thermoacoustic and photoacoustic sensing of temperature," *J Biomed Opt* 14(5), 054024 (2009)

16. J. Shah, S. Park, S. Aglyamov, T. Larson, L. Ma, K. Sokolov, K. Johnston, T. Milner and S. Y. Emelianov, "Photoacoustic imaging and temperature measurement for photothermal cancer therapy," *J Biomed Opt* 13(3), 034024 (2008)

17. G. Schule, G. Huttmann, C. Framme, O. Roider and R. Brinkmann, "Noninvasive optoacoustic temperature determination at the fundus of the eye during laser irradiation," *J Biomed Opt* 9(1), 173-179 (2004)

18. S. Kim, Y.-S. Chen, G. P. Luke, M. Mehrmohammadi, J. R. Cook and S. Y. Emelianov, "Ultrasound and photoacoustic image-guided photothermal therapy using silica-coated gold nanorods: in-vivo study," in *2010 IEEE Intl Ultrasonics Symp*, 233-236 (2010)

19. S. M. Nikitin, T. D. Khokhlova and I. M. Pelivanov, "Temperature dependence of the optoacoustic transformation efficiency in ex vivo tissues for application in monitoring thermal therapies," *J Biomed Opt* 17(6), 061214 (2012)

20. T. D. Khokhlova, I. M. Pelivanov, O. A. Sapozhnikov, V. S. Solomatin and A. A. Karabutov, "Opto-acoustic diagnostics of the thermal action of high-intensity focused ultrasound on biological tissues: the possibility of its applications and model experiments," *Quantum Electron* 36(12), 1097-1102 (2006)

21. J. F. Black and J. K. Barton, "Chemical and structural changes in blood undergoing laser photocoagulation," *Photochem Photobiol* 80, 89-97 (2004)

22. P. V. Chitnis, H. P. Brecht, R. Su and A. A. Oraevsky, "Feasibility of optoacoustic visualization of high-intensity focused ultrasound-induced thermal lesions in live tissue," *J Biomed Opt* 15(2), 021313 (2010)

23. A. A. Oraevsky, S. L. Jacques and F. K. Tittel, "Measurement of tissue optical properties by time-resolved detection of laser-induced transient stress," *Appl Opt* 36(1), 402-415 (1997)

24. V. E. Gusev and A. A. Karabutov, *Laser Optoacoustics*, American Institute of Physics, New York (1993)

25. F. A. Duck, *Physical Properties of Tissue*, Academic Press Inc., San Diego, CA (1990)

26. B. Wang and S. Emelianov, "Thermal intravascular photoacoustic imaging," *Biomed Opt Express* 2(11), 3072-3078 (2011)

27. S. M. Nikitin, T. D. Khokhlova and I. M. Pelivanov, "In-vitro study of the temperature dependence of the optoacoustic conversion efficiency in biological tissues," *Quantum Electron* 42(3), 269-276 (2012)

28. R. Sfareni, A. Boffi, V. Quaresima and M. Ferrari, "Near infrared absorption spectra of human deoxy- and oxyhaemoglobin in the temperature range 20-40 degrees C," *Biochem Biophys Acta* 1340(2), 165-169 (1997)

29. J. Laufer, R. Simpson, M. Kohl, M. Essenpreis and M. Cope, "Effect of temperature on the optical properties of ex vivo human dermis and subdermis," *Phys Med Biol* 43(9), 2479-2489 (1998)

30. W. H. Nau, R. J. Roselli and D. F. Milam, "Measurement of thermal effects on the optical properties of prostate tissue at wavelengths of 1,064 and 633 nm," *Lasers Surg Med* 24(1), 38-47 (1999)

31. J. P. Ritz, A. Roggan, C. Isbert, G. Muller, H. J. Buhr and C. T. Germer, "Optical properties of native and coagulated porcine liver tissue between 400 and 2400 nm," *Lasers Surg Med* 29(3), 205-212 (2001)

32. H. Ao, D. Xing, H. Wei, H. Gu, G. Wu and J. Lu, "Thermal coagulation-induced changes of the optical properties of normal and adenomatous human colon tissues in vitro in the spectral range 400-1,100 nm," *Phys Med Biol* 53(8), 2197-2206 (2008)

33. J. W. Pickering, S. Bosman, P. Posthumus, P. Blokland, J. F. Beek and M. J. van Gemert, "Changes in the optical properties (at 632.8 nm) of slowly heated myocardium," *Appl Opt* 32(4), 367-371 (1993)

34. J. W. Pickering, P. Posthumus and M. J. van Gemert, "Continuous measurement of the heat-induced changes in the optical properties (at 1,064 nm) of rat liver," *Lasers Surg Med* 15(2), 200-205 (1994)

35. M. G. Skinner, S. Everts, A. D. Reid, I. A. Vitkin, L. Lilge and M. D. Sherar, "Changes in optical properties of ex vivo rat prostate due to heating," *Phys Med Biol* 45(5), 1375-1386 (2000)

36. T. Vo-Dinh, Ed., *Biomedical photonics handbook*, CRC Press, Bota Raton, FL (2003)

37. L. L. Randeberg, J. H. Bonesronning, M. Dalaker, J. S. Nelson and L. O. Svaasand, "Methemoglobin formation during laser induced photothermolysis of vascular skin lesions," *Lasers Surg Med* 34(5), 414-419 (2004)

38. D. T. Delpy and M. Cope, "Quantification in tissue near-infrared spectroscopy," *Philos Trans R Soc B* 352(1354), 649-659 (1997)

39. S. A. Sapareto and W. C. Dewey, "Thermal dose determination in cancer-therapy," *Int J Radiat Oncol* 10(6), 787-800 (1984)

40. D. Haemmerich, J. G. Webster and D. M. Mahvi, "Thermal dose versus isotherm as lesion boundary estimator for cardiac and hepatic radio-frequency ablation," in *Proc 25th Annual Intl Conf IEEE Engin Med Biol Soc*, 134-137, IEEE (2003)

41. P. S. Yarmolenko, E. J. Moon, C. Landon, A. Manzoor, D. W. Hochman, B. L. Viglianti and M. W. Dewhirst, "Thresholds for thermal damage to normal tissues: An update," *Int J Hyperthermia* 27(4), 320-343 (2011)

42. C. E. Metz, "Basic principles of ROC analysis," *Semin Nucl Med* 8(4), 283-298 (1978)

43. K. V. Larin, I. V. Larina and R. O. Esenaliev, "Monitoring of tissue coagulation during thermotherapy using optoacoustic technique," *J Phys D Appl Phys* 38(15), 2645-2653 (2005)

44. E. Salomatina and A. N. Yaroslavsky, "Evaluation of the in vivo and ex vivo optical properties in a mouse ear model," *Phys Med Biol* 53(11), 2797-2807 (2008)

45. G. M. Palmer, C. L. Marshek, K. M. Vrotsos and N. Ramanujam, "Optimal methods for fluorescence and diffuse reflectance measurements of tissue biopsy samples," *Lasers Surg Med* 30(3), 191-200 (2002)

46. A. M. K. Nilsson, C. Sturesson, D. L. Liu and S. Andersson-Engels, "Changes in spectral shape of tissue optical properties in conjunction with laser-induced thermotherapy," *Appl Optics* 37(7), 1256-1267 (1998)

47. J. P. Ritz, A. Roggan, C. Isbert, G. Muller, H. J. Buhr and C. T. Germer, "Optical properties of native and coagulated porcine liver tissue between 400 and 2400 nm," *Lasers Surg Med* 29(3), 205-212 (2001)

CHAPTER 5

Conclusions and future work

Focused ultrasound (FUS) is a promising modality for non-invasive, targeted hyperthermia and HIFU ablation.[1-3] However, FUS-compatible guiding and monitoring systems to provide real-time measurement on temperature and tissue status are limited to ultrasound and magnetic resonance imaging (MRI). The work described in this dissertation represents efforts to develop new tools to boost the current research on ultrasound thermometry and to investigate new imaging modalities to improve controlled HIFU ablation based on infrared (IR) thermography and photoacoustic (PA) imaging.

This dissertation research contributed to the field of ultrasound thermometry by introducing IR thermography as a new independent temperature measurement tool to calibrate tissue-specific properties and to validate temperature estimation in a fast manner with high spatial information unavailable in previous studies (Chapter 2). In Chapter 3 we further utilized IR thermography to monitor lesion formation and bubble activities that occurred close to the tissue surface. The spatiotemporal temperature characteristics determined in correspondence to HIFU events are applicable to HIFU monitoring using alternative temperature measuring techniques. The presented experimental design using simultaneous bright-field imaging and IR imaging is advantageous for determining tissue-specific thermal damage threshold, which is a critical indicator of successful treatment outcome for various types of thermal therapy. Finally, an innovative PA imaging technique

to monitor tissue status independent of temperature by utilizing laser illuminations at two wavelengths was proposed (Chapter 4). The method can be extended to multiple wavelengths, with the choice of wavelengths dependent on the absorption spectrum of the target object. The temperature-independent parameter can be applied in monitoring thermal therapy including but not limited to HIFU ablation, photothermal treatment, and radiofrequency ablation. When the technique is further utilized for tissue characterization in diagnostic settings, by eliminating factors due to variations in patient body temperature and environment temperature, it may improve diagnosis accuracy compared to single wavelength PA imaging techniques.

For the techniques presented in this dissertation to become more clinical relevant, they have to be further demonstrated *in-vivo* where effects such as blood perfusion during FUS heating need to be considered. Laparoscopic IR probes[4] can be used for the second study, and PA endoscopes with integrated optical fibers for light delivery[5] can be used for the third study.

Other future studies which we would like to investigate include 1) real-time HIFU ablation monitoring using dual-wavelength PA imaging, 2) tissue characterization using non-ablative FUS-modulated active dynamic IR thermography, and 3) tissue characterization using non-ablative FUS-modulated PA imaging. The rationale and preliminary results are described in more details in the following sections.

5.1 Real-time HIFU ablation monitoring using dual-wavelength PA imaging

As mentioned in Sec. 4.4.3, for real-time HIFU monitoring, we have integrated two laser systems by adding another Nd:YAG laser system (Powerlite DLS 8010, Continuum, Santa Clara, CA) operating at 1064 nm to the original set-up (Fig. 5.1). The choice of 1064 nm is because of water being more absorptive of light at this wavelength[6] and the resulting ratio *k* may provide a better contrast when tissue coagulates, which is generally accompanied by dehydration. The OPO laser operates at a wavelength tunable from 680 to 950 nm, and a dichroic mirror (50% transmittance/reflectance at 900 nm) is used to allow the light beam to propagate into the same direction into the tissue specimen. Synchronization between the two laser systems and HIFU system is achieved using the delay/pulser, with pulse sequences shown in Fig. 5.2.

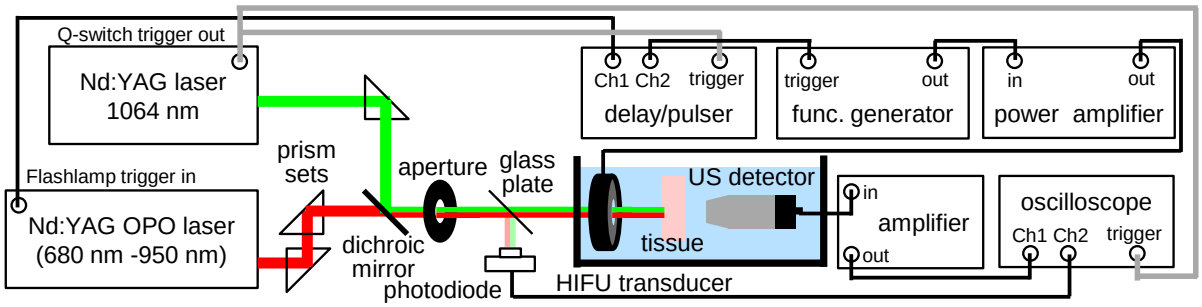

Figure 5.1 Schematic of the real-time dual-wavelength PA sensing during HIFU application using two laser sources.

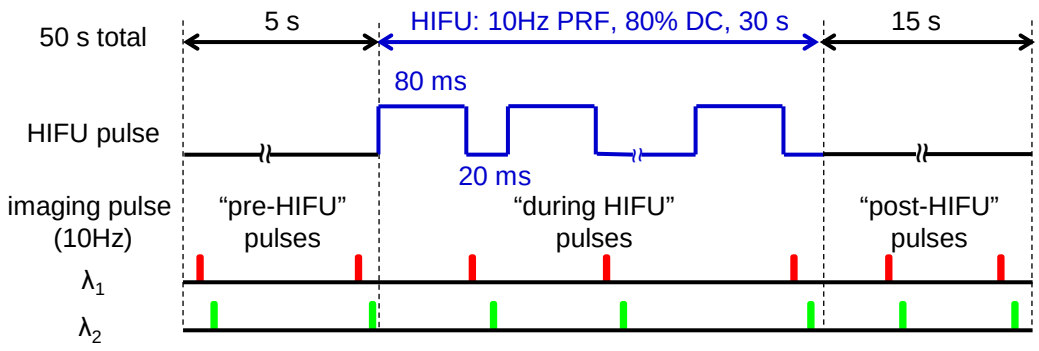

Figure 5.2 Time sequence interleaving HIFU exposures and PA imaging pulses with laser wavelength λ_1 = 1064 nm and λ_2 = tunable 680 – 950 nm.

5.1.1 Preliminary results

Fig. 5.3A shows an example of the normalized PA amplitude *P* (calculated by dividing the peak-to-peak PA signal amplitude by the peak amplitude of the photodiode signal) at 700 nm and 1064 nm before, during, and after a 30 sec HIFU exposure (2 MHz center frequency, 1500 W/cm^2 focal intensity, 80% DC, 10 Hz PRF). No observable lesion was formed on the tissue surface. Although the ratio between the normalized PA amplitude obtained at the two wavelengths (1064 nm/700 nm, Fig. 5.3B) stayed almost constant over time, it exhibited undesired large standard deviation (S.D.) which defeats its purpose for accurate monitoring of changes in tissue status. Moreover, in cases where HIFU lesions were generated, the acoustic transparent wrap used for preventing changes in hydration and concentration of chromophores in the tissue specimen was also heated and damaged, making the source of signal change not coming from the tissue alone.

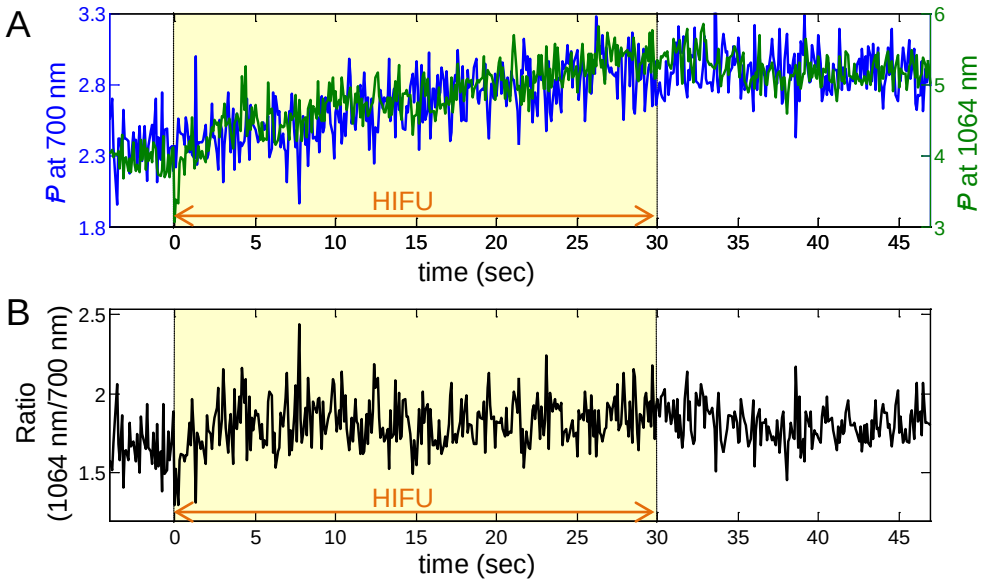

Figure 5.3 (A) Normalized PA amplitude $\bar{P}$ with laser illuminations at 700 nm and 1064 nm before, during, and after a 30 sec HIFU exposure. (B) Corresponding ratio (1064 nm/700 nm).

For further studies of real-time HIFU monitoring using the dual-wavelength PA technique, it is important to have alternative set-up designs and/or more advanced signal processing methods to achieve higher signal-to-noise ratio (SNR) and a smaller signal S.D. Short time averaging or filtering may be used without slowing the ablation process. The overheating of the wrap also needs to be avoided. Moreover, since light beam is scattered and absorbed as it penetrates into the tissue, the feasibility of applying the same technique for monitoring HIFU ablation aimed at the tissue subsurface volume needs to be further investigated. Composite parameters combining temperature and tissue status will be investigated to further improve sensitivity and specificity. For the technique to become more widely adopted in the long term, advancement in new laser systems capable of fast wavelength tuning at lower cost is critical.

5.2 Tissue characterization using non-ablative FUS-modulated active dynamic IR thermography

Most clinical applications of IR thermography use only passive temperature measurements. However the use of an external heat source to induce thermal response inside tissue has received more attention over the past few years.[7] These kinds of "active dynamic IR imaging" are less sensitive to external conditions such as ambient temperature and provide visualization on subsurface abnormalities. When subjected to the same heat source, different tissue types may exhibit different transient temperature responses, which can be utilized for tissue characterization. Microwave radiation and halogen lamp are commonly used heat sources for active dynamic IR imaging. For example, IR temperature measurements with the use of halogen lamp to heat up skin have been investigated for differentiating burn wounds with varying burn depths.[8] However, to better visualize subsurface abnormalities, our hypothesis is to instead use FUS to noninvasively generate a heat source in the subsurface volume. Since FUS is only applied to induce transient temperature changes and not cause tissue damage, acoustic intensity needs to be in the non-ablative range.

Although for different tissue compositions or tissue types, the IR measured surface temperature evolution may already be different (as demonstrated in Sec. 3.3.4 for HIFU lesions and normal tissue), it is more valuable if the 3D spatiotemporal temperature information in the subsurface volume can be further reconstructed. In our collaboration work,[9] the 3D acoustic and thermal properties as well as temperature evolution within a subsurface tissue volume was reconstructed based on the spatiotemporal IR temperature measurements. However the algorithm used was computationally intensive. Therefore, we

propose to use another inverse bio-heat transfer method to reconstruct the tomographic temperature distribution without first reconstructing the acoustic and thermal properties. The method will use multiple control points to compute the 3D heat source generated by FUS exposures with the assumption of axial symmetry along the FUS propagation path. These control points distribute over various depths and distances from the FUS focus. The 3D heat source is optimized by minimizing an objective function $f(T_{IR}-T_C)$, where T_{IR} is the IR-measured temperature and T_C is the corresponding set of calculated temperature. The 3D temperature distribution is then calculated based on the 3D heat source and will be verified with temperature measured by thermocouples inserted in the subsurface.

A Potential model for FUS-modulated active dynamic IR imaging is breast cancer. The differences in ultrasound absorption and thermal conduction between breast tumor and normal breast tissue can result in a different temperature transient under the same FUS exposure. However, for 3D inverse reconstruction of temperature, the inhomogeneity in breast tissue may introduce reconstruction errors and needs to be carefully examined.

5.3 Tissue characterization using non-ablative FUS-modulated PA imaging

Based on the results from this dissertation and using a similar concept as in Sec. 5.2, we discover a potential imaging modality with a newly defined tissue contrast, which combines the optical, acoustic, and thermal properties of tissue. It was shown in Chapter 4 that below tissue coagulation threshold, the relative percentage change in PA signal intensity under a certain temperature change depends on the tissue type. The reason behind such phenomenon is because the thermal expansion coefficient and speed of sound of tissue depend on its composition and are often temperature dependent. For example, HIFU lesions

had a smaller averaged relative percentage change compared to that of native tissue under the same temperature increment (Section 4.3.2 and Fig. 4.3) likely due to their having a lesser water content. The phenomenon was also observed in Chapter 2 where water-based and oil-based phantoms exhibited different echo time shifts under the same temperature rise. The concept can therefore be brought into tissue characterization using PA imaging with temperature elevation provided from an external heat source. The changes in PA signal due to temperature changes can be different in different tissue types, providing contrasts unavailable at a fixed temperature. A similar concept was proposed by Wang and Emelianov[10] to distinguish periadventitial fat and lipid-rich atherosclerotic plaques, which were undistinguishable using spectroscopic PA methods. However their experiment was performed in water bath and warm saline and cold ice were used to adjust the temperature, which are not practical and feasible in clinical use. To generate temperature transient non-invasively, FUS again is the ideal candidate.

The potential of lower intensity, non-ablative FUS heating to generate temperature transient as a diagnostic or post-treatment assessment tool was also studied in Section 3.3.4 using IR thermography. Under the same FUS transducer settings, the higher acoustic absorption in HIFU lesions led to the higher temperature rise compared to that of native tissue (Fig. 3.13 and Fig. 3.14). Therefore by combing non-ablative FUS exposures with PA imaging, a new tissue contrast is developed based on the combined differences in the optical, acoustical, and thermal properties in different tissue types.

5.3.1 Theory: FUS-modulated PA tissue contrast

Assume PA signals are collected for two tissue types/statuses s_1 and s_2 at their baseline temperature T_0 and their individual FUS-elevated temperature of T_1 and T_2, where T_1

and T_2 depend on their acoustical and thermal properties. Using Eq. (4.2) at one single laser wavelength: $\Delta P_{s,T} = \Gamma_{s,T}\alpha_s F_0$, we have the pressure rises summarized in Table 5.1. The tissue contrast, defined as the ratio between the PA signal intensity after FUS heating and before FUS heating, now only depends on the Grüneisen parameter Γ, and not the optical properties.

Table 5.1 Tissue contrast from PA imaging with FUS-induced temperature modulation.

	Tissue s_1	Tissue s_2
Before FUS exposure (Baseline Temp. T_0)	$\Delta P_{s_1,T_0} = \Gamma_{s_1,T_0}\alpha_{s_1}F_0$	$\Delta P_{s_2,T_0} = \Gamma_{s_2,T_0}\alpha_{s_2}F_0$
After FUS exposure	(Temp. T_1) $\Delta P_{s_1,T_1} = \Gamma_{s_1,T_1}\alpha_{s_1}F_0$	(Temp. T_2) $\Delta P_{s_2,T_2} = \Gamma_{s_2,T_2}\alpha_{s_2}F_0$
Tissue contrast (after FUS/before FUS)	$\frac{\Gamma_{s_1,T_1}}{\Gamma_{s_1,T_0}}$	$\frac{\Gamma_{s_2,T_2}}{\Gamma_{s_2,T_0}}$

5.3.2 Potential models

Considering the technique does not detect one particular tissue property, but rather the combined effect from the acoustical (FUS heating), optical (PA imaging), and thermal (FUS heating) properties, we propose the following prominent models for future exploration: fatty liver, tumor, osteoporosis etc. The method should be most promising in distinguishing fat-based and water-based tissues due to the Γ of fat is inversely proportional to temperature whereas Γ of water is proportional to temperature. The resulting tissue contrasts will therefore be negative in fat and positive in water in the extreme.

5.5 References

1. J. E. Kennedy, "High-intensity focused ultrasound in the treatment of solid tumours," *Nat Rev Cancer* 5(4), 321-327 (2005)

2. G. ter Haar, "Harnessing the interaction of ultrasound with tissue for therapeutic benefit: High-intensity focused ultrasound," *Ultrasound Obst Gyn* 32(5), 601-604 (2008)

3. S. Crouzet, F. J. Murat, G. Pasticier, P. Cassier, J. Y. Chapelon and A. Gelet, "High intensity focused ultrasound (HIFU) for prostate cancer: Current clinical status, outcomes and future perspectives," *Int J Hyperthermia* 26(8), 796-803 (2010)

4. K. Ogan, W. W. Roberts, D. M. Wilhelm, L. Bonnell, D. Leiner, G. Lindberg, L. R. Kavoussi and J. A. Cadeddu, "Infrared thermography and thermocouple mapping of radiofrequency renal ablation to assess treatment adequacy and ablation margins," *Urology* 62(1), 146-151 (2003)

5. J. M. Yang, K. Maslov, H. C. Yang, Q. F. Zhou, K. K. Shung and L. V. Wang, "Photoacoustic endoscopy," *Opt Lett* 34(10), 1591-1593 (2009)

6. T. Vo-Dinh, Ed., *Biomedical photonics handbook*, CRC Press, Bota Raton, FL (2003)

7. A. Nowakowski, "Quantitative active dynamic thermal IR-imaging and thermal tomography in medical diagnostics," in *Medical infrared imaging*, N. A. Diakides and J. D. Bronzino, Eds., 7-1-7-29, CRC Press, New York, NY (2008)

8. A. Renkielska, A. Nowakowski, M. Kaczmarek and J. Ruminski, "Burn depths evaluation based on active dynamic IR thermal imaging - A preliminary study," *Burns* 32(7), 867-875 (2006)

9. L. Yin, M. S. R. Gudur, Y.-S. Hsiao, R. E. Kumon, C. X. Deng and H. Jiang, "Tomographic reconstruction of tissue properties and temperature increase for high-intensity focused ultrasound applications," *Ultrasound Med Biol* (2013)

10. B. Wang and S. Emelianov, "Thermal intravascular photoacoustic imaging," *Biomed Opt Express* 2(11), 3072-3078 (2011)

Appendix

Theory of infrared radiation

All objects with a temperature > 0 K radiate energy. The relation between total radiation power W (watt) and temperature T (K) of a blackbody can be expressed by the Stefan-Boltzmann law[1]

$$W = A \cdot \sigma \cdot T^4 , \tag{6.1}$$

where the radiated power is from a body of area A (m^2) and σ is the Stefan-Boltzmann constant = 5.67×10^{-8} ($W\cdot m^{-2}\cdot T^{-4}$). Unlike Stefan-Boltzmann law which integrates the radiation over the entire spectrum, infrared (IR) cameras operate in a specific range of wavelengths and use a different relation between received radiation power and temperature. Conversion from IR radiance to temperature is usually performed using the manufacturer's calibration and non-uniformity corrections. For derivation purposes, we denote W simply as a function of T: $W(T)$. The temperature of the object of interest T_{obj} measured using IR thermography can therefore be calculated from W_{obj}, the radiation power from the object if it were a black body. The total received radiation power W_{tot} from the IR camera is expressed as[2]

$$W_{tot} = \varepsilon \cdot \tau \cdot W_{obj} + (1-\varepsilon) \cdot \tau \cdot W_{amb} + (1-\tau) \cdot W_{atm} , \tag{6.2}$$

where ε is the emissivity of the object, τ is the transmittance of the atmosphere, and W_{amb} and W_{atm} are the radiation power from ambient sources and the atmosphere. With air atmosphere, τ can be assumed to be 1 (100% trasmittance) and Eq. (6.2) can be simplified to

$$W_{tot} = \varepsilon \cdot W_{obj} + (1-\varepsilon) \cdot W_{amb} . \quad (6.3)$$

For precise temperature conversion from W_{obj}, ε and W_{amb} have to be accurately provided.

A.1 Ambient temperature

W_{amb} can be determined if the ambient temperature is given. When the object is at room temperature $T_{obj} = T_{amb}$, we can assume $W_{obj} = W_{amb} = W$. Substituting Eq. (6.3) gives us

$$W_{tot} = \varepsilon \cdot W + (1-\varepsilon) \cdot W = W , \quad (6.4)$$

where ε does not affect the total radiance and W_{amb} simply equals W_{tot}. This simple method should be used immediately before each experiment with the target object left at room temperature for sufficient long period of time to ensure temperature equilibrium.

A.2 Emissivity

As seen in Eq. (6.3), accurate input of ε is also important for temperature conversion, particularly for objects with low ε. To measure emissivity,

$$\varepsilon = \frac{W_{tot} - W_{amb}}{W_{obj} - W_{amb}} . \quad (6.5)$$

Note that emissivity measurement cannot be performed with the object at ambient temperature ($W_{obj} = W_{amb}$). To estimate the temperature measurement error due to inaccurate input emissivity ε_{input}, let $\varepsilon_{input} = \varepsilon_{true} + d\varepsilon$, where ε_{true} is the true emissivity and $d\varepsilon$ is the error, and object radiation power $W_{obj} = W_{amb} + dW$, where dW is the radiation power difference between the object and the ambient temperature. The error of between calculated object radiation power W_{cal} and true radiation power W_{true} can then be derived from Eq. (6.3):

$$W_{tot} = \varepsilon_{input} \cdot (W_{amb} + dW) + (1-\varepsilon_{input}) \cdot W_{amb} = \varepsilon_{input} \cdot dW + W_{amb} \quad (6.6)$$

$$dW = \frac{W_{tot} - W_{amb}}{\varepsilon_{input}} = \frac{W_{tot} - W_{amb}}{\varepsilon_{true} + d\varepsilon} \tag{6.7}$$

$$W_{error} = W_{cal} - W_{true} = \frac{W_{tot} - W_{amb}}{\varepsilon_{true} + d\varepsilon} - \frac{W_{tot} - W_{amb}}{\varepsilon_{true}} = \frac{-d\varepsilon \cdot \left(W_{tot} - W_{amb}\right)}{\varepsilon_{true} \cdot \left(\varepsilon_{true} + d\varepsilon\right)} \tag{6.8}$$

Note that when $\varepsilon_{\text{true}}$ is smaller, W_{error} is larger. Therefore care must be taken especially when imaging objects with small ε value.

A.3 References

1. T. L. Bergman, A. S. Lavine, D. P. Dewitt, and F. P. Incropera, "Radiation: processes and properties," in *Introduction to heat transfer*, 733-826, John Wiley & Sons, Inc., Hoboken, NJ (2011)

2. C. Öhman, "Measurement in thermography," FLIR Systems AB (2001)